

DEVELOPMENT OF A GAS MICROVALVE BASED ON FINE AND MICROMACHINING

IMRAN FAZAL

Graduation committee

Chairman

Prof. dr. ir. A. J. Mouthaan

University of Twente

Promotor

Prof. dr. M. C. Elwenspoek

University of Twente

Assistant promotor

Dr. ir. H. V. Jansen

University of Twente

Members

Prof. dr. ir. Albert van den Berg

University of Twente

Prof. dr. Han Gardeniers

University of Twente

Prof. dr. Engg. Peter Enoksson

Chalmers University

Prof. dr.-Ing. habil. Jörg Müller

Technical University Hamburg Harburg

Prof. dr. Roland Zengerle

University of Freiburg

Dr. ir. Joost Lötters

Bronkhorst High Tech B. V.

This work presented in the dissertation was carried out at the Transducers Science & Technology Group of University of Twente, with the financial support of the Dutch Technology Foundation (STW) under the project no. TPC. 5610 “Micro and Miniaturized Flow Controller for Gas Chromatography”.

Development of gas microvalve based on fine- and micromachining

Imran Fazal

PhD. Thesis, University of Twente, Enschede, The Netherlands

ISBN: 978-90-365-2571-8

Copyright © Imran Fazal, Enschede 2007

Printed by Wöhrmann Printservice, Zutphen, The Netherlands

DEVELOPMENT OF A GAS MICROVALVE BASED ON FINE- AND MICROMACHINING

DISSERTATION

to obtain
the doctor's degree at the University of Twente,
on the authority of the rector magnificus,
prof. dr. W. H. M. Zijm,
On account of the decision of the graduation committee,
To be publicly defended

on Friday 19th October 2007 at 15:00

by
Imran Fazal
born on 12th November 1975
in Lahore, Pakistan

This doctoral dissertation is approved by:

Promotor: Prof. dr. M. C. Elwenspoek

Assistant promotor Dr. ir. H. V. Jansen

To my parents, my wife and my Son

Table of Contents

1	Introduction	1
1.1	Motivation of the work	2
1.2	General introduction	2
1.3	Literature study	2
1.4	Conclusions.....	14
1.5	Outline of thesis	14
2	Design and Modeling	17
2.1	Introduction.....	18
	2.1.1 Operational Modes.....	20
	2.1.2 Gas Flow Model.....	20
	2.1.3 Additional resistance.....	24
2.2	Validity of the design model.....	27
	2.2.1 Mach number	27
	2.2.2 Reynolds number	29
	2.2.3 Entrance length	31
2.3	Design parameter selection.....	31
2.4	Fine machined part: Stepper motor and screw mechanism for mechanical transmission	34
2.5	Simulation.....	39
	2.5.1 Pressure	42
	2.5.2 Mach number	43
	2.5.3 Velocity profile	44
	2.5.4 Density	45
	2.5.5 Volume flow	48
2.6	Conclusions.....	49
3	Stepper Motor Actuated Microvalve	51
3.1	Introduction.....	52
3.2	Fabrication	54
3.3	Characterization	58
	3.3.1 Experimental setup.....	58
	3.3.2 Volume flow rate measurements	59
	3.3.3 Stepper motor performance.....	63
3.4	Modifications	65
	3.4.1 Fabrication	66
	3.4.2 Characterization	67
3.5	Conclusions.....	71

Table of Contents

4	Piezoelectric Actuated Microvalve	73
4.1	Introduction.....	74
4.2	Design description	74
4.3	Characterization of piezoelectric actuated microvalve.....	76
4.3.1	Experimental setup.....	76
4.3.2	Volume flow rate measurements	76
4.3.3	Controllability	77
4.3.4	Backlash behavior.....	78
4.3.5	Hysteresis.....	78
4.4	Conclusions.....	80
5	Pressure regulator microvalve	81
5.1	Introduction.....	82
5.2	Valve design and modeling.....	82
5.3	Fabrication	84
5.4	Characterization	87
5.4.1	Chamber pressure measurements.....	87
5.5	Conclusions.....	90
6	Fusion Bonded Fluidic Interconnects	91
6.1	Introduction.....	92
6.2	Fabrication	92
6.3	Characterization	95
6.3.1	Experimental setup.....	95
6.3.2	Bond strength analysis	95
6.4	Conclusions.....	100
7	Conclusions and Future Aspects	101
	Bibliography	105
	List of Publications	119
	Acknowledgements	121
	Biography	123
	Appendix	125
A	125
B	127
C	153
D	155
E	157

Chapter 1

1 Introduction

Abstract

The first chapter gives an impression of the fascinating world of microvalve and the significance of the achievements of microsystems research for present and future. This chapter presents the motivation and the project goals of the work presented in this thesis. Finally the structure of the thesis is presented.

1.1 Motivation of the work

The work presented in this thesis is generated in the frame of the project “Micro and Miniaturized Flow Controller for Gas Chromatography” financially supported by the Dutch Technology Foundation (STW). The aim of the project is to develop a miniature instrument for the control of gas flow known as flow controller. An important application of the flow controller is gas chromatography. Gas chromatography is a method for separating substances in a mixture and measuring the relative quantities of substances. It is a useful technique for substances that do not decompose at high temperatures and when a very small quantity of sample (micrograms) is available. Since there is a strong trend to miniaturize these systems as small systems use small amounts of materials and smaller samples for analysis, small flow controllers are demanded. Flow controllers are comprised of controllable valves, flow sensors and control electronics. The research subject in this project is directed mainly to miniature valve, which currently forms the bottleneck in the development of the miniature flow controller. In this thesis a new design of a valve is proposed, which has the attractive feature that no power is required to keep the valve at a freely chosen position. To achieve the aforesaid objective to realize a controllable valve with no power consumption to keep the valve at a freely chosen position, a combination of micromachining and conventional fine machining is explored.

1.2 General introduction

One of the key building blocks for successful miniaturization and commercialization of microfluidic systems is the development of reliable microvalves. In recent years a great deal of research has been conducted to design and develop microvalves for different fluidic systems. These systems involve the integration of many individual steps performed in chemical analysis. This requires the ability to control flow and transport of reagents and samples throughout different parts of the system with lowest amount of fluid leakage. Microvalves have been developed in the form of active or passive microvalves employing mechanical, non mechanical and external systems. Despite the fact that great progress has been made during the last two decades, there is plenty of room for further improving the performance of the existing microvalves.

1.3 Literature study

The present microvalves can be broadly categorized as shown in Table 1-1. Generally they fall into two categories: passive and active microvalves. Passive micro-valves are simply check valves. These microvalve systems are mostly silicon based but some non-silicon based passive microvalves have also been produced. They are mainly used to restrict the flow in one direction. Passive microvalves are most commonly used in micro-pump applications. Very small leakage is required for passive microvalves. The response time, time that is the transition time during the open-to-close or close-to-open, is another important parameter for the passive microvalve applications.

Active micro valve systems use actuators to regulate the flow and obtain the desired flow rate. Active microvalves are complicated systems compared to passive ones. There are multiple different actuation methods used in active microvalves.

Active microvalves; using mechanical and non mechanical moving parts as well as external systems, and passive microvalves; use mechanical and non-mechanical moving parts [1]. Active valves are further categorized into three groups according to their actuation principles. In the first category, the mechanical active microvalves are realized using the MEMS based bulk or surface micromachining technologies, where mechanically movable membranes are attached to magnetic, electric, piezoelectric or thermal actuation methods. In the second category, the unconventional non-mechanical active microvalves can be actuated by the use of smart or intelligent materials. These microvalves may hold moveable membranes which are actuated due to their functionalized smart materials such as phase change or rheological materials. The third is the external active microvalves actuated by the aid of external systems such as built-in modular or pneumatic means. A modular valve structure comprising a fluid structure valve part, a drive part and a plurality of different valve components. Additionally, the microvalves based on their initial modes, can be divided into normally open, normally closed and bistable microvalves [1].

A variety of actuation principles are used to actuate the mechanical moving parts in the active microvalves. Figure 1-1 shows the actuation principles widely in use in the microvalve structures. Though, the configurations of these valves could be different (open or closed valve) but the structures are very similar. Generally they have a deflectable membrane and a valve seat with inlet and outlet or a deflectable membrane with groove or channel. When the membrane is deflected, it seals the inlet on the valve seat or closes the valve or it changes the channel geometry to control the flow. This deflected membrane is coupled to magnetic [2-13], electric [16-27], piezoelectric [29-38], thermal [39-57] or other actuation methods [58-66]. These active microvalves are realized using MEMS based bulk or surface micromachining technologies. Table 1-2 gives an overview of the performance of the demonstrated active microvalves.

Table 1-1: Classification of microvalves [1].

Categories				
Active	Mechanical	Magnetic	External magnetic fields Integrated magnetic inductors	
		Electric	Electrostatic Electrokinetic	
		Piezoelectric		
		Thermal	Bimetallic Thermopneumatic Shape memory alloy	
		Bistable		
	Non-mechanical	Electrochemical		
		Phase change	Hydrogel Solo-gel Paraffin	
		Rheological	Electro-rheological Ferrofluids	
		External	Modular	Built-in Rotary
			Pneumatic	Membrane In-line
Passive	Mechanical	Check valve	Flap Membrane Ball In-line mobile structure	
		Non-mechanical	Diffuser	
	Capillary	Abrupt Liquid triggered Burst Hydrophobic valve		

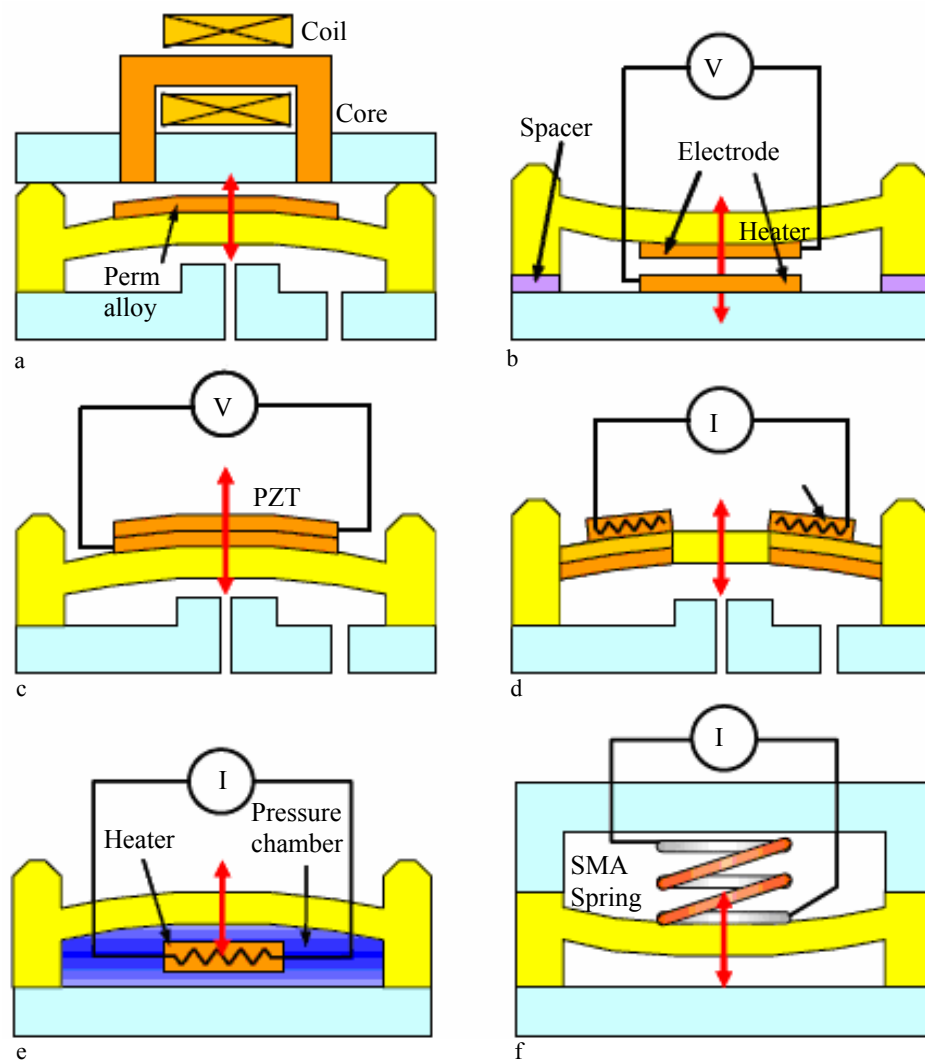


Figure 1-1: Actuation principles of active microvalves with mechanical moving parts: a) electromagnetic b) electrostatic c) piezoelectric d) bimetallic e) thermopneumatic and f) shape memory alloy [1].

Table 1-2: Mechanical active microvalves [1].

Reference	Type	Mechanical part	Mode	Fluid	Valving time (ms)	On/off switching		Flow regulation			Leakage		
						Max. pressure (kPa)	On/off Power	Generated force/pressure/deflection	Measured flow (μlmin^{-1})	Applied Power	Applied pressure (kPa)	Measured leakage (μlmin^{-1})	Applied pressure (kPa)
Terry et al [2]	EM	M	NC	G									
Yanagisawa et al [3]	EM	M	NO	V							7.5 E-13		
Meckes et al [4]	EM	M	NO	G				0.8 mN		0.025 A			
Bae et al [5, 6]	EM	M	NO	L				2.3 kPa		0.06 A			
Krusemark et al [7]	EM	Ball	NC	G									
Oh et al [8]	EM	Ball	NC	L					1300 000	1.0 A		1	21
Fu et al [9]	EM	Ball	NO	G	10				500 000	0.2 A	50		
Oh et al [10, 11]	EM	Pinch	NC	L		207	0.12 A		836 000	0.16 A	8.2	0	207
Ahn's group [12]	EM	Integrated	NC	G			0.25 A					5.6	4.8
Ahn's group [13]	EM	Integrated	NC	DI			0.25 A					3.9	4.1
Shikida et al [16, 17]	ES	M	NO	G			200 V		1 000		0.1		
Goll et al [18]	ES	M	NO	N2			60 V	25 μm	12 000		110		
Robertson and Wise [19]	ES	M	NO	G	0.1		80 V		0.87		0.75		
Schailble [20]	ES	M	NC		1								
Wijngaart et al [21]	ES	M	NC	Air				15 μm		366 V	500		
Wijngaart et al [21]	ES	M	B	Air				5 μm		24 V	100		
Yobas et al [22, 23]	ES	M	NO	Air		82.7							
Yang et al [27]	ES	M	NC	N2					45 000	136 V	900		
Yang et al [27]	ES	M	NC	He								6	170
Roberts et al [29, 30]	PE	M	NC	G				17 μm	12 600	500 V	260		
Rogge et al [31]	PE	M	NC	N2	2	193	245 V	50 μm				30	200
Rogge et al [31]	PE	M	NC	DI								0.013 3	100

Continued part of Table 1-2

Reference	Type	Mechanical part	Mode	Fluid	Valving time (ms)	On/off switching		Flow regulation			Leakage		
						Max. pressure (kPa)	On/off Power	Generated force/pressure/deflection	Measured flow (μlmin^{-1})	Applied Power	Applied pressure (kPa)	Measured leakage (μlmin^{-1})	Applied pressure (kPa)
Shao et al [32]	PE	M	NC	N2	0.7				70 000		50		
Peirs et al [33]	PE	Ball	NO	DI				140 N		100 V		420	600
								6 μm					
Chakraborty et al [34]	PE	M	NC	Air				10 μm					
Yang et al [35]	PE	M	NC	He					52 000	10 V	2070	5	550
Waibel et al [36–38]	PE	Lip	NC	Ink				80 μm	190	140 V		0.002	1
Jerman [39]	BM	M	NC	N2					150 000		350	30	34.5
Barth [40]	BM	M	NC	Air	200	1035			1000 000	1.03 W			
Rich and Wise [41]	TP	M	NO	G	1 s	7.4 Pa	0.34 W	0.016 kPa		0.5 W			
Rich and Wise [41]	TP	M	NO	G					400 000		0.011 3	1	
Ruzzu et al [42]	TP	M	NO	G			0.04 W				20	9600	20
Takao et al [43]	TP	M	NO	DI	5 s (O) 8 s (C)		0.2 W				20	1	30
Yang et al [44, 45]	TP	M	NO	DI				134 μm			28.3		
Yang et al [44, 45]	TP	M	NO	N2					1000 000	0.04 W	228		
Bacchi et al [46, 47]	TP	M	NO	L	150 (C)			3.5 μm		0.24 W			
Kim et al [48]	TP	M	NO	DI	25 s (O) 20 s (C)		0.2 W	40 μm		0.025 W			
Kohl et al [53]	SMA	M	NO	G	22			20 μm	360 000	0.22 W	250		
Reynaerts et al [55]	SMA	Pinch	NC	L	660 (O)		0.12						
Pemble and Towle [56]	SMA	Pinch	NC	L	1 s (O) 2.5 s (C)	207			16 800	0.398 W	20.7		

Continued part of Table 1-2

Reference	Type	Mechanical part	Mode	Fluid	On/off switching			Flow regulation			Leakage		
					Valving time (ms)	Max. pressure (kPa)	On/off Power	Generated force/pressure/deflection	Measured flow (μLmin^{-1})	Applied Power	Applied pressure (kPa)	Measured leakage (μLmin^{-1})	Applied pressure (kPa)
Tamanaha et al [57]	SMA	Pinch	NC	A				2.35 N					
								406 μm					
Goll et al [61]	Thermal	M	B	G		47							
Ren and Gerhard [62]	EM	Cantilever	B	A	0.3 (C)		1.25 A	5 mN					
								100 μm					
Bohm et al [63]	EM	M	B	DI				200 μm					
Bosh et al [66]	EM+ES	M	B	G	0.4		0.2 A (O) 30 V (C)		3 000		16		

EM: Electromagnetic, ES: Electrostatic, PE: Piezoelectric, TP: Thermo-pneumatic, SMA: Shape memory alloy, M: Membrane, B: Bistable, NO: Normally open, NC: Normally closed, I: Inlet, OL: outlet, G: gas, DI: deionized water, V: Vacuum

The active microvalves with non-mechanical moving parts include the actuation principles based on electrochemical [67-71], phase change [72-95], and rheological materials [96-101]. Phase change actuation includes different actuation mechanism such as the hydrogel [72-84], solo gel [85, 86] and paraffin [87-95]. Additionally, electro-rheological materials [96] or ferrofluids [99-101] can be used for the non mechanical active microvalves. These microvalves are relatively new and cheap compared to the traditional mechanical active microvalves. These non mechanical active microvalves are of particular interest in terms of their simple device structure and disposability, making them well suited for life sciences applications (see Table 1-3).

The active microvalves using external systems include modular built in valves [102-105], rotational [106-108], thin membrane [109-124] or in line [125-131] microvalves actuated by the external pneumatic air pressure or vacuum. This is one of the best approaches in designing the microvalves. It can produce high force and deflection. In certain cases process gas can be isolated from the actuation. Additionally actuation in this case is advantageous with no leakage at high inlet pressures. The miniaturization is difficult due to the requirement of additional external system (see Table 1-4).

The passive microvalves with mechanical moving parts or check valves are integrated in inlets and outlets of reciprocal displacements micropumps as mechanical moving parts, such as flaps [140-152], membranes [153-164], spherical balls [166-169] or mobile structures [170-172]. Passive valves are operational only to forward pressure. This characteristic of the check valves significantly affects the pumping performance of a reciprocal displacement micropump. Leakage in the check valves reduces back pressure and pumping rate in the micropump (see Table 1-5).

The passive microvalves without mechanical moving parts, also known as valveless micropumps, using some sort of nozzle [174-179], diffuser [180-184], or Tesla elements [185,186] have been extensively used in inlets and outlets of reciprocal displacement micropumps. Another approach to control the flow, where advantage of the large surface to volume ratio in microfluidic systems is taken, is the passive capillary microvalves utilizing the geometries or the surface properties in the microchannels [187-197].

Most active microvalves actuate mechanical moving parts using magnetic [3-13], electric [16-27], piezoelectric [29-38], thermal [39-57] or other actuation methods [58-66]. The microvalves for pressure or flow control normally employ magnetic actuation in the form of solenoids to drive membranes or pistons, since they can generate large forces and deflections rapidly. For small structures, electrostatic actuation becomes more attractive. However, it is difficult to achieve high forces and large deflections because of the extremely high voltages required. Piezoelectric actuation can provide very high forces, but very small deflections even with the high voltage. Thermal actuation provides large forces via large strokes, but is slow in response and may not be appropriate for certain fluids due to heat dissipation. Bistable actuation is ideal in terms of power consumption, since it requires power only during the change between two stable modes. Bistable actuation device is capable of changing its operating condition between a stable rest position and a stable work position.

Table 1-3: Phase change microvalves [1].

Reference	Type	Phase change material	Valving channel	Mode	Fluid	Time	Pressure (kPa)	Power
Liu et al [74]	Hydrogel (2D)	pH sensitive hydrogel	In-line PDMS	NO	pH buffers	12 s	390	
Liu et al [74]	Hydrogel (3D)	pH sensitive hydrogel	In-line PDMS	NO	pH buffers	19 s	184	
Baldi et al [76]	Hydrogel	Glucose sensitive hydrogel	PDMS membrane with a Si bump	NO	Glucose	32 min (O) 18 min (C)		
Baldi et al [76]	Hydrogel	pH sensitive hydrogel	PDMS membrane with a Si bump	NO	pH buffers	7 min (O) 13 min (C)	5.9	
Richter et al [78]	Hydrogel	Temperature sensitive hydrogel (T _c = 34 °C, swelling at T < T _c)	In-line Si	NC	Methanol	0.3 s (O) 2 s (C)	840	0.2 W
Yu et al [79]	Hydrogel	Temperature sensitive hydrogel (T _c = 32 °C, swelling at T < T _c)	In-line glass	NC	Water	3.5 s (O) 5 s (C)	1380	
Liu et al [85]	Sol-gel	Pluronics sol-gel (T _c = 5 °C, liquid at T < T _c)	In-line PC	NC	PCR mixture		138	
Tashiro et al [86]	Sol-gel	Methylcellulose sol-gel (T _c = 55 °C, liquid at T < T _c)	In-line glass/Si	NO	Methyl-cellulose	1 s		2 W
Carlen and Mastrangelo [87]	Paraffin	Logitech bonding wax (T _m = 72 °C, volume expansion)	Parylene membrane	NO	Gas			0.05–0.15 W
Selvaganapathy et al [88]	Paraffin	Logitech bonding wax (T _m = 72 °C, volume expansion)	Parylene membrane	NO	DI	15 ms	160	0.04 W
Klintberg et al [91]	Paraffin	Paraffin (T _m = 45 °C, volume expansion)	Corrugated silicon membrane	NO	Gas			
Pal et al [92]	Paraffin	M1595 wax (T _m = 85 °C, phase change)	In-line glass/Si	B	PCR mixture	2 s	1725	0.015 W
Liu et al [93, 94]	Paraffin	Paraffin (T _m = 70 °C, phase change)	In-line PC	B	PCR mixture	10 s	275	
Gui et al [95]	Ice	Water (phase change)	In-line	NO	Water	15 s (C)		5 A
Yoshida et al [96]	Electro-rheological	ER fluids (viscosity change)	In-line	NO	ER	0.2 s	60% of supply pressure	4 kV mm ⁻¹
Hartshorne et al [99, 100]	Ferrofluid	Ferrofluids (600 cP)	In-line	NO	DI	15–30 s	12	
Oh et al [101]	Ferro-wax	Paraffin-based ferrofluids (T _m = 68 □ 74 °C, phase change)	In-line	B	DI	3 s	345	

NC: normally closed microvalve, NO: normally open microvalve, B: bistable, ER: Electro-rheological material, DI: deionized water, O: opening, C: closing

Table 1-4: Pneumatic microvalves (Externally operated microvalves) [1].

Reference	Type	Mode	Applications	Thickness (μm)	Pneumatic pressure (kPa)	Vacuum pressure (kPa)	Resistible pressure (kPa)
Takao et al [111]	Membrane	NC or NO	Pressure amplification	10	-80 to + 80		
Mathies group [114–116]	Membrane	NO	PCR	150	69–83	4	
Mathies group [117, 118]	Membrane	NC or NO	PCR	254	40	80	
Go and Shoji [120]	Membrane	NO	On/off switching		10		
Kanai et al [121]	Membrane	NO	On/off switching	30	20		
Lee et al [122]	Membrane	NO	On/off switching	200			
Baek et al [123]	Membrane	NO	On/off switching	200			
Hosokawa and Maeda [124]	Membrane	NC	On/off switching	25		60	10
Taylor et al [125]	Membrane	NO	On/off switching		138		
Yuen et al [126]	Membrane	NC or NO	On/off switching			By manual screwing	690
Quake's group [127, 128]	In-line	NO	On/off switching	10	60		
Studer et al [130]	In-line	NO	On/off switching		100		
Wheeler et al [131]	In-line	NO	On/off switching		140		
Wang et al [133]	In-line	NO	On/off switching		200–550		
Rolland et al [139]	In-line	NO	On/off switching		170		

NC: Normally closed, NO: Normally open, PCR: Polymer chain reaction

Table 1-5: Passive check microvalves with mechanical moving parts, such as flaps, membranes or balls [1].

Reference	Type	Actuator	Fluid	Valve size (μm)	Orifice size (μm)	Forward flow		Reverse flow	
						Flow rate (μlmin^{-1})	Applied pressure (kPa)	Flow rate (μlmin^{-1})	Applied pressure (kPa)
Zengerle et al [140, 141]	Flap (cantilever)	ES		$1700 \times 1000 \times 5$	400×400				
Xu et al [142]	Flap (cantilever)	SMA		$3300 \times 1200 \times 12$	700×2500				
Yang et al [143]	Flap (bivalvular)	None	DI	$780 \times 1580 \times 2$	25×1580	1600	4.50		4
Oosterbroek et al [149]	Flap (duckbill-like)	None	L	$1000 \times 300 \times 5$		192	30.42		30
Sim et al [150]	Flap (cantilever)	TP	DI	$1300 \times 1000 \times 2$	350×350	470	1.39		1
Yun et al [151]	Flap (cantilever)	C	DI	$660 \times 310 \times 2.2/0.3$	180×180	800	0.74		0.3
Paul and Terhaar [152]	Flap (hinged)	None	G	$\varnothing 2200 \times 150$	$\varnothing 1500$			Diodicity: 1.7	
Paul and Terhaar [152]	Flap (bridged floating)	None	G	$\varnothing 2200 \times 150$	$\varnothing 1500$			Diodicity: 12.8	
Feng and Kim [153]	Flap (cantilever)	PE		3					
Li et al [154]	Membrane (bridge)	PE	DI	$300 \times 300 \times 10$	$\varnothing 200$	1080 000	345		
Bien et al [155]	Membrane (bridge)	None	M	$400 \times 400 \times 2.5$	100×100	2500	11.85		11
Hu et al [156]	Membrane (bridge)	PE	DI	$960 \text{ (hexagon)} \times 50$	900 (hexagon)	35 600	65.5 0.01		600
Feng and Kim [153]	Membrane (bridge)	PE		4					
Chung et al [157]	Membrane (bridge)	None		$\varnothing 1200 \times 6$					
Nguyen et al [158–160]	Membrane (bridge)	PE	DI	$\varnothing 1000 \times 100$		2500	3 1200		3
Wego et al [161, 162]	Membrane (hole)	TP		$\varnothing 5000 \times 7.8$				Forward resistance: 950 kPa min μl^{-1}	
Bohm et al [163]	Membrane (hole)	PE or EM		$\varnothing 2500 \times 7$	$\varnothing 200$	2000	2.5		
Santra et al [164]	Membrane (hole)	EM		$\varnothing 4700 \times 100$	$\varnothing 200$			Forward resistance: 0.0475 kPa min μl^{-1}	
Jensen and Gravesen [165]	Membrane (bump)	None		$11\ 000 \times 11\ 000 \times 50$	1500×1500	200 000	70		
Carrozza et al [167, 168]	Ball	PE		$\varnothing 1200$	$\varnothing 500$				
Yamahata et al [169]	Ball	EM	G	$\varnothing 700$		20 000	10 1000		40
Pan et al [170]	Ball	EM	DI	$\varnothing 800$	$\varnothing 560$		<1		5–30

EM: Electromagnetic, ES: Electrostatic, PE: Piezoelectric, TP: Thermo-pneumatic, SMA: Shape memory alloy, M: Membrane, B: Bistable, NO: Normally open, NC: Normally closed, I: Inlet, OL: outlet, C: closing, O: opening, G: Gas

The presented active microvalves without mechanical moving parts are based on electrochemical [67-71], phase change [72-94], and rheological [95-101] actuations. Electrochemical actuation by electrolysis can provide large forces and deflections with relatively low voltages. The phase change actuation uses materials such as hydrogel [72-84], sol gel [85, 86] and paraffin [85-92]. Phase change actuation consumes energy in the form of thermal, pH, electric fields or light, and is very useful in disposable biochip applications due to its relatively low cost. Electro or magneto-rheological materials can be used as movable plugs remotely controlled by electric or magnetic fields. Large forces can not be produced by these actuation principles due to indirect magnetization or polarization by the external fields.

In the life sciences and chemistry applications, the microvalves have one of the most promising applications. Sealing of bio and chemical reagents without leakage even at high input pressure and on/off switching is a critical feature in ensuring successful biochemical analysis. If there exists leakage through the microvalves, leaking reagents contaminate each other and eventually influence the analysis. Also, it is imperative that the microvalves should tightly seal reaction chamber, in order to prevent evaporation of reagents and air bubbles generation at an elevated reaction temperature. In practice, microvalves using external systems, such as modular and pneumatic microvalves, are very useful due to their excellent performance in on/off switching or sealing [102-139]. Till today, the pinch type microvalves with external actuation forces by indirect contact with any flexible polymer based membranes [111-126], in-line channels [104,105, 127-139] or tubes [8] integrated on the disposable Lab on chip have been preferred, often because they can provide zero leakage and large resistible pressure, eliminating the risk of contamination. But in most of the cases miniaturization is difficult due to the requirement of additional external systems.

While active valves control flow rate by pressure differences and have complex structures due to their various actuation principles, passive valves only open to forward pressure and have simple structures, showing diode-like characteristics. In the reverse flow direction the efficiency of passive valves is relatively poor, since the performance of these check valves depends on input pressure. This lack of efficiency results in leakage at low pressure. Despite this drawback, most passive microvalves are incorporated as check valves in inlets and outlets of reciprocal displacement micropumps: flaps [140-152], membranes [154-165], spherical balls [167-170], mobile structures [171-173], nozzles [174-179], diffusers [180-184] or Tesla elements [185,186]. In addition, passive microvalves using capillary effects are sometimes useful for microfluidic applications since autonomous and spontaneous valving can be realized due to the geometry [187-195] and surface properties [196,197] of the microchannels. These passive capillary valves are recommended to block and pass fluidic flows without sealing at elevated temperatures.

There are several disadvantages for the mechanical active microvalve or passive check valves integrated with micropumps such as unavoidable leakage and relatively high cost due to their complicated structures. Though leakage becomes a critical feature for on/off switching applications, it is not critical for flow regulation applications. Therefore, many micromachined active microvalves were used for gas or selected liquid regulation [3-6, 8, 10, 14, 16, 17, 20-23, 29, 30, 32, 33, 35-39, 44, 45, 53]. In these applications, an important issue is the linear operation over wide ranges of pressures or flow rates with low power. For life sciences applications, non-mechanical active or capillary passive microvalves are preferred due to the possibilities of low cost and easy integration into the lab on chip devices, as well as

miniaturization of instruments. If the size of the instruments does not matter, microvalves using external systems are recommended [102-139]. For example, on/off switching and sealing in polymer chain reaction systems have been successful using these non-mechanical active microvalves [92–94], modular microvalves [102, 103] and pneumatic microvalves [144–117, 134–136].

1.4 Conclusions

In recent years, progress about the design and development of the microvalves has been very fast. As a result the performance the microvalves has been regularly improved and features such as leakage flow, workable pressure, power consumption, response time and biochemical compatibility have been partially addressed and solved. However there is plenty of room for improving the performance of the microvalves and making them cost effective for further commercialization.

All of these valves demonstrate very good properties for special applications such as flow regulation, on/off switching, or sealing of biomolecules, micro or nano-particles, chemical reagents, oils, water, bubbles, gases, vacuum, and many others. The preferred characteristics of microvalves include no leakage, controlled flow for high inlet pressures, control flow at different intermediate states with certain precision such as with 1-2% of full scale flow, less power consumption, large pressure resistance, insensitivity to particular contamination, fast response time, potential for linear operation, ability to control the flow for different pressure regimes with single design. Additionally, the existing valves are not capable of controlling the flow without power consumption at different intermediate states during valve operation. To fulfill all these requirements, various approaches have been explored in the development of the microvalves. Apparently there is no such microvalve that favors/accommodates all applications.

To fulfill all the aforesaid requirements, a new approach based on fine and micro-machining has been adopted and presented in the following chapter.

1.5 Outline of the thesis

The research presented in this thesis is focused on the development of gas microvalve based on fine- and micromachining. A novel concept of combination of fine- and micromachining is introduced to design and develop a microvalve which offers the benevolent features of fast response, controlled flow rates at high inlet pressure, no leakage, low power consumption, ability to control the flow for different pressure regimes, large pressure resistance and process gas isolation from actuator. In the following a chapter by chapter of the thesis is given:

In chapter 2 design and modeling of the microvalve based on the combination of fine- and micromachining is presented. Based on the requirements, different designs are considered and numerical simulations are performed to improve the design parameters for better valve operation.

Chapter 3 comprises the work out on the fabrication and the characterization of the stepper motor actuated microvalve based on the modeling details presented in chapter 2.

Chapter 4 is based on the characterization of piezoelectric actuated microvalve. This chapter provides a complete overview about the improved performance of the microvalve with the use of piezoelectric actuator.

In chapter 5 further development of microvalve is presented. In order to accommodate more than one pressure regimes in one design, a new design concept of pressure regulation is introduced. This chapter comprises the design, fabrication and characterization of a pressure regulator microvalve.

Chapter 6 focuses on the development of the fusion bonded fluidic interconnects. In this chapter a new technique is presented which establishes a reliable packaging technology for the connection of MEMS components which operate even at more than 600 °C. This new approach differs from the previous techniques as the interconnections are realized by the direct fusion bonding of glass tubes to the silicon.

Chapter 7 presents the conclusions based on the findings in all the chapters.

Chapter 2

2 Design and Modeling

Abstract

In this chapter design and the simulation of the stepper motor actuated microvalve based on the combination of fine- and micromachining are presented. A study for different designs is carried out by using an incompressible gas flow model. Additionally numerical simulations for a compressible flow models are performed for the improvement of the design parameters for better valve performance.

2.1 Introduction

The development of microfluidic systems for biological and chemical applications has been progressing rapidly in recent years. Typically a microfluidic device consists of pumps, conduits, connectors, actuators and valves. A fully functional valve is a key component in many microfluidic systems. A microvalve basically consists of three major components: an inlet orifice for fluidic flow, a membrane/cantilever beam to open or close the orifice and an actuator to provide the actuation force.

The application of the microvalves include flow regulations, sealing of gases, vacuum, chemical reagents and micro or nano particles, on/off switching and many others. To meet these requirements, there has been variety of actuation mechanisms and methods employed for construction of microvalves including magnetic [2-13], electric [16-27], piezoelectric [29-38] and thermal [39-57]. Conventional valves for pressure or for flow control normally employ magnetic actuation as they can generate large forces and deflections swiftly. Electrostatic actuation becomes more attractive for its miniaturized structures. But it requires extremely high voltages to achieve high force and deflections. Similarly piezoelectric actuation can offer very high forces but very small deflection with very large voltages. In case of thermal actuation, it can provide large forces by means of large strokes but slow in response. It might not be appropriate to use thermal actuation for many fluids due to heat dissipation. In terms of power consumption bistable actuation is preferred as it requires power only during the transition between two stable modes.

Microvalves also employ other actuation methods such as electrochemical [67-71], hydrogel [72-84], paraffin [87-95]. In the electrochemical actuation, large force and deflection can be obtained by electrolysis with relatively low voltage. The use of hydrogel and paraffin actuation methods consumes energy resources such as temperature, light, pH and electric fields and are advantageous for their relatively low cost.

Using external systems [102-131] is promising approach in designing microvalves. It is advantageous with no leakage flows at high input pressures. It is difficult to miniaturize the system due to the requirement of an additional external system.

Though all the presented microvalves exhibit excellent properties for certain applications such as flow regulation, sealing of fluids, pressure regulation and many others but still there is plenty of room to improve the performance of the microvalve. The key areas to improve the performance of the valve include no leakage, controlled flow for high inlet pressures, control flow at different intermediate states with certain precision such as with 1-2% of full scale flow, less power consumption, large pressure resistance, insensitivity to particular contamination, fast response time, potential for linear operation, ability to control the flow for different pressure regimes with single design. Additionally, the existing valves are not capable of controlling the flow without power consumption at different intermediate states during valve operation.

To accomplish all the aforementioned requirements, a new approach based on fine and micromachining has been adopted. This approach basically comes under the category of “active valves using external systems”. The important factors to adopt this approach are:

- Precise control of flow with a single valve design for different input pressures, ranging from 1 to 10 bar for different applications such as micro total analysis system, drug delivery, mixing and chemical analysis such as gas chromatography.
- No power consumption to control the flow at different intermediate states during valve operation.
- Flow control at different intermediate states with certain precision of 1-2 % of full scale flow.

A schematic cross-sectional view of the microvalve based on this concept is shown in Figure 2-1. The valve is composed of two main parts. The first is the fine machined actuation part. It includes a metal block along with a screw, which is rotated by the stepper motor (an electromagnetic actuator) mounted on a spring. The screw mechanism is used to convert the rotary motion of the stepper motor into the translational motion in order to deflect the membrane to control the gas flow. The second part is the microvalve based on standard micromachining techniques.

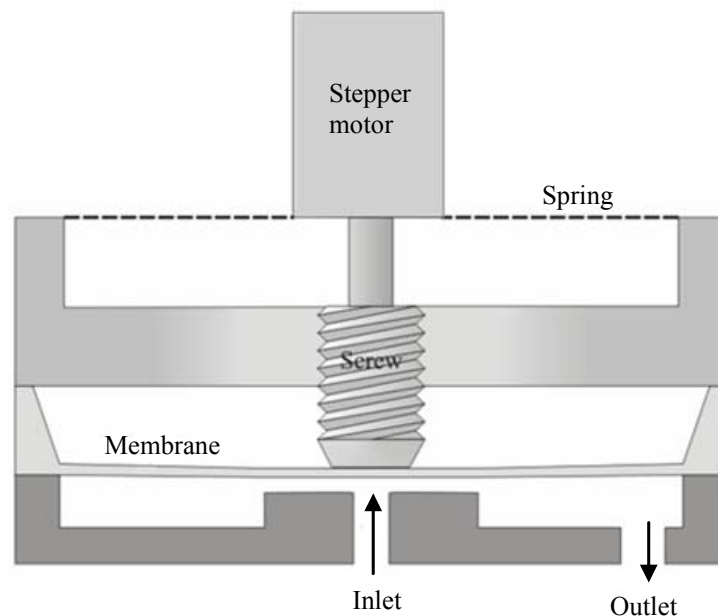


Figure 2-1: Schematic cross-sectional view of microvalve based on the combination of micro and fine machining.

This new approach provides the following benign features:

- It offers the control of flow at any intermediate state from open to close position.
- It is not an open and closed valve in a sense that there is no power required to keep the valve open at any desired state.
- The process gas is isolated from the actuation part.
- The screw which is intact with the membrane provides more strength to it to sustain high pressure.
- The specific configuration of microvalve is leak tight.

In this section design and modeling of the microvalve is described. Three different operational modes with different inlet pressures with their respective flows are considered for the designing of a microvalve (see Table 2-1). The operational modes are named according to their relevant flows and pressure differences in between the inlet and the outlet. The criterion to select the different operational modes is based on designing a single valve for different applications such as micro total analysis systems, drug delivery, mixing and chemical analysis such as gas chromatography. The microvalve needs to design in such a way that it can control the flow at any relative change to its inlet pressure. To derive the specifications of the valve an existing gas flow model based on the simple geometry shown in Figure 2-2 is used [198, 199].

2.1.1 Operational Modes

For different operational modes, flow resistance of the valve is calculated and given in the Table 2-1.

The resistance of the valve is calculated by:

$$R = \frac{\Delta P}{\varphi_v} \quad (1)$$

where R is the flow resistance [Pas/m^3], ΔP is the pressure difference [bar] between inlet and the outlet of the valve and φ_v is the volumetric flow rate [m^3/sec].

Table 2-1: Variable flow resistances for different operational modes.

Typical	Low flow high pressure	High flow low pressure
$P_1 = 5 \text{ bar}$	$P_1 = 10 \text{ bar}$	$P_1 = 1.1 \text{ bar}$
$P_2 = 1 \text{ atm}$	$P_2 = 1 \text{ atm}$	$P_2 = 1 \text{ atm}$
$\Delta P = 4 \text{ bar}$	$\Delta P = 9 \text{ bar}$	$\Delta P = 0.1 \text{ bar}$
$\varphi_v = 200 \text{ ml/min}$	$\varphi_v = 20 \text{ ml/min}$	$\varphi_v = 1500 \text{ ml/min}$
$\varphi_v = 3.33 \times 10^{-6} \text{ m}^3/\text{sec}$	$\varphi_v = 0.33 \times 10^{-6} \text{ m}^3/\text{sec}$	$\varphi_v = 25 \times 10^{-6} \text{ m}^3/\text{sec}$
$R = 120 \times 10^9 \text{ Pas/m}^3$	$R = 2700 \times 10^9 \text{ Pas/m}^3$	$R = 0.4 \times 10^9 \text{ Pas/m}^3$

It can be seen that the difference in resistances for different operational modes varies over three orders of magnitude. The resistance for the ‘Low flow high pressure’ mode is 6750 times larger than the resistance for the resistance for ‘High flow low pressure’ mode. It means that the valve should provide very high resistance during its operation at ‘Low flow high pressure’ mode and vice versa. In the next section, analysis for a simple geometry is presented to verify whether it is possible to fit all operational modes in one valve design or not.

2.1.2 Gas Flow Model

Figure 2-2 shows a typical design for the microvalve based on micromachining techniques. The arrows show the direction of the flow of gas. The gap height s changes with the membrane deflection. By changing the gap height s , the flow resistance is changed to

control the flow of gas through the valve. Assuming the flow is laminar, incompressible and fully developed, the variable flow resistance is calculated by [198, 199]:

$$R_v = \frac{6\mu \ln\left(\frac{a_2}{a_1}\right)}{\pi s^3} \quad (2)$$

where μ is dynamic fluid viscosity, a_1 and a_2 are the inner and outer radius of the valve seat respectively and s is the gap height.

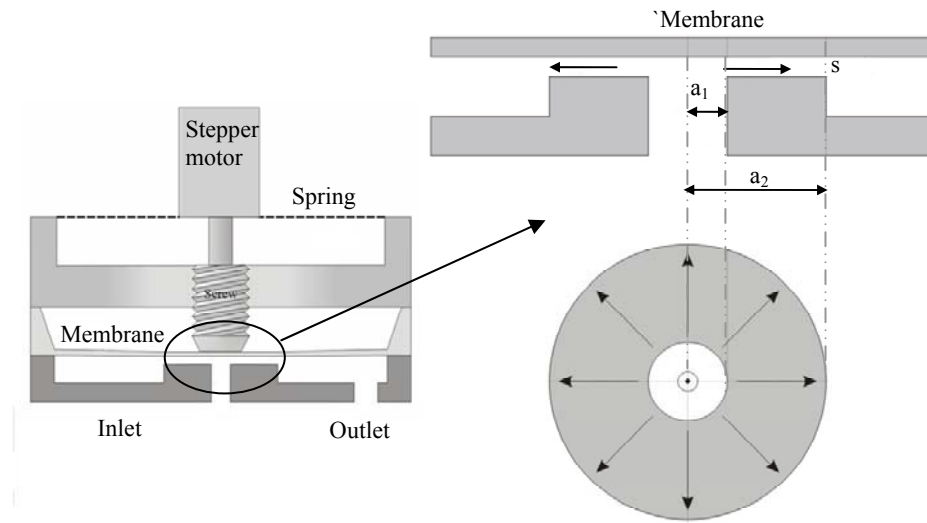


Figure 2-2: Circumferential flow model.

Flow rate can be calculated as:

$$\varphi_v = \frac{\pi \Delta P s^3}{6\mu \ln\left(\frac{a_2}{a_1}\right)} \quad [\text{m}^3/\text{s}] \quad (3)$$

$$\varphi_v = 60000 \varphi_v \quad [\text{l}/\text{min}] \quad (4)$$

To observe the flow behavior through variable resistance for different operational modes, a valve with typical dimensions of $a_1 = 0.2$ mm and $a_2 = 2$ mm is considered. Figure 2-3 shows the flow rates for different operational modes as a function of gap height s .

It can be seen that for the ‘Typical’ and ‘Low flow high pressure’ modes, the required flow reaches at a gap height of 3 μm and 9 μm respectively. It can also be observed that there is steep rise in the flow for a smaller change in the gap height. This non linear behavior of the flow through this particular valve geometry makes it difficult for any actuation principle to control the flow with the certain precision of 1-2 % of full scale flow with in the range of 3 and 9 μm . Hence the combination of stepper motor and screw mechanism (mechanical

transmission) is not precise enough to deflect the membrane to control the flow of gas precisely within this range. It is also obvious that only the ‘High flow low pressure’ regime has enough range to control the flow accurately as required because of larger flow range (see Figure 2-3).

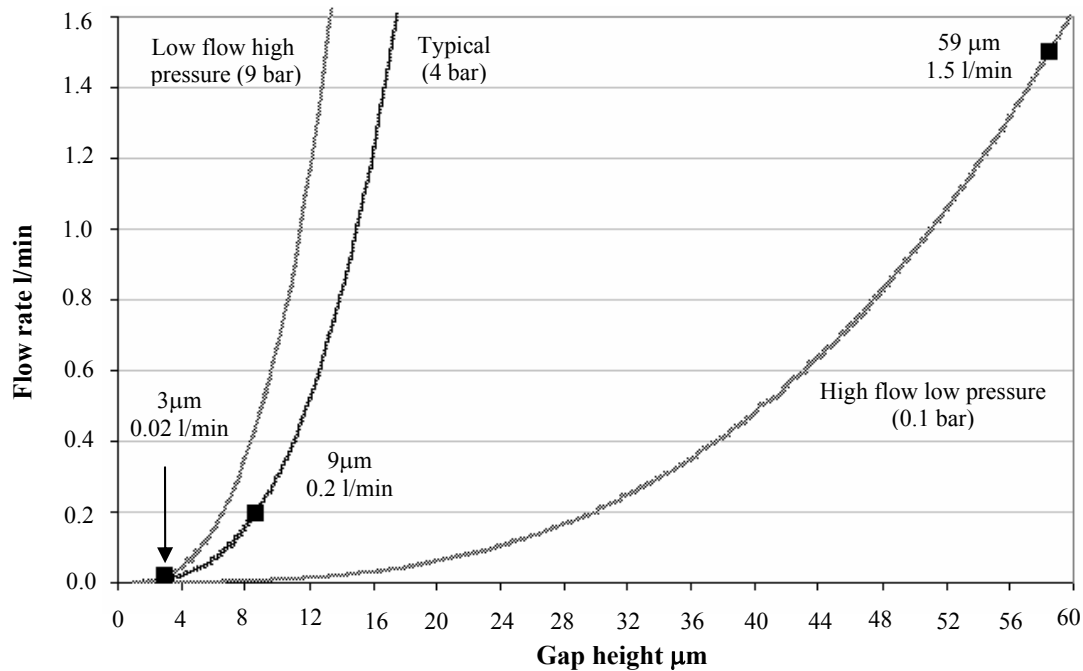


Figure 2-3: Flow behavior through variable resistance for three different operational modes. Flow reaches its desired value of 0.02, 0.2 and 1.5 l/min for a gap height of 3, 9 and 59 μm respectively for its respective modes.

The Mach numbers are also calculated through the variable resistance to examine whether the flow is compressible or not. The flow is termed as compressible if the Mach number is larger than 0.3. The compressible flow is not desirable as the communication of pressure information through out the flow is not unrestricted and not instantaneous. The compressibility effects on the important flow variable like the variation in the drag coefficient with Reynolds number and Mach numbers can severely influence the flow behavior by producing the step like discontinuities in the fluid flow which can directly affect the performance of the valve [200]. The Mach number can be calculated as:

$$Ma = \frac{V_m}{c_{air}} = \frac{\varphi_v}{c_{air} A_v} = \frac{\varphi_v}{c_{air} 2\pi a_1 s} \quad (5)$$

where c_{air} is the speed of sound in the air, V_m is the mean velocity and A_v is the smallest area where the gas flows through.

Figure 2-4 shows the Mach numbers for different operational modes. It can be examined that the Mach number exceeds the value of 0.3 for ‘Typical’ and ‘High flow low pressure’ modes for their required flow. Hence for ‘Typical’ and ‘High flow low pressure’ regimes the gas flow will be compressible. Compressibility effects have to be taken into

account as the Mach number exceeds the value of 0.3. Then the assumption of incompressible flow is no longer valid to predict the behavior of the microvalve.

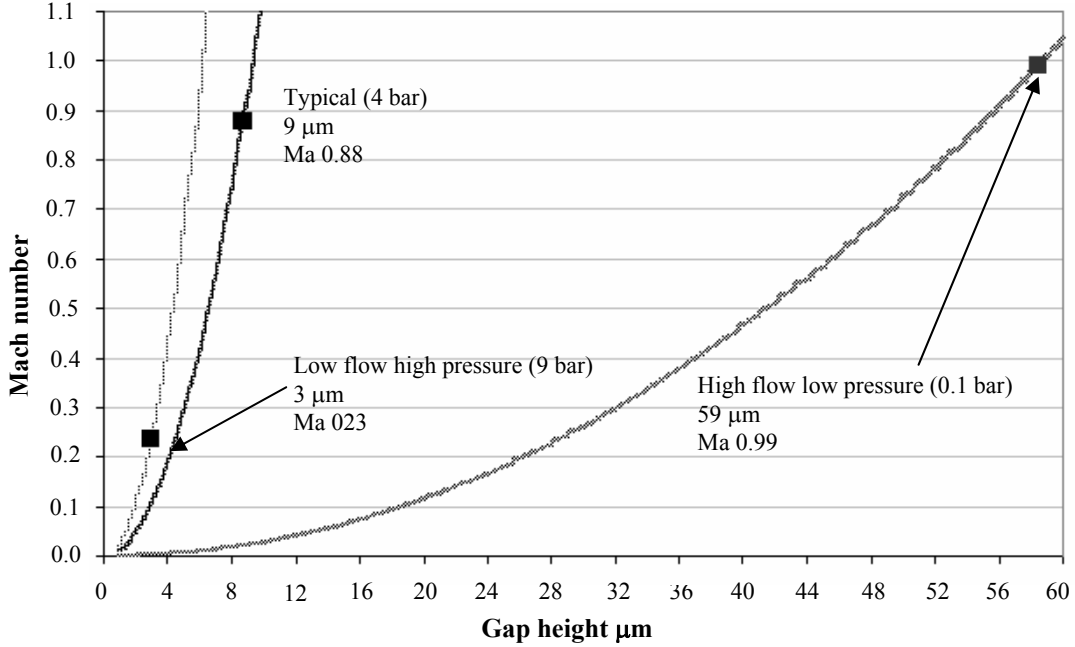


Figure 2-4: Mach number for Typical and High flow low pressure modes.

Reynolds number through variable resistance for different operational modes is also calculated to examine whether the flow is laminar or turbulent. The Reynolds number can be calculated as:

$$R_e = \frac{\rho V_m l}{\mu} \quad (6)$$

where ρ is the fluid density, V_m is the mean velocity, μ is the fluid dynamic viscosity and l is the characteristic length.

For a flow in a pipe for instance, the characteristic length is the pipe diameter if the cross section is circular, or the hydraulic diameter for a non circular section. The Reynolds number in case of non circular section is:

$$R_e = \frac{\rho V_m D_h}{\mu} \quad (7)$$

where D_h is the hydraulic diameter and for the variable resistance can be calculated as:

$$D_h = \frac{4A_v}{U_v} = \frac{2\pi a s}{\pi a} = 2s \quad (8)$$

where A_v is the smallest area where the gas flows through and U_v is the wetted perimeter.

The value of Reynolds number helps to predict the change in flow type. Generally if the value is less than 2100 then flow is termed as laminar and if it is more than 2100 then it is termed as turbulent. At smaller values of Reynolds number ($Re < 2100$) the fluid particles exhibits no instabilities and the flow is predictable. In case when Reynolds number is larger than 2100, then the flow is known as turbulent and exhibits instabilities and hence difficult to predict the flow behavior. The Reynolds number through variable resistance which is not a circular section can be calculated by equation 7. For the variable resistance the mean velocity is calculated by:

$$V_m = \frac{\varphi_v}{A_v} = \frac{\varphi_v}{2\pi as} \quad (9)$$

Reynolds number in the variable resistance are plotted and shown in Figure 2-5 as a function of gap height. It can be seen that the flow is laminar for all operational modes as the Reynolds number is always less than the 2100 for their equivalent gap heights.

From Figure 2-3, Figure 2-4 and Figure 2-5 it can be concluded that, to fit all operational modes in a single valve design is not possible. The difference in flow resistances is too large. In order to control the flow precisely, the operation range (gap height) has to be optimized for each mode. Additionally with these design parameters Mach number value is higher than 0.3 which is not desirable as the flow will be consider as compressible flow.

2.1.3 Additional resistance

In order to increase the operational range to control the flow more precisely, a static resistance in series with the variable resistance is introduced. The flow is now calculated by:

$$\varphi_v = \frac{\Delta P}{R_v + R_s} \quad (10)$$

where R_v is the variable resistance and R_s is the static resistance.

A static resistance is a simple channel of different shapes. The shapes and the equations to calculate the static resistances are given in Table 2-2. Depending on the operational mode, different channel shapes and dimensions are used. The value of the static resistance is chosen in such a way that the flow rate is limited just above the required flow rate. The static resistances for different operational modes are calculated and given in Table 2-3.

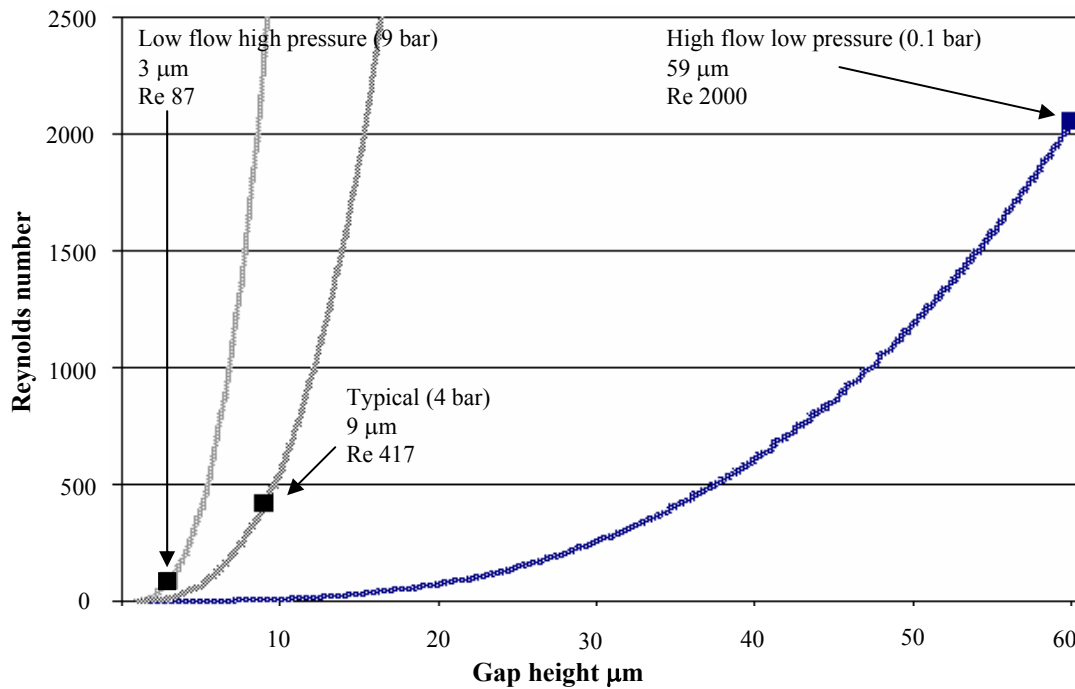


Figure 2-5: Reynolds number in variable resistance for all operational modes as a function of gap height.

Table 2-2: Channel shapes, hydraulic diameter, area and resistance for length l and a fluid dynamic viscosity [201].


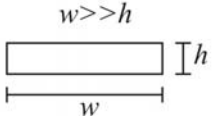
Shape	Hydraulic diameter D_h [m]	Area A [m ²]	Resistance R_s [Nsm ⁻⁵]
	h	h^2	$\frac{28.48l}{h^4} \mu$
	$2 \cdot h$	$h \cdot w$	$\frac{12l}{wh^3} \mu$

Table 2-3: Static resistances for different operational modes.

<u>Typical</u>	<u>Low flow, high pressure</u>	<u>High flow, low pressure</u>
Rectangular shape	Square shape	Rectangular shape
$l = 32 \text{ mm}$	$l = 21 \text{ mm}$	$l = 4.2 \text{ mm}$
$w = 400 \text{ }\mu\text{m}$	$h = 80 \text{ }\mu\text{m}$	$w = 1000 \text{ }\mu\text{m}$
$h = 60 \text{ }\mu\text{m}$	$R_s = 2600 \times 10^9 \text{ Ns/m}^5$	$h = 140 \text{ }\mu\text{m}$
$R_s = 110 \times 10^9 \text{ Ns/m}^5$		$R_s = 0.3 \times 10^9 \text{ Ns/m}^5$

Flow characteristic curves for all operational modes with different static resistances are shown in Figure 2-6. It can be seen that the flow in all operational modes is limited with the introduction of the static resistance. In fact, the static resistance controls the flow for the larger opening (gap height s) of the variable resistance: while for smaller opening variable resistance controls the flow. The combination of these resistances provides a larger range of deflecting the membrane for controlling the gas flow. The membrane can deflect 21 μm and 12 μm instead of 9 μm and 3 μm for ‘Typical’ and ‘Low flow high pressure’ modes respectively, which is important for better controllability.

It can also be observed that the introduction of static resistance in series with the variable resistance provides more linearity in each case. The linear part of the curve determines the smallest step needed to achieve the full scale control. Full scale flow control range for all operational modes is given in the Table 2-4. Figure 2-7 shows an enlarged part of the flow curve for ‘Typical’ operational mode. It can be seen that a flow rate change of 4 ml/min can be achieved with in a gap height change of 0.2 μm . The membrane has to be positioned above the valve seat with a precision of 0.2 μm to achieve the controllability of 4 ml/min. The plots for different operational modes to obtain minimum displacement for full scale control range are given in Appendix A.

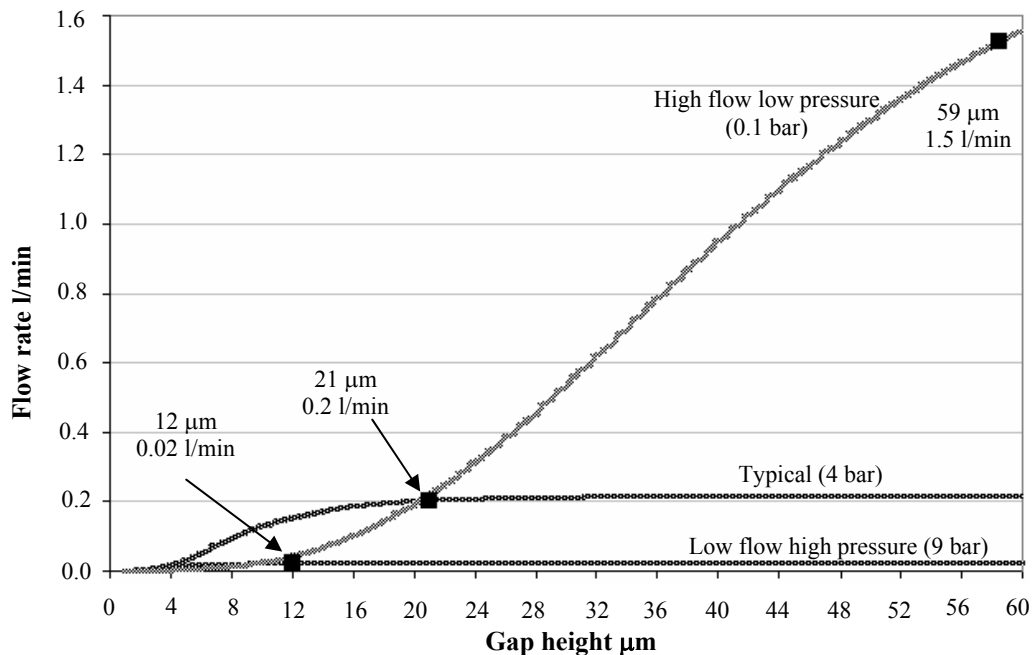


Figure 2-6: Addition of static resistance provides more controllable range and linearity in flow.

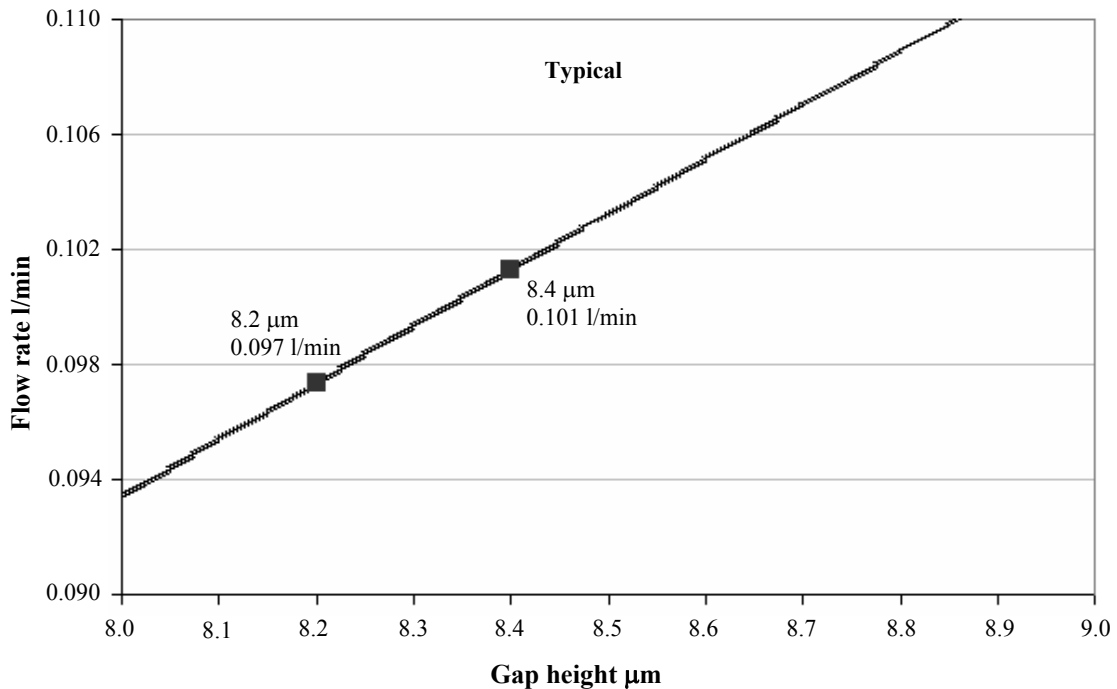


Figure 2-7: Enlarged view of typical flow behavior curve.

Table 2-4: Minimum displacements to achieve the full scale controllability for all operational modes.

Typical	Low flow high pressure	High flow low pressure
Flow range: 4-200ml/min	Flow range: 0.4-20 ml/min	Flow range: 30-1500ml/min
$\Delta_{\text{step}} = 0.2 \mu\text{m}$	$\Delta_{\text{step}} = 0.09 \mu\text{m}$	$\Delta_{\text{step}} = 0.8 \mu\text{m}$

2.2 Validity of the design model

For design and modeling of the valve for three different operational modes, it is assumed that flow is laminar, fully developed and incompressible. In order to check the validity of the modeling for the new design with static resistance in series with the variable resistance, the Mach number, the Reynolds number and the entrance lengths are calculated.

2.2.1 Mach number

The Mach number gives an indication about the compressibility of the gas flow. The Mach number in the static resistance and in the variable resistance is calculated by the following equations:

$$Ma_s = \frac{V_m}{c_{air}} = \frac{\varphi_v}{c_{air} A_s} = \frac{\varphi_v}{c_{air} wh} \quad (11)$$

$$Ma_v = \frac{V_m}{c_{air}} = \frac{\varphi_v}{c_{air} A_v} = \frac{\varphi_v}{2\pi as}$$

where V_m is the mean velocity, $A_s = wh \text{ m}^2$ and $A_v = 2\pi as \text{ m}^2$ are the areas of the static and the variable resistances respectively, w and h are the width and the height of the channel, a and s are the radius and the gap height of the variable resistance respectively.

Mach numbers for different operational modes with static resistance in series with the variable resistance are shown in Figure 2-8.

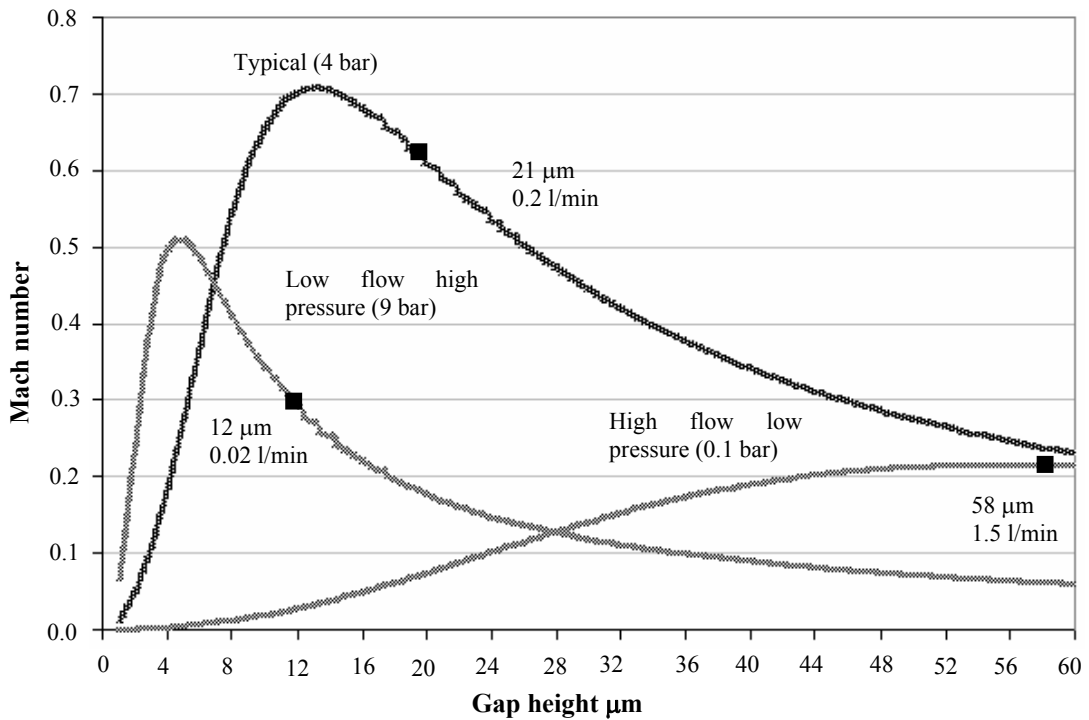


Figure 2-8: Mach numbers at the entrance of the variable resistance.

In Figure 2-8, Mach numbers at the entrance of the variable resistance as a function of gap height are plotted. By comparing Figure 2-4 and Figure 2-8 it can be seen that the introduction of static resistance considerably reduces the Mach number in all operational modes. It can also be observed that the Mach number increases as the valve starts to open and decreases as the valve is fully opened. When the valve is fully opened the value of the Mach number is less than the critical value of 0.3 in ‘Low flow high pressure’ and ‘High flow low pressure’ modes. But it is higher in ‘Typical’ mode. In order to have low Mach number for ‘Typical’ mode, the size of the static resistance and the orifice needs to be large which is not desired to miniaturize the valve.

2.2.2 Reynolds number

The Reynolds number provides information whether the flow is laminar or turbulent for the particular geometry. The Reynolds number in general can be calculated as:

$$R_e = \frac{\rho V_m l}{\mu} \quad (12)$$

where ρ is density, V_m is the mean velocity and l is characteristic length.

For a flow in a pipe for instance, the characteristic length is the pipe diameter, if the cross section is circular, or the hydraulic diameter, for a non circular section. The flow is assumed to be turbulent if the Reynolds's number is larger than 2100. The Reynolds number in case of non circular section is:

$$R_e = \frac{\rho V_m D_h}{\mu} \quad (13)$$

where D_h is the hydraulic diameter.

For the variable resistance in series with static resistance the mean velocity is calculated by:

$$V_m = \frac{\varphi_v}{A_v} = \frac{\varphi_v}{2\pi a s} \quad (14)$$

The hydraulic diameter of the variable resistance is calculated by:

$$D_h = \frac{4A_v}{U_v} = \frac{2\pi a s}{\pi a} = 2s \quad (15)$$

where A_v is the smallest area for the variable resistance where the gas flows through and U_v is the wetted perimeter.

Reynolds number in the variable resistance in series with the static resistance are plotted and shown in Figure 2-9 as a function of gap height. It can be seen that the flow is always laminar for all operational modes as Reynolds number is always less than the 2100.

Similarly Reynolds number for the static resistance is calculated and plotted in the Figure 2-10. It can be observed that only in case of 'High flow low pressure' mode the flow will be turbulent as the Reynolds number is higher than the 2100. The turbulent flow makes it difficult to control the flow precisely as flow will not be fully developed. In this case we can not use the specifications give in Table 2-3.

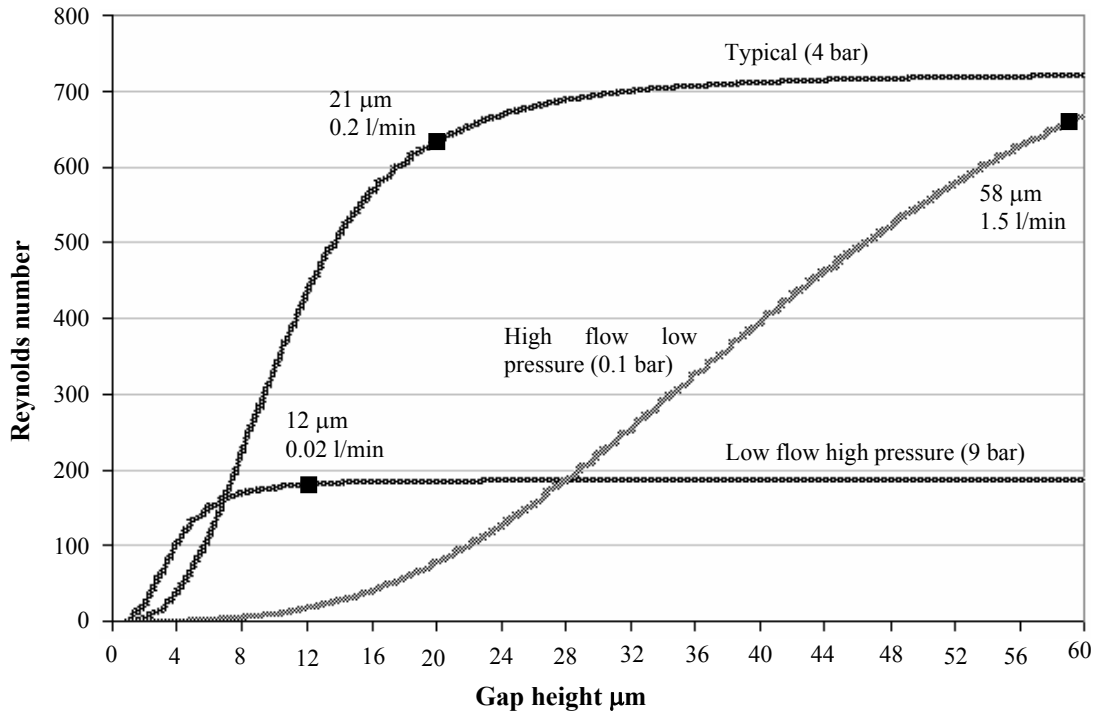


Figure 2-9: Reynolds number for variable resistance is always lesser than the 2000 in all operational modes.

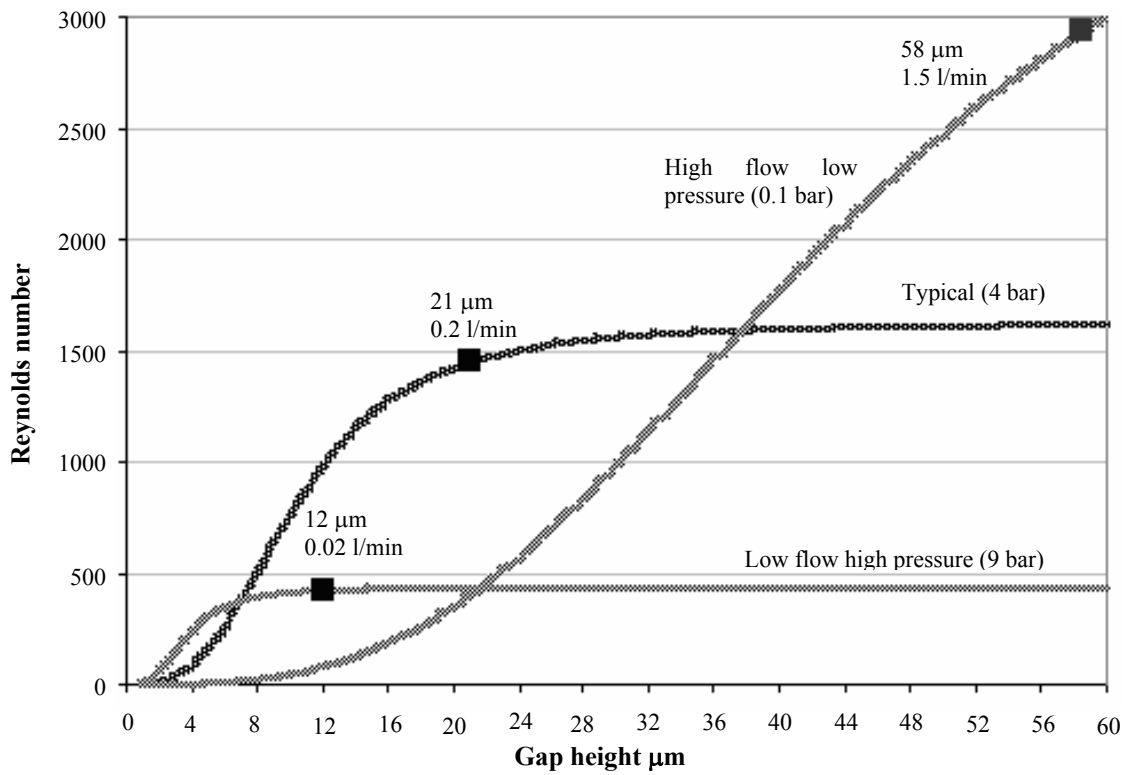


Figure 2-10: Reynolds number in the static resistance.

2.2.3 Entrance length

The entrance length provides the vital information for designing a channel or tube geometry for fully developed laminar flow. It is the channel length where the gas flow becomes fully developed. The conditions to have fully developed laminar flow: Reynolds number should be smaller than 2100, and the channel should be long compared to the entrance length of the flow. Actually besides the pressure drop across the entire region where the fully developed flow exists, there are also pressure drops in the entrance and the exit region of the channel or tube. It gives the information that how long a tube or channel should be, so that these entrance and exit effects can be neglected. The typical entrance lengths for a pipe are given by:

$$\frac{L_{el}}{D} = 0.06R_e \quad \text{Laminar flow} \quad (16)$$

$$\frac{L_{et}}{D} = 4.4(R_e)^{\frac{1}{6}} \quad \text{Turbulent flow} \quad (17)$$

The entrance length for a laminar flow entering a particular geometry with a hydraulic diameter D_h is given by [201]:

$$\frac{L_e}{D_h} = 0.59 + 0.056R_e \quad (18)$$

Figure 2-11 and Figure 2-12 show the entrance length in the variable and the static resistance respectively. For the ‘Typical’ and ‘Low flow high pressure’ modes, the entrance length is smaller than the channel length in both variable and static resistance. But in case of ‘High flow low pressure’ mode, the entrance length is larger than the channel length in both resistances. In this case flow will not be fully developed. In this case, incompressible flow model used can not provide the exact information about the precise control of flow.

2.3 Design parameter selection

In this paragraph, the design considerations which led to the dimensions of micromachined valve are addressed. The optimized parameters for all three operational modes are summarized in Table 2-5.

For the high pressure modes (Typical and Low flow high pressure), the dimensions of variable resistance are chosen as large as possible to achieve a low Mach number. The operational range is mainly determined by the inner radius of the valve seat a_1 . The area where the gas flows through becomes smaller and the Mach number increases (see eq. 5).

For ‘Typical’ mode, the dimensions of the static resistance are chosen by considering the length of the channel and Mach number. In order to obtain a low Mach number, cross sectional area should be larger but the channel has to be very long to provide the required resistance for better control of flow. So in order to fit the channel inside the size of 1 cm^3 , a channel length of 32 mm is selected to obtain linear flow behavior. In this case Mach number is higher than the 0.3.

For the ‘Low flow high pressure’ mode, the channel dimensions for the series resistance are arbitrary, because the values for the Mach numbers and Reynolds numbers are not exceeding the requirements.

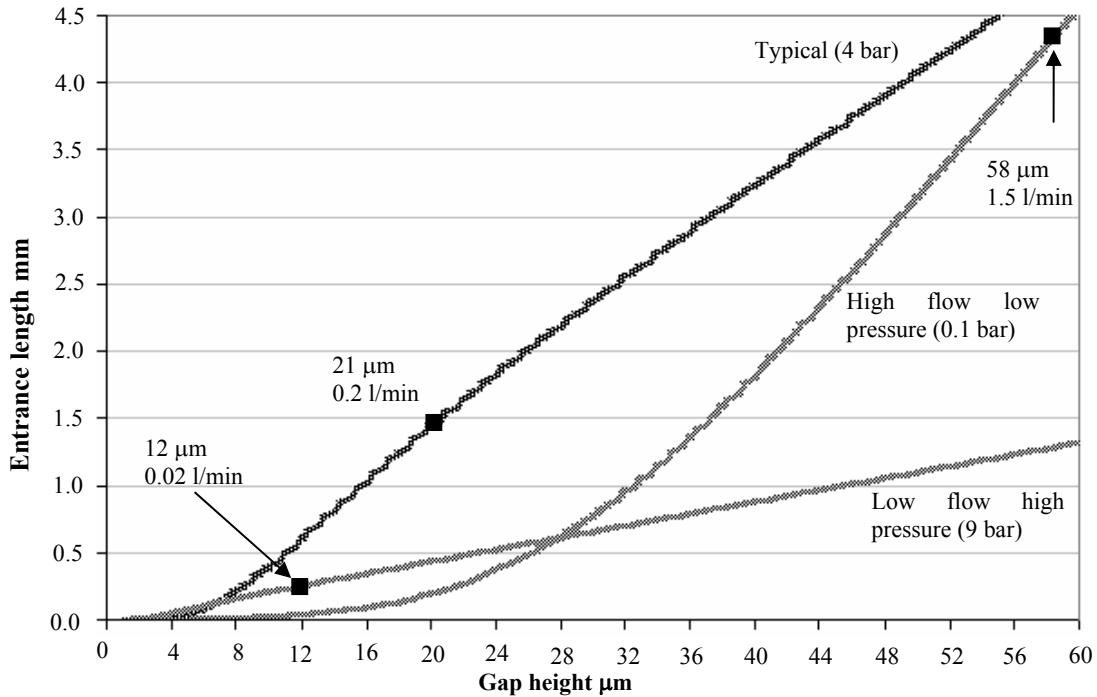


Figure 2-11: Entrance length is smaller than the channel length in variable resistance for all operational modes.

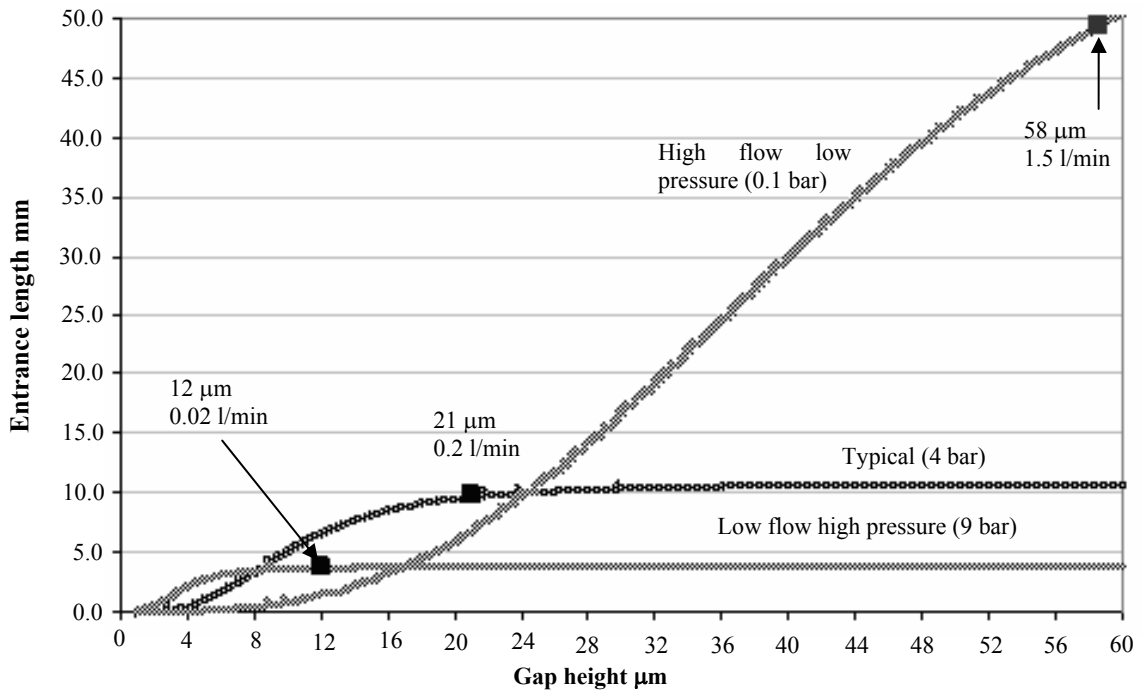


Figure 2-12: Entrance length is smaller than channel length in static resistance for all operational modes except ‘High flow low pressure’ mode.

Table 2-5: Optimized design parameters for all operational modes based on the incompressible flow model.

Operation mode	Typical $\Delta p = 4$ bar $\phi_v = 0.2$ l/min	Low flow, high pressure $\Delta p = 9$ bar $\phi_v = 0.02$ l/min	High flow, low pressure $\Delta p = 0.1$ bar $\phi_v = 1.5$ l/min
Variable resistance	$a_1 = 0.2$ mm $a_2 = 2$ mm $s_{max} = 20$ μ m $Ma_{max} \approx 0.65$ $Le \approx \frac{1}{2}(a_2 - a_1)$ Laminar	$a_1 = 0.05$ mm $a_2 = 2$ mm $s_{max} = 12$ μ m $Ma_{max} \approx 0.5$ $Le \ll (a_2 - a_1)$ Laminar	$a_1 = 1$ mm $a_2 = 2$ mm $s_{max} = 60$ μ m $Ma_{max} \approx 0.2$ $Le > (a_2 - a_1)$ Laminar
Static resistance	Rectangular ($h \gg w$) $w = 400$ μ m $h = 60$ μ m $l = 32$ mm $Le \approx 1/3l$ Laminar	Squared $h = 80$ μ m $l = 21$ mm $Le \ll 1$ Laminar	Rectangular ($h \gg w$) $w = 1000$ μ m $h = 140$ μ m $l = 4.2$ mm $Le \gg 1$ $\phi_v > 1200$ ml/min → Turbulent

For the ‘High flow low pressure’ mode, the dimensions of the variable resistance are chosen to control the required flow of 1.5 l/min within a gap height of 60 μ m. The gap height is determined by the maximum deflection of the membrane. Mach number is less than the value of 0.3. A rectangular channel is chosen for a series resistance to reduce the Reynolds number (see Figure 2-10). It can be seen that the flow is turbulent after 1200 ml/min.

It can be concluded from the modeling that a single valve which can operate in all the 3 different operational modes can not be made within a single design (see Table 2-5). In order to achieve this, the static resistance needs to be adjustable within the range of 3×10^8 till 2.6×10^{12} Ns/m⁵ (see Table 2-3). This is a very large range. Additionally the orifice radius a_1 of the variable resistance also needs to be changeable in the range of 50 μ m to 1mm. It seems to be very difficult to integrate all three operational modes in one design. For every mode, Mach number, Reynolds number and the entrance lengths are considered. The theoretical model is accurate when Mach number is less than 0.3, flow is laminar and entrance length is smaller than channel length. It seems to be impossible to define the single valve configuration which can accommodate all operational modes within these boundaries.

2.4 Fine machined part: Stepper motor and screw mechanism for mechanical transmission

In this paragraph the required torque to rotate the screw, the minimum displacement and the response time are calculated. In order to turn the screw, the stepper motor has to overcome the frictional forces. The frictional force is proportional to the force which presses the surfaces together as well as the roughness of the surfaces. There are two forces that have to be taken into account, the force due to tensile stress when the membrane is deflected to control the flow and the force due to pressure on the membrane. The force due to tensile stress on the membrane can be calculated by [202]:

$$F_{deflection} = \frac{s_d D}{0.0056 a_m^2} \quad (19)$$

where s_d is the deflection in the middle of the membrane, a_m is the side length and D is the flexural rigidity. D is given by:

$$D = \frac{Eh^3}{12(1-\nu^2)} \quad (20)$$

where E is the young's modulus, ν is the Poisson ratio and h is the thickness of the membrane.

The membrane parameters to calculate the tensile force are given in the Table 2-6.

Table 2-6: Design specifications for membrane to calculate the tensile force.

Thickness h	Deflection S_d	Side length a_m	Boss	Poison's ratio ν	Young's modulus E
50 μm	80 μm	7 mm	2 mm	0.25	170 MPa

The membrane with a thickness of 50 μm is preferred. The side length of the silicon membrane is taken as 7 mm as the valve should fit into the size of 1 cm^3 . The tensile force on the membrane due to bending is calculated as 540 mN.

The force on the membrane due to pressure is also an important parameter for designing the membrane. The membrane has to be strong enough to withstand the force due to different pressures for different operational modes. To calculate the force caused by fluid on the membrane, it is assumed that there is the static uniform pressure at the membrane above inlet ($a_1 = 0.2$ mm) as the valve is closed. It is approximated that the static pressure drops radially in the variable resistance as the valve opens. So with the boundary conditions $P(a_1) = P_1$ and $P(a_2) = 1$ bar, the force on the membrane is given by:

$$F_{pressure} = \pi a_1^2 \Delta P + \frac{1}{3} \pi \Delta P (a_2^2 + a_1 a_2 - a_1^2) \quad (21)$$

where $\Delta P = P_I - I$ is the pressure difference and a_1 and a_2 are the inner and the outer radii of the variable resistance respectively.

The total force is then given by:

$$F_{Total} = F_{pressure} + F_{deflection} \quad (22)$$

Where $F_{pressure}$ is the force on the membrane due to pressure and $F_{deflection}$ is the maximum tensile force due to deflection of the membrane.

The resulting pressure force and the total force for all operational modes are given in the Table 2-7. The bending force of 600 mN is used instead of 540 mN for safety.

In order to calculate the required torque to rotate the screw by stepper motor, frictional forces also have been taken into account. There are two contact points where the friction occurs. One is in between the screw threads and the second is in between the bottom of the screw and the silicon membrane. To calculate the friction between the bottom and the silicon membrane, it is assumed that the force per unit area on the bottom of the screw is uniformly distributed. The force per unit area is given by:

$$P_{bottom} = \frac{\mu_{membrane} F_{Total}}{\pi a_s^2} \quad (23)$$

where $\mu_{membrane}$ is the coefficient of friction between the membrane and the screw and a_s is the radius of the screw.

The torque needed to overcome this friction is given by:

$$T_{bottom} = 2\pi \int P_{bottom} r^2 dr = \frac{2}{3} P_{bottom} a_s^3 = \frac{2}{3} \mu_{membrane} F_{Total} a_s \quad (24)$$

The resulting torque to overcome the friction between the bottom of the screw and the silicon membrane boss is given in the Table 2-8.

Table 2-7: Total force acting on the membrane for all operational modes.

$F_{pressure} (N)$								
Typical			Low flow high pressure			High flow low pressure		
a_1 (mm)	0.2	1.88	a_1	0.05	3.86	a_1	1	0.084
a_2 (mm)	0.1		a_2	2		a_2	2	
Pressure (bar)	4		Pressure (bar)	9		Pressure (bar)	0.1	
$F_{total} = F_{pressure} + F_{deflection} (N)$								
1.88 + 0.6 = 2.48			3.87 + 0.6 = 4.47			0.084 + 0.6 = 0.684		

The torque needs to overcome the friction between the screw threads and the nut is given by:

$$T_{thread} = \mu_{thread} F_{Normal} a_s \quad (25)$$

where μ_{thread} is the coefficient of friction between the threads and the nut and F_{normal} is the force perpendicular to the upper plane of the thread (see Figure 2-13).

The normal force can be calculated by:

$$F_{Normal} = \cos(\varphi) \cos(\theta) F_{Total} \quad (26)$$

where φ is the angle between the normal force to the plane and the total force and θ is the angle between the screw threads.

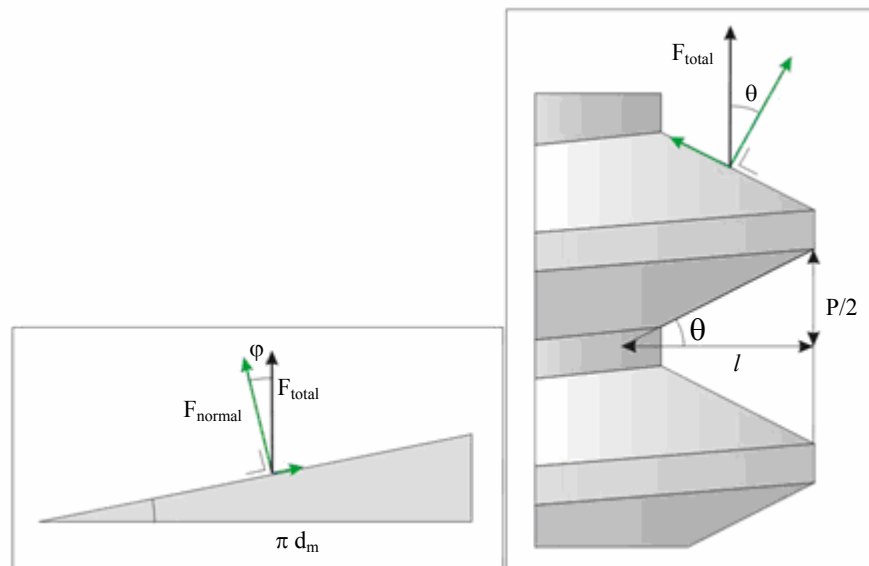


Figure 2-13: Specifications about screw threads.

To calculate the normal force, φ can be calculated as:

$$\varphi = \arctan\left(\frac{P_s}{\pi d_m}\right) \quad (27)$$

In equation 27, P_s is the pitch of the screw and d_m is the mean diameter of the screw. The minimum pitch and the diameter of the screw used to calculate the normal force are 0.4 mm and 2 mm respectively. This is the minimum pitch that can be realized by standard fine machining techniques. The normal force and the torque to overcome the frictional force due to this total force are given in Table 2-8.

The total frictional torque is then calculated for all operational modes and is given in Table 2-8.

$$T_{friction} = T_{thread} + T_{bottom} \quad (28)$$

It can be seen from Table 2-8 that the maximum total frictional torque is 3.34 mNm for ‘Low flow high pressure’ mode. The frictional torques for other operational modes are also given in the Table 2-8

Table 2-8: Total torque required to rotate the screw to control the gas flow.

Typical			Low flow high pressure			High flow low pressure		
T _{bottom} (mNm)								
F _{total} (N)	2.48	0.66	F _{total} (N)	4.47	1.032	F _{total} (N)	0.684	0.182
μ _{membrane}	0.4		μ _{membrane}	0.4		μ _{membrane}	0.4	
a _s (mm)	1		a _s (mm)	1		a _s (mm)	1	
T _{thread} (mNm)								
F _{normal} (N)	2.14	1.29	F _{normal} (N)	3.86	2.316	F _{normal} (N)	0.59	0.35
μ _{membrane}	0.6		μ _{membrane}	0.6		μ _{membrane}	0.6	
a _s (mm)	1		a _s (mm)	1		a _s (mm)	1	
T _{total} = T _{bottom} + T _{thread} (mNm)								
1.95			3.348			0.532		
T _{mottor} (μNm) for N = 120 and ε = 0.7								
23.15			40			6		

The corresponding torque required by the stepper motor to overcome the maximum frictional torque is calculated by:

$$T_{motor} = \frac{T_{friction}}{N\varepsilon} \quad (29)$$

where N is the gear reduction ratio and the ε is the efficiency of the gear box of the stepper motor.

The specifications of the smallest stepper motor shown in the Figure 2-14 are used to calculate the required torque [221]. It can be seen that the maximum torque of 40 μNm is required in case of ‘Low flow high pressure’ mode. And the stepper motor can provide a torque of 0.3 mNm which is 7 times higher than the maximum required torque.

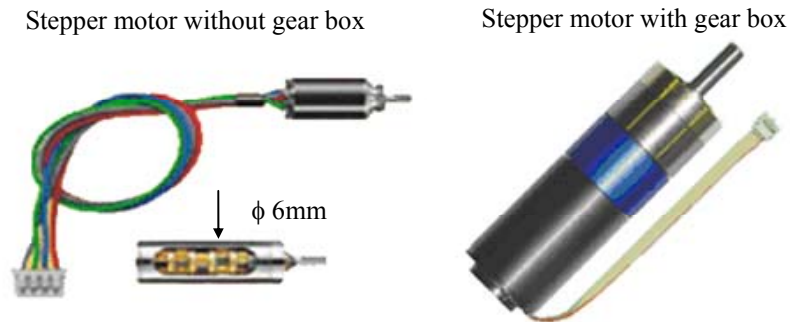


Figure 2-14: The stepper motor can provide the maximum torque of 0.65 mNm and 85 nm displacement per step.

The minimum displacement per step to achieve the full scale control of (1:50) flow for all operational modes is given in the Table 2-4. The minimum displacement per step that can be achieved with this stepper motor is calculated by:

$$\Delta_{steps} = \frac{P_s}{Nm} \quad (30)$$

where P_s is the pitch of the screw, N is the gear reduction ratio and m is the maximum number of steps per rotation taken by the stepper motor.

The minimum displacement step that can be achieved by the stepper motor is 83 nm which is precise enough to achieve the required controllability for all operational modes (see Table 2-9).

The number of steps required to open and close the valve is calculated by:

$$n = \frac{S_{open}}{\Delta_{step}} \quad (31)$$

where S_{open} is the gap height for open valve. The numbers of steps to bring the valve from open to close state are given in Table 2-9.

The response time to take the step is given by:

$$t_{response} = \frac{n}{v_m} \quad (32)$$

where v_m is the maximum velocity in steps per second that the stepper motor can provide. The response time is smaller than 50 ms for all operational modes (see Table 2-9).

Table 2-9: Minimum displacements, no. of steps and the response time of the stepper motor.

Minimum displacement			
P_s (mm)	0.4	Δ_{step} 83 nm	$\Delta_{step}=200$ nm (Typical)
M	40		$\Delta_{step}=90$ nm (Low flow high pressure)
N	120		$\Delta_{step}=800$ nm (High flow low pressure)
No of steps			
S_{open} (μ m)	20	$n = \frac{S_{open}}{\Delta_{step}}$	100 (Typical)
	12		133 (Low flow high pressure)
	60		75 (High flow low pressure)
Response time			
N	100	$t_{response} = \frac{n}{v_m}$	12.5 s (Typical)
	133		16.6 s (Low flow high pressure)
	75		9.45 s (High flow low pressure)
v_m (steps/sec)	8000		

The torque for all the operational modes required by the stepper motor is calculated and it is found that the AMD0620 stepper motor in combination with a gear box of 120:1 reduction ratio can provide the required torque. The stepper motor is of 6 mm in diameter and 9 mm in length. It is the smallest stepper motor available on the market which can provide the required torque to control the flow of gas. The displacement per step is also calculated and it is found that the stepper motor can also provide the required minimum displacement. Similarly the stepper motor can also provide a response time less than 20 ms.

It can be concluded that the smallest stepper motor AMD0620 in combination with a gear box of 120:0 can provide the following benevolent features:

- Enough torque to deflect the membrane to control the flow
- Minimum displacement per step to achieve the controllability of 1-2 % of full scale flow
- Response time of less than 20 ms

It is discussed in the section 2.3 that the Mach number exceeds the value of 0.3 as the valve is opening and then decreases down to the value less than 0.3 for the fully opened valve. As the Mach number exceeds the value of 0.3, compressibility effects have to be taken into account. In the following section the influence of the high Mach number on the behavior of the valve will be examined with numerical simulation.

2.5 Simulation

In order to observe the influence of the high Mach number on the behavior of the valve, numerical simulation has been performed. The gas flow through the variable resistance is simulated only, as it plays a critical role in controlling the flow rate. Instead of an incompressible gas flow, as it is assumed in the theoretical model, a compressible gas flow is simulated. The effect of a compressible gas flow on the volume flow is evaluated. The simulations are performed by using CFDRC software (Computational Fluid Dynamics).

The dimensions for the “Typical” operational mode are used for the simulation model (see Table 2-5). The valve seat has an inner radius a_1 of 0.2 mm and an outer radius a_2 of 2 mm.

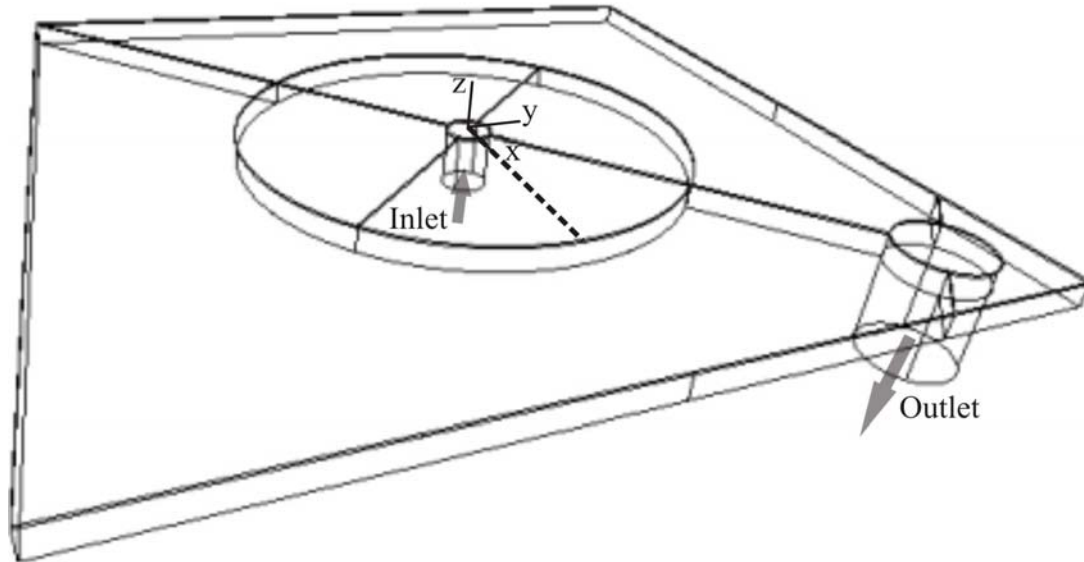


Figure 2-15: Valve structure used in simulation.

Figure 2-15 shows a three dimensional impression of the valve geometry used for the simulation. Five different geometries are made with different gap heights (20 μm , 16 μm , 12 μm , 8 μm and 4 μm).

To calculate the pressure drop over the variable resistance, “Typical” operational mode dimensions are used. A gap height of 15 μm is used as the highest Mach number appears at this gap height (see Figure 2-8). The values of the static and the variable resistances are given in the Table 2-10. The maximum pressure drop over the static and the variable resistance for their resistance values is calculated as 3.5 and 0.5 bar respectively.

It is assumed that the gas follows the ideal gas law. In Table 2-11 all the relevant simulation parameters are given. The calculated pressure drop of 0.5 bar over the variable resistance is used for the simulation.

The simulation results shown in Figure 2-16 provide the information about the total pressure, static pressure, density and the Mach number. The figures show the cross section of the z-plane. It can be observed that color changes in the portion of the variable resistance not in the chamber around it. It means that variable resistance determines the behavior of the valve.

Table 2-10: Calculated static and variable resistance.

Static resistance	Variable resistance
$R_s = \frac{12l\mu}{wh^3}$	$R_v = \frac{6\mu \ln(\frac{a_2}{a_1})}{\pi s^3}$
$14 \times 10^{10} \text{ Pas/m}^3$	$2.4 \times 10^{10} \text{ Pas/m}^3$

Table 2-11: Parameters used for simulation.

ΔP	Temperature	Dynamic viscosity
0.5 bar	293 °C	$1.82 \times 10^{-5} \text{ Ns/m}^2$

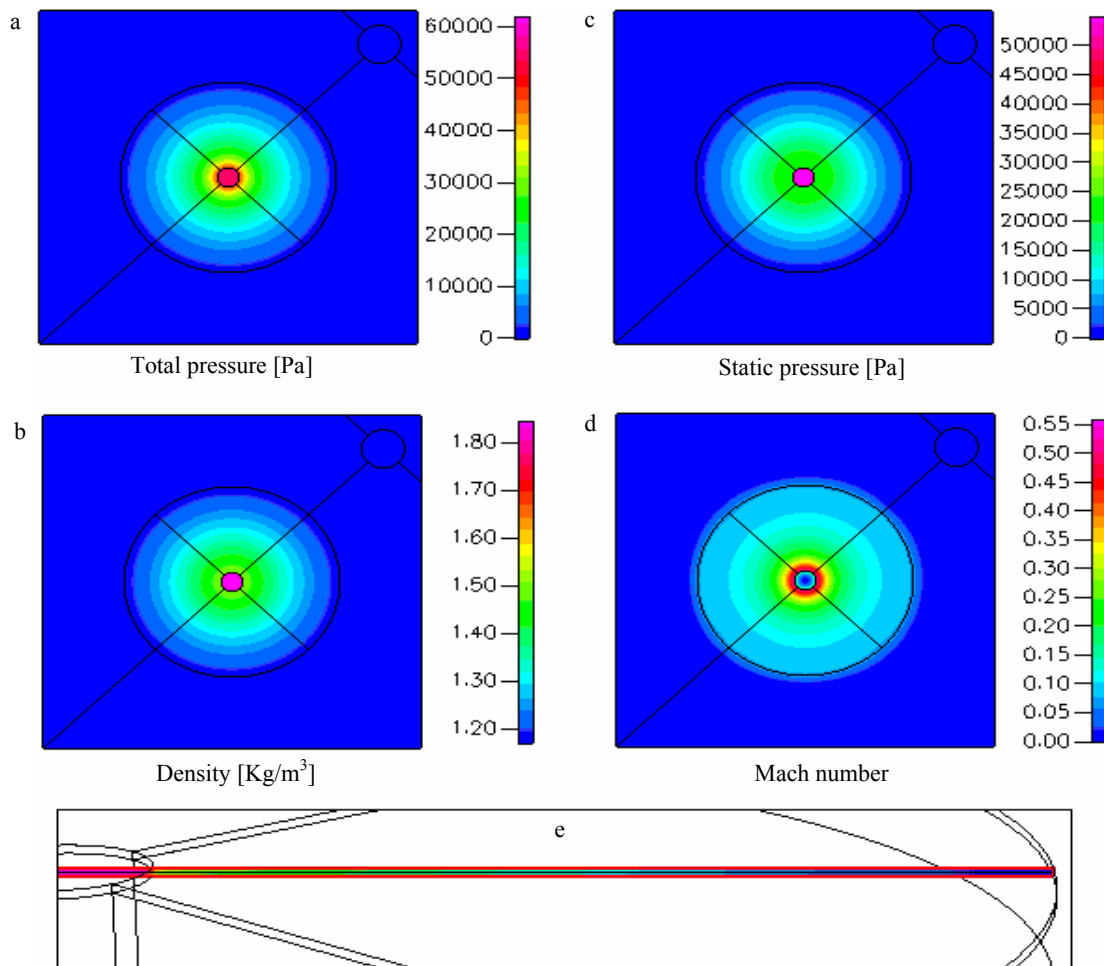


Figure 2-16: Simulation results a) Total pressure b) Static pressure c) Density d) Mach number e) Close up of variable resistance.

A close up of the variable resistance is also shown in Figure 2-16 e. The red rectangle marks a cross section of the y-plane, also indicated in Figure 2-15 by the dashed line. The color corresponds to the value of the variables (total pressure, static pressure, density or the Mach-number) at that point in the resistance. Plots for different variables such as the Mach number, velocity profile and for the density as a function of the radius are drawn. In the following section these plots are discussed. The mass flow is also calculated and compared with the theory.

2.5.1 Pressure

Figure 2-17 and Figure 2-18 show the total pressure and the static pressure respectively as a function of radius for different gap heights. The two plots can be related by the following equation:

$$P_{Total} = P_{static} + P_{dynamic} = P_{static} + \frac{1}{2} \rho V^2 \quad (33)$$

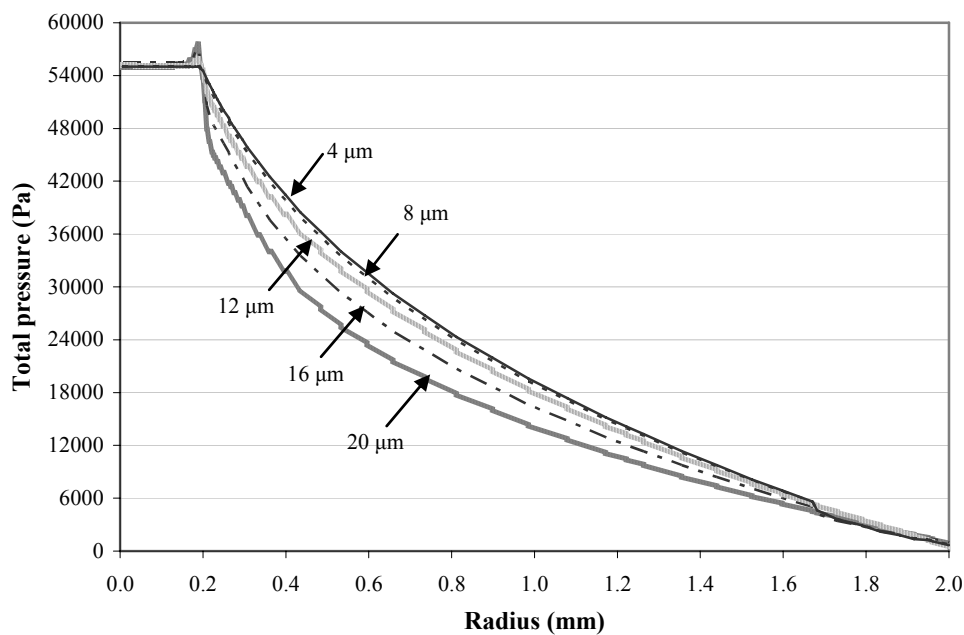


Figure 2-17: Total pressure as a function of radius for different gap heights.

From Figure 2-18 it can be seen that there is uniform static pressure at the membrane above the inlet ($r < 0.2$). The total force due to pressure is calculated by the equation 22 and is given in Table 2-7. The force on the membrane for different gap heights is calculated by the simulation and given in Table 2-12. It can be seen that when the valve is open the force on the membrane is smaller than when the valve is closed. In fact for the high flow rates the dynamic pressure is high. The dynamic pressure term reduces the static pressure which results in a smaller force on the membrane (see equation 33).

It can also be observed from Figure 2-18 that the static pressure drops faster than that $1/r$. That is why the simulated force is smaller than the calculated force (see Table 2-7 and Table 2-12). So the calculations are in the safer side.

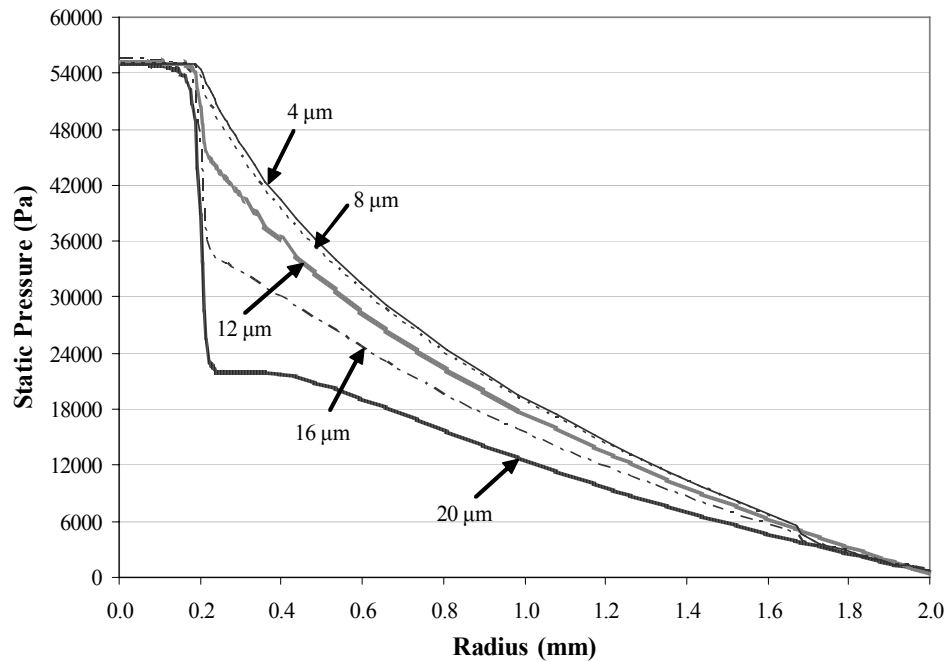


Figure 2-18: Pressure as a function radius for different gap heights.

Table 2-12: Simulated force on the membrane.

Gap height s μm	4	8	12	16	20
Force (N)	0.17	0.17	0.16	0.14	0.12

2.5.2 Mach number

To see compressibility effect on a gas flow, Mach number as a function of radius for different gap heights are plotted. Figure 2-19 shows the simulated Mach number as a function of the radius for different gap heights. The highest flow velocity is reached when the valve is fully open ($s = 20 \mu\text{m}$). According to the simulation, the maximum Mach number is approximately 0.5. From Figure 2-19 one can see that the highest Mach number occurs at a radius of approximately 0.22 mm. There is a direct relation between the static pressure and the Mach number, which can be seen from equation 33. As the valve is closed, the total pressure is the static pressure and as it starts to open, the velocity change results in large dynamic pressure which reduces the static pressure. In Figure 2-19 the simulated Mach number as a function of radius for a gap height of 20 mm is compared with the theory. The Mach number as a function of radius is calculated by [204]:

$$Ma(r) = \frac{1}{r} \frac{\Delta P s^2}{12 \mu \ln\left(\frac{a_2}{a_1}\right) c_{air}} \quad (34)$$

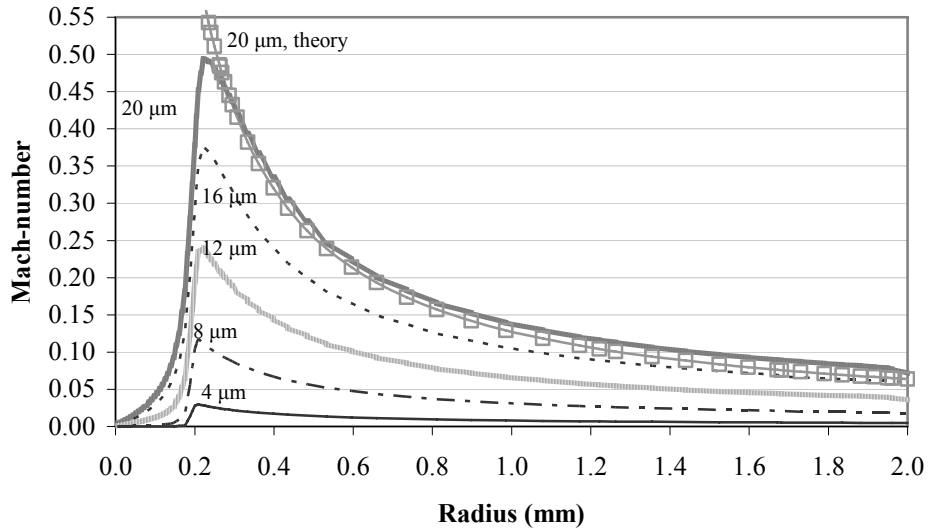


Figure 2-19: Mach number as function of radius for different gap heights.

It can be seen that the theory is quite accurate when comparing it with the simulation. Only in the beginning of the resistance (at a radius of $200 \mu m$) the theory is deviating from the simulation. This deviation is caused by the fact that the flow is not immediately fully developed at the entrance of the resistance. In theory a fully developed flow is assumed. The velocity profile is considered to give an indication when the flow is fully developed.

2.5.3 Velocity profile

The velocity profile is evaluated at several radii for a fully opened valve ($s=20 \mu m$) where the highest Mach number occurs. Figure 2-20 shows a cross section of the y-plane in the variable resistance. The color indicates the velocity in the r -direction at that certain point.

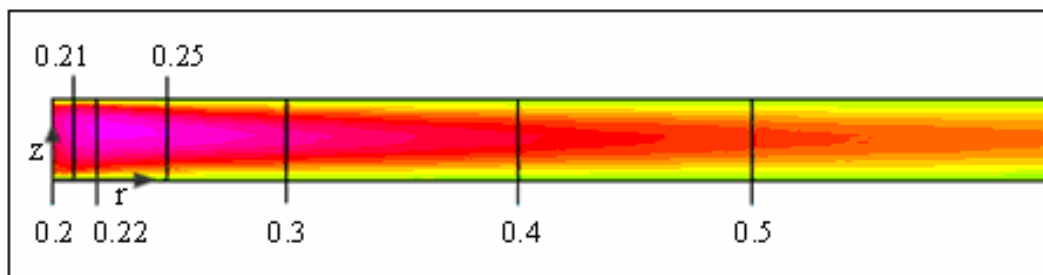


Figure 2-20: Velocity change at several radii.

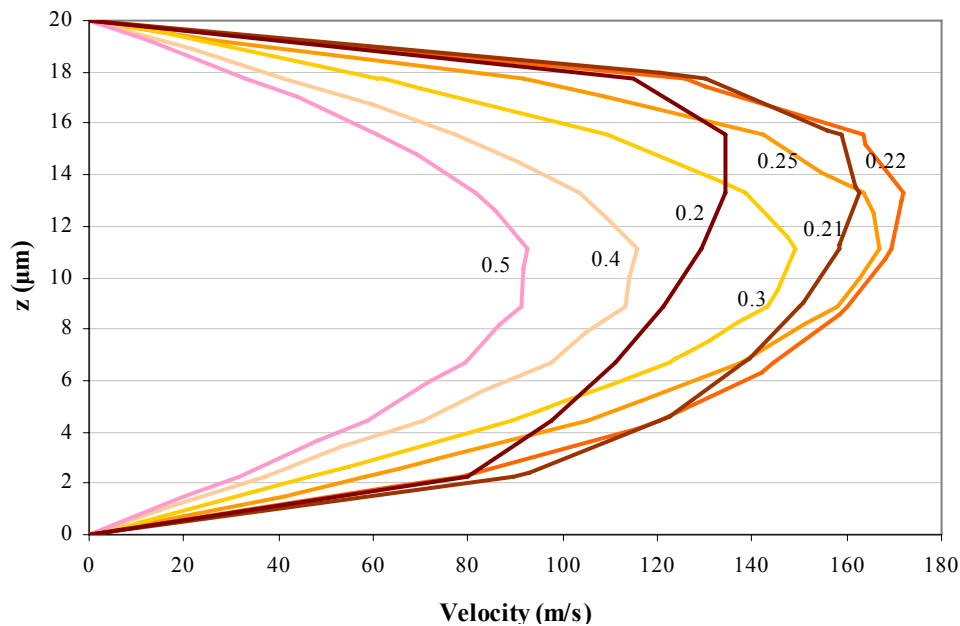


Figure 2-21: Velocity profile at different radii for fully opened valve.

In Figure 2-21 the velocity profiles are plotted for the different radii indicated in Figure 2-20. The radii are given in mm. For a fully developed flow, the velocity profile is assumed to be parabolic. One can see that the velocity profile is not parabolic in the beginning of the resistance (0.2-0.25 mm). At a radius of 0.5 mm the flow is fully developed. It means that the entrance length is $0.5 - 0.2 = 0.3$ mm. It can also be observed that the highest velocity reached at 0.22 mm and then decreases with $1/r$ (see equation 34). According to theory, it can be seen that the entrance length in the variable resistance for 20 mm gap height is 1.2 mm (see Figure 2-12). In comparison with the simulation it is 4 times higher. This deviation is due to the fact that the area in the simulation where the gas flow through increases with the radius. And the equation used for the calculating entrance length is valid when the cross sectional area is constant (see section 2.2.3).

2.5.4 Density

In theory it is assumed that the density is constant. But as the Mach number exceeds the value of 0.3 then the compressibility affects are important to predict the flow behavior. The abrupt changes in density occur as the Mach number increases. Figure 2-22 shows the density as function of radius for different gap heights. By comparing the Figure 2-18 and Figure 2-22 one can observe that they look quit similar. From this it can be concluded that the density is determined by the static pressure. The more the valve opens, the Mach number increases and the abrupt changes in the density occur. The Mach number gives an indication for the rate of change in the density.

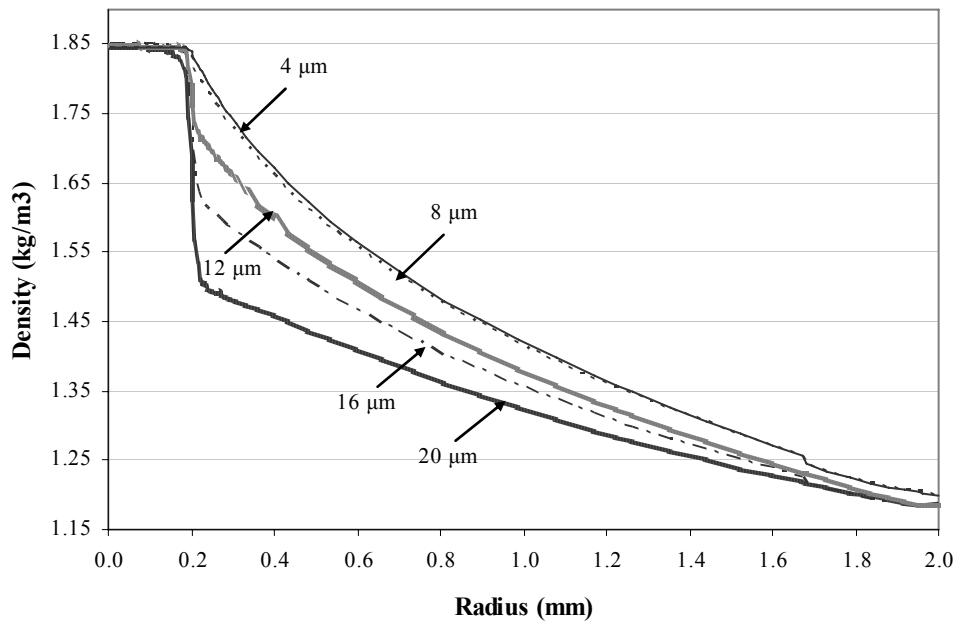


Figure 2-22: Density as a function of the radius for different gap heights.

In theory the density at the entrance of the valve can be calculated with an equation similar to the Bernoulli equation for isentropic flow of a perfect gas. For a perfect gas the density and pressure are related by

$$\frac{p}{\rho^k} = C \quad (35)$$

where k is the specific heat ratio and C is a constant.

Along a streamline the following equation is valid

$$\int \frac{dp}{\rho} + \frac{V^2}{2} + gz = \text{constant} \quad (36)$$

In equation 36 p is the pressure, ρ is the density, V is the velocity and g the gravitational constant. Substituting equation 35 in equation 36 results in equation 37.

$$C^{1/k} \int p^{-1/k} dp + \frac{V^2}{2} + gz = \text{constant} \quad (37)$$

Integrating the first term of equation 37 between 2 points along a streamline (see Figure 2-23) results in:

$$\left(\frac{k}{k-1}\right)\left(\frac{p_1}{\rho_1}\right) + \frac{V_1^2}{2} + gz_1 = \left(\frac{k}{k-1}\right)\left(\frac{p_2}{\rho_2}\right) + \frac{V_2^2}{2} + gz_2 \quad (38)$$

The parameters V_1, p_1, ρ_1 and V_2, p_2, ρ_2 are taken at the entrance of the resistance and at the exit of the resistance, respectively (see Figure 2-23).

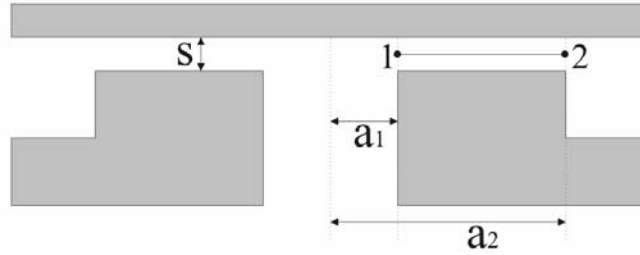


Figure 2-23: Streamlines between points 1 and 2.

In this case the body force terms can be neglected. The density at the entrance is then calculated by:

$$\rho_1 = \frac{\left(\frac{k}{k-1}\right)p_1}{\left(\frac{k}{k-1}\right)\left(\frac{p_2}{\rho_2}\right) + \frac{1}{2}(V_2^2 - V_1^2)} \quad (39)$$

The velocities V_1 and V_2 can be calculated by:

$$V_{1,2} = \frac{1}{12} \frac{(p_2 - p_1) \cdot s^2}{\mu \cdot \ln\left(\frac{a_2}{a_1}\right) a} \quad (40)$$

In equation 40 a is a_1 for the velocity at point 1 (V_1) and a is a_2 for the velocity at point 2 (V_2). In table 8 the required values to calculate the velocities and the density at the inlet. Table 2-14 shows the calculated velocities and the calculated density at the inlet for different gap heights. As one can see from Table 2-14 the density at the inlet is not depending on the gap height. This is in agreement with the simulation as can be seen from Figure 2-22.

Table 2-13: Parameters used to calculate density at the entrance.

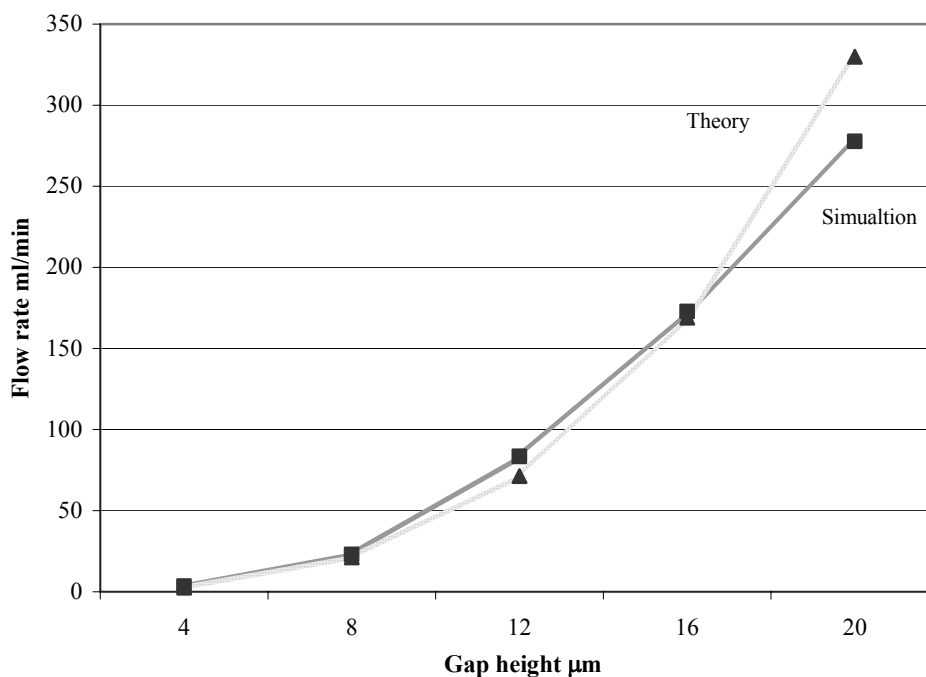
k	ρ_2 (kg/m ³)	p_1 (Pa)	p_2 (Pa)	a_1 (mm)	a_2 (mm)
1.4	1.19	$1.5 \cdot 10^5$	$1.0 \cdot 10^5$	0.2	2

Table 2-14: Velocities and entrance density for different gap heights.

s (μm)	V_1 (m/s)	V_2 (m/s)	ρ_1 (kg/m^3)
20	217.7	21.9	1.844
16	140.0	14.0	1.844
12	78.5	7.87	1.845
8	35.0	3.5	1.845
4	8.8	0.9	1.845

2.5.5 Volume flow

In this section, the flow rate of the theoretical model is compared with the simulated results. The simulation software calculates the mass flow through the valve. The mass flow at the inlet is the same as at the outlet. The volume flow however is depending on the density. It is obvious from the simulation results that the density at the inlet is higher than at the outlet. In the theoretical model it is assumed that the density is constant. The volume flow is calculated at a temperature of 20°C. The density of air at this temperature is 1.204 kg/m³.

**Figure 2-24:** Volume flow as a function of gap height.

The volume flow is calculated at a temperature of 20 °C. the density of the air at this temperature is 1.204 kg/m³. The volume flow can be calculated by:

$$\varphi_v = \frac{60000\varphi_m}{\rho} \quad (41)$$

In Equation 41 φ_m is the mass flow calculated by the simulation software and ρ is the density of air at 20°C. The calculated volume flow is plotted as a function of the gap height (see Figure 2-24). Table 2-15 shows the comparison of calculated and simulated values.

Table 2-15: Volume flow.

s (μm)	Simulation [ml/min]	Calculated [ml/min]	Deviation %
4	3.40	2.64	22.43
8	22.92	21.11	7.91
12	83.37	71.25	14.53
16	172.76	168.88	2.24
20	277.77	329.85	-18.75

By comparing the simulated and calculated volume flow values, one can observe the following:

- Simulation predicts higher flow for smaller gap height which suggests the low resistance as compared to the flow model.
- For a fully opened valve, simulation volume flow is smaller which suggests higher resistance due to rapid density changes.

From the simulation one can see that the gas flow is mostly determined by the variable resistance and not by the chamber around it. This is as expected because the resistance in between the membrane and the valve seat is much higher than the resistance of the chamber. The density difference between the inlet and outlet is calculated. It is observed that density changes rapidly when the Mach-number exceeds 0.3. A rapid density change results in a lower volume flow through the valve when compared with the theory.

2.6 Conclusions

Summing up all the results it can be concluded from the modeling that a single valve which can operate in all the 3 different operational modes can not be made within a single design (see Table 2-5). In order to achieve this, the static resistance needs to be adjustable within the range of $1 \cdot 10^8$ till $3 \cdot 10^{12}$ Ns/m⁵. This is a very large range. Additionally the orifice radius a_1 of the variable resistance also needs to be changeable in the range of 50μm to 1mm. It seems to be very difficult to integrate all three operational modes in one design. For every mode, Mach number, Reynolds number and the entrance lengths are considered. The theoretical model is accurate when Mach number is less than 0.3, flow is laminar and entrance length is smaller than channel length. It seems to be impossible to define the single valve configuration which can accommodate all operational modes within these boundaries.

It can also be concluded that the smallest stepper motor AMD0620 in combination with a gear box of 120:0 can provide the enough torque to deflect the membrane to control the flow. Additionally, the controllability of 1-2% of full scale flow can be achieved with a fast response time of less than 20 ms.

In order to see how the compressibility affects the flow behavior, a valve with typical dimensions is fabricated and characterized.

Chapter 3

3 Stepper Motor Actuated Microvalve

Abstract

In this chapter fabrication and the characterization of the stepper motor actuated microvalve is presented. The physical nature of the fabrication process is provided in detail. Experimental results are compared with the theory. It is demonstrated that the new technique of fine and micromachining is not only simpler but it also provides the results as expected.

3.1 Introduction

Based on the modeling details presented in the chapter 2, design, fabrication and characterization of the stepper motor actuated microvalve is described in this chapter. All the aforementioned factors have been considered and the valve with ‘Typical’ operational mode has been chosen to realize and characterize.

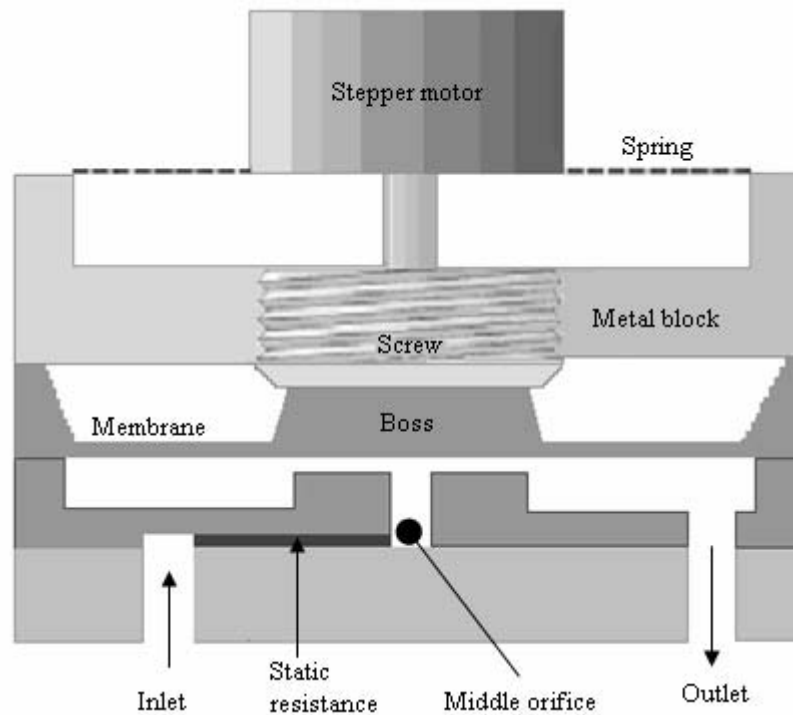


Figure 3-1: A schematic cross sectional view of microvalve with variable and static resistance in series.

The schematic cross sectional view of the valve is shown in Figure 3-1. The core components of the microvalve are divided into two parts: Fine machined and Micro machined respectively. The first part, which is fine machined, comprises of a metal block along with a screw, which is rotated by the micro stepper-motor mounted on a spring (see Figure 3-2). The screw mechanism is used to convert the rotary motion of the stepper-motor into translational motion in order to deflect the silicon membrane. The combination of stepper with screw provides the benevolent feature of controlling the flow at any intermediate state without continuous power consumption. Upon actuation, stepper motor rotates the metal screw which deflects the membrane to control the flow without actuation. The screw position remains unchanged due to the friction between the threads, which keeps the membrane in deflected state even when stepper motor is switched off. This mechanism keeps the valve in operation at any state without the need of continuous power supply.

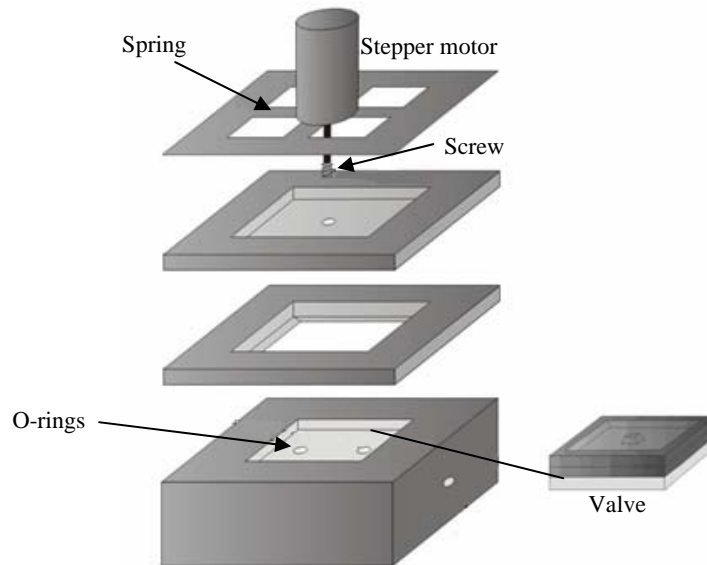


Figure 3-2: Fine machined part: Stepper motor mounted on a spring, metal block and metal screw.

The second part is the micro machined valve made from three wafers (see Figure 3-3). The Pyrex wafer has the inlet and the outlet orifices (see Figure 3-3 c). The middle wafer is from silicon which carries the valve-seat that acts as variable resistance and also contains a rectangular channel at its bottom, which acts as a static resistance. The inlet in the Pyrex wafer opens in this rectangular channel which is connected to the valve seat by the middle orifice (see Figure 3-3 b, e). The top wafer is also from silicon having a square membrane, which controls the gas flow upon deflection (see Figure 3-3 a). To prevent the membrane from breakage, a square boss is introduced on the top of the membrane. The boss makes the membrane less vulnerable for the mechanical contact between silicon membrane and metal screw.

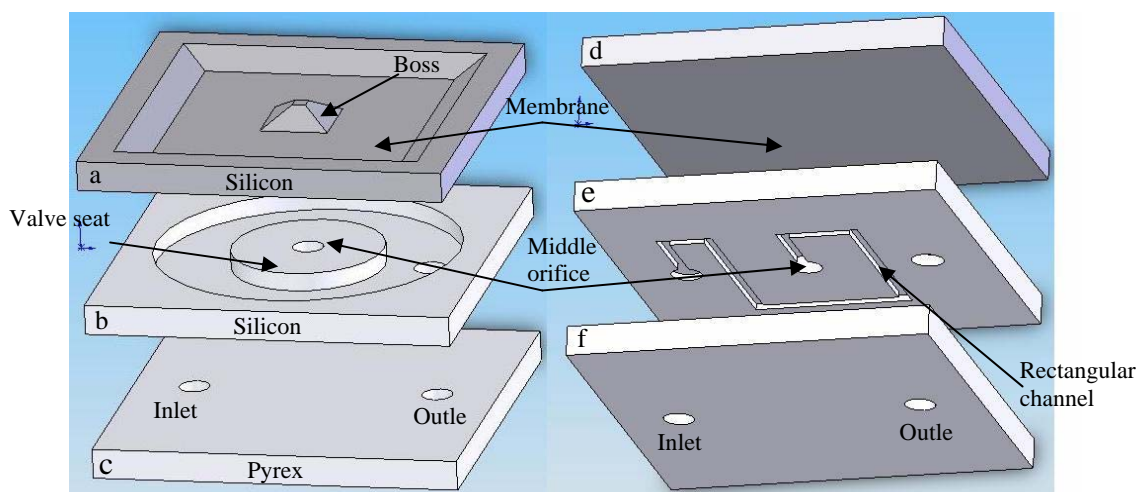
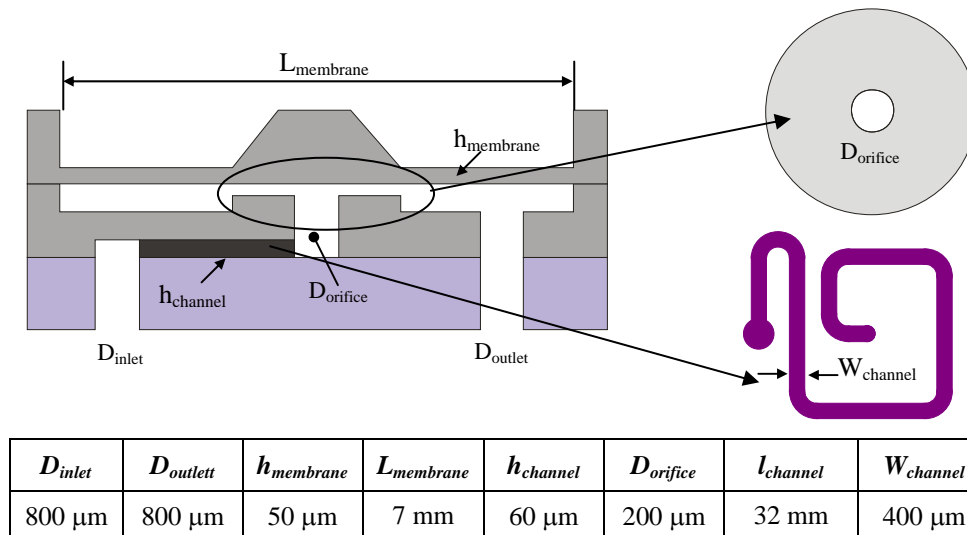


Figure 3-3: Three dimensional view of microvalve with variable and static resistance in series with each other.

The specifications used to fabricate the valve with ‘Typical’ mode are given in the Table 3-1.

Table 3-1: Valve specifications for “Typical” operational mode.



3.2 Fabrication

The fabrication process of the valve is straightforward as it includes standard micro-machining steps. It includes the micro machining of three wafers as shown in Figure 3-3. The fabrication is started with silicon membranes. They are fabricated primarily by the deposition, patterning and KOH etching. A 150 nm thick high stress stoichiometric silicon nitride (Si_3N_4) layer is deposited on Silicon <100> wafer by the Low Pressure Chemical Vapor Deposition (LPCVD). The high stress silicon nitride layer is preferred over silicon rich nitride (SiRN) as it leaves the silicon surface smoother than SiRN upon its removal. The silicon nitride is patterned from the topside of the wafer by the Reactive Ion Etching (RIE) defining the membrane and the boss. Then KOH etching (with a time stop) is used to etch the silicon wafer till the required membrane thickness of 50 μm is reached. Finally the nitride is removed by 50% HF to get the membrane with the boss as shown in Figure 3-4.

To realize the channel, the variable resistance and the orifices, a double-sided polished Silicon <100> substrate is used. As a first step, photo resist (908/35) as a mask layer, is patterned on the backside of the substrate. Using the photo resist as a mask layer, 60 μm rectangular channels are etched using the BOSCH process for 15 minutes (see Figure 3-5). For complete process scheme see Appendix B.

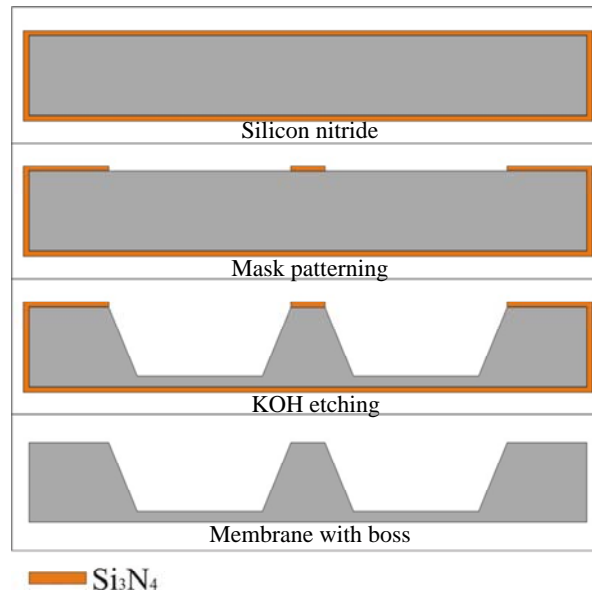


Figure 3-4: Fabrication of square silicon membrane with KOH time stop etching.

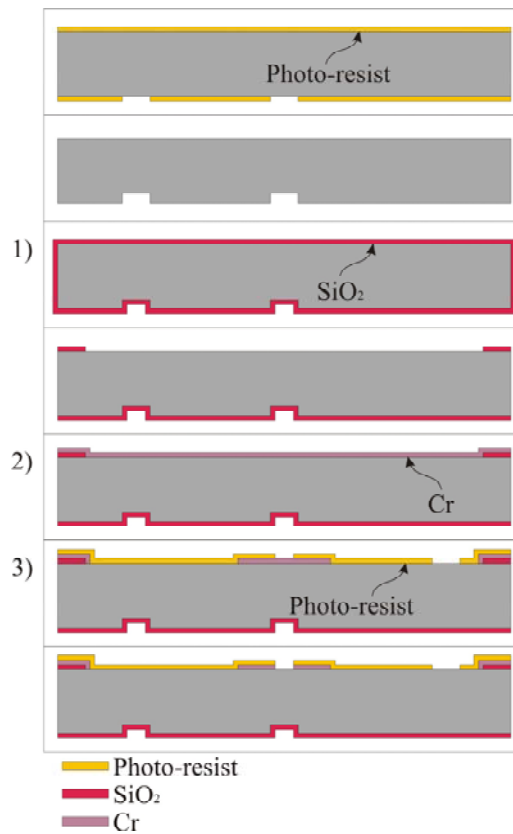


Figure 3-5: Process flow for the fabrication of the middle wafer containing channels, variable resistance and orifice.

To fabricate the variable resistance and the orifice, three different layers are realized on the topside of the substrate. 1) A 1.2 μm layer of SiO_2 is grown by wet oxidation of silicon at 1150 $^\circ\text{C}$. The SiO_2 layer is patterned which defines the square chamber around the valve seat. With this step the height between the valve seat and the membrane is defined. A 50 nm layer of chromium is deposited using a sputtering process (90 sccm Ar. flow, 5.0 E-3mbar, 200W). The chromium layer is patterned which defines the shape of the valve seat in the second etching step. Finally a layer of photo-resist (907-17) is patterned. This mask layer defines the orifice and outlet of the valve (see Figure 3-5).

Then the three etching steps are followed to realize the variable resistance, the chamber and the orifice with the BOSCH process. First, the Bosch etching process is optimized to give the best uniformity over the whole wafer. A drawback for the optimization is that the walls are less straight which is not critical for this application (see Appendix C). The following parameters are used for the BOSCH process: Temperature: 10 $^\circ\text{C}$, C_4F_8 (2 sec, 10 sccm, valve 100 %), SF_6 (13 sec, 400 sccm, valve 15 %), ICP: 2500 W, CCP: 10 W, SH: 110 mm, He: 0.7 sccm.

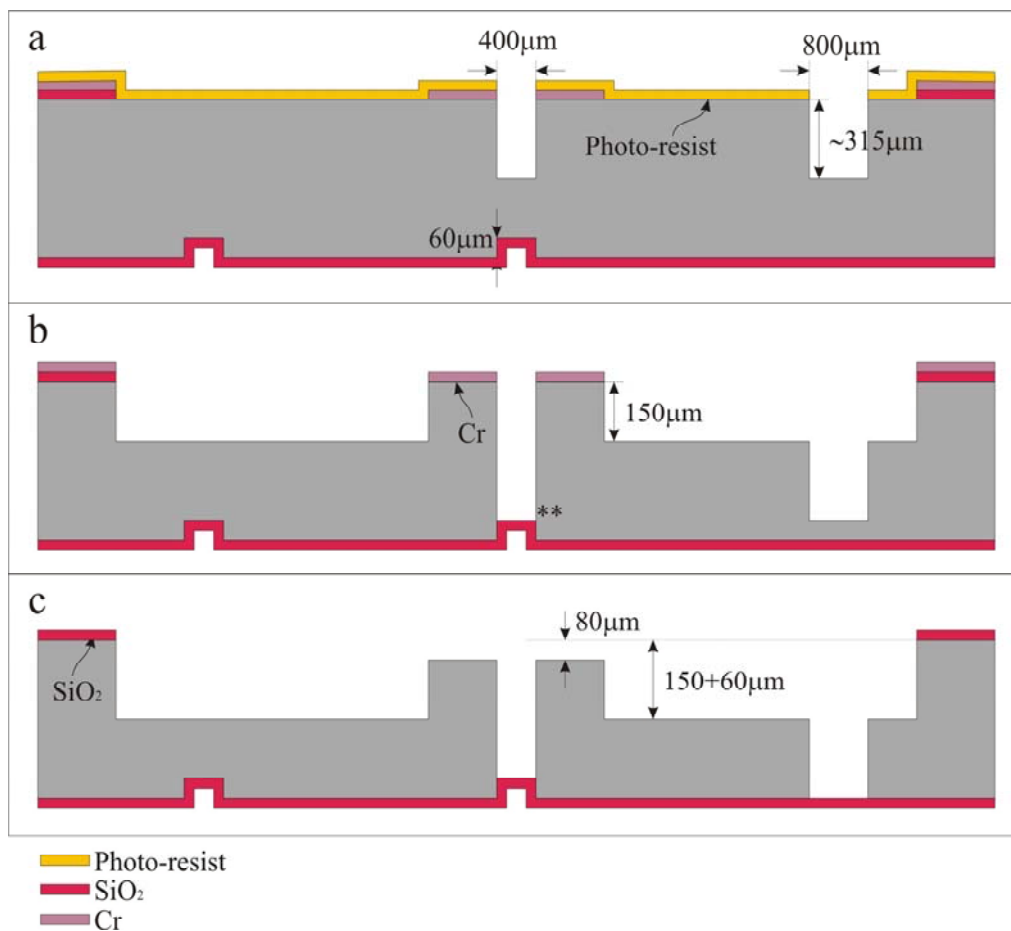


Figure 3-6: Process flow for etching through the wafer.

Figure 3-6 shows the etching steps in detail. Within three etching steps the orifice and the outlet have to be etched through the wafer. In the last step the valve seat is etched and it is critical that the depth is not more than 80 μm . In the first two steps it is important that the holes are etched far enough for the last step. Over-etching is needed to get a well defined hole at the bottom of the wafer. The thickness of the wafer is 525 μm . After the first two steps the depth of the holes needs to be at least 465 μm , leaving 60 μm silicon plus 20 μm over-etching for the last step. The first etching step (16 minutes) has a depth of 315 μm (Figure 3-6 a). After this step the photo-resist is removed by HNO_3 . In the second step (10 minutes) another 150 μm is etched (see Figure 3-6 b). The Cr layer is removed leaving the SiO_2 mask layer for the last etching step of 6 minutes (see Figure 3-6 c). To keep the temperature constant during the etching process, the wafer is cooled from the backside by helium. A procedure has been developed to avoid leakage of cooling gas while etching through the wafer. This procedure can be found in Appendix D. Finally, the SiO_2 layer is removed using HF (50%). It is difficult to etch different size holes on one wafer because a small hole etches slower than a larger hole. The process is optimized for an orifice with the diameter of 400 μm . In order to realize the orifices with different size on a single wafer, process should be optimized.

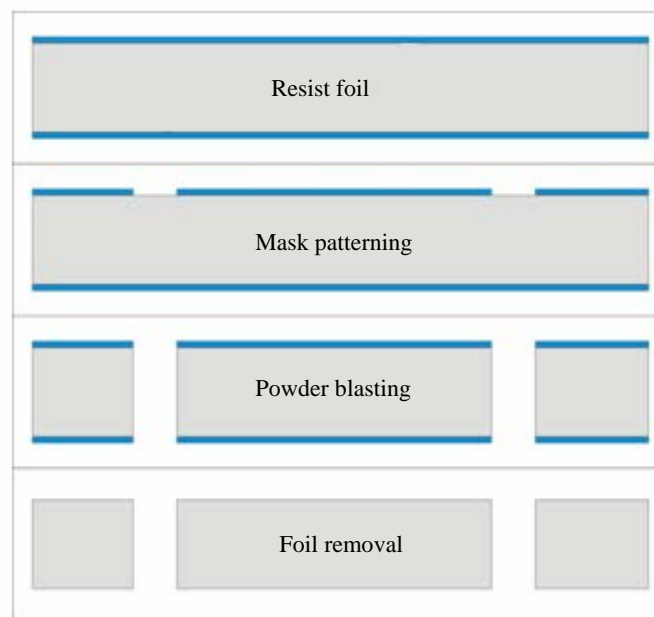


Figure 3-7: Flow process for the fabrication of inlet and outlet in the Pyrex wafer.

The fabrication process to realize the inlet and the outlet in Pyrex wafer is shown in Figure 3-7. Both sides of the Pyrex wafer are covered with B 410 foil. The foil on the top side of the wafer is patterned to define the inlet and the outlet of the valve. The inlet and the outlet are realized in the Pyrex wafer by a powder blasting process (particles 32 μm AlO_2) as shown in Figure 3-7.

The two silicon wafers are fusion bonded at 1100 $^{\circ}\text{C}$ in the N_2 atmosphere (see Figure 3-8 c). An Electronic Visions Aligner is used to align and to pre bond the wafers. The final

step is to anodic bond the fusion bonded silicon wafers and Pyrex wafer (see Figure 3-8 e). The anodic bonding is performed on a hot plate setup.

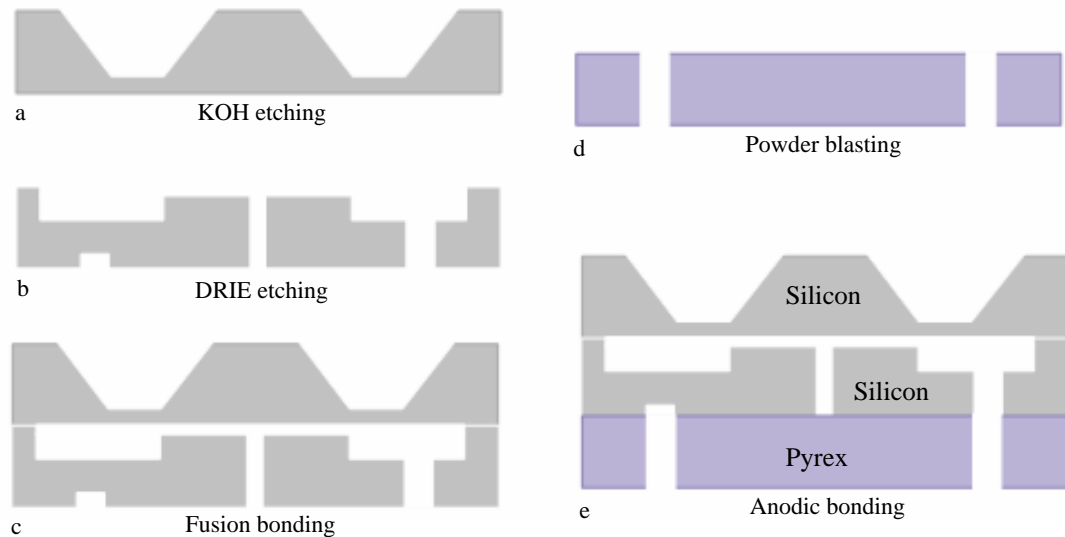


Figure 3-8: Process flow for fusion and anodic bonding.

Finally the wafers are diced from topside. Dicing foil is applied on the backside of the stack of three wafers to protect the inlet and the outlet from the particle contamination.

We could not optimize the etching process for the different sizes of static resistances and valve openings which results in devices not having required static resistance ($w = 800 \mu\text{m}$, $h = 60 \mu\text{m}$ and $l = 32 \text{ mm}$) with valve opening size of $100 \mu\text{m}$.

3.3 Characterization

In this section the characterization of the valve comprising of fine and micromachined part is described. The volume flow through the valve is measured as a function of gap height and the performance of the stepper motor is analyzed.

3.3.1 Experimental setup

A schematic of the measurement setup is shown in Figure 3-9. A flow meter of Bronkhorst is used to measure the gas flow. The maximum volumetric flow for the flow meter that has been used is 220 ml/min as it is calibrated to this value. The precision of the flow meter is 1% of the maximum flow. In front of the flow meter an air filter is placed to purify air from dust particles, to avoid congestion of the valve. The pressure is measured by the pressure gauge in between the flow meter and the valve.

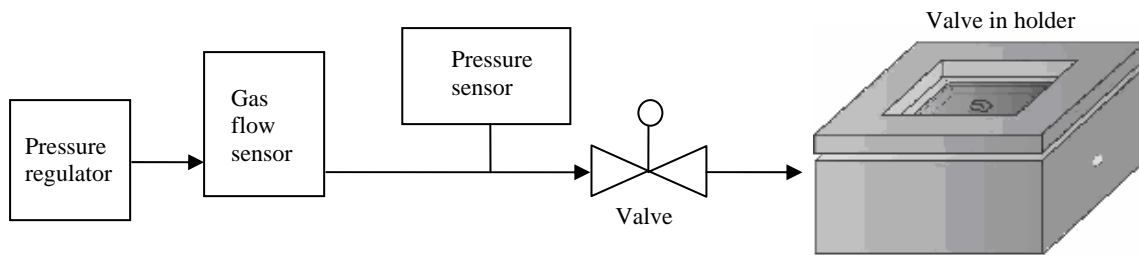


Figure 3-9: Experimental setup.

3.3.2 Volume flow rate measurements

The flow rate is measured as a function of gap height at a pressure difference of 4 bar. The measurement procedure starts with applying the pressure and closing the valve till a volumetric flow of 2 ml/min is reached. Then the valve is gradually opened up to a gap height of 24 μm and the flow rate is measured. The step size is set to approximately 1 μm . The volume flow rate is measured with four different pressure differences of 1, 2, 3 and 4 bar between inlet and outlet. Valves with five different lengths of the static resistance (8, 12, 16, 20 and 24 mm) were characterized. Figure 3-10 shows the measured volumetric flow rates at a pressure difference of 4 bar for a valve with static resistance of 24 mm in length.

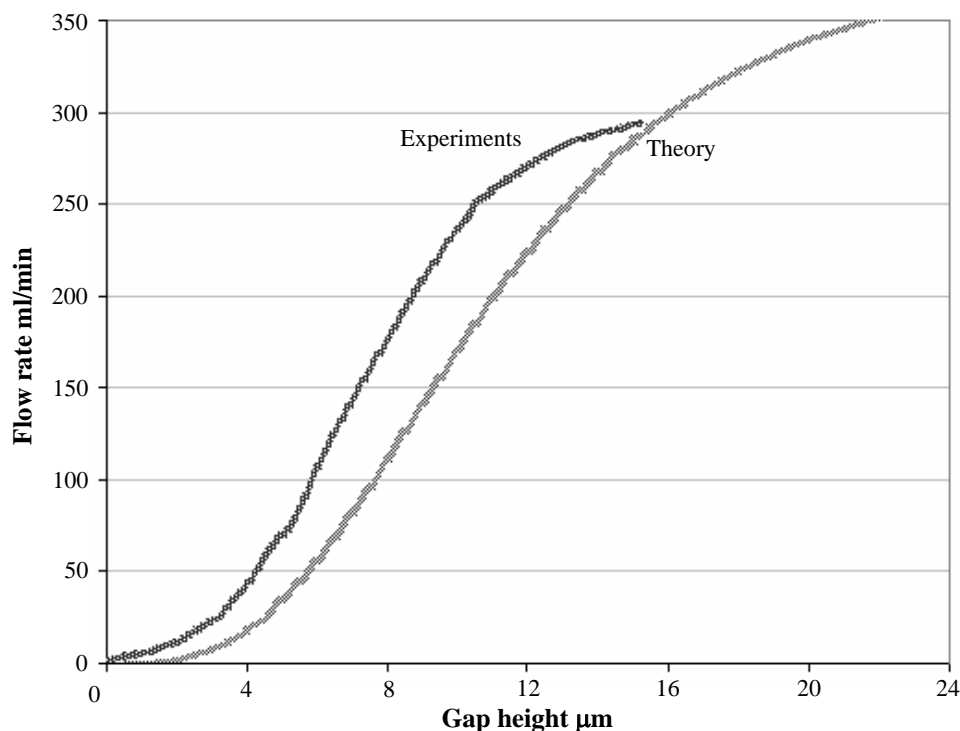


Figure 3-10: Measured volume flow rate as a function of gap height.

It can be seen that the volume flow exceeds the value of 200 ml/min at a gap height of 9 μm instead of 22 μm (see Figure 3-10). It is due to the small static resistance because the valves with higher static resistance were not properly etched (see section 3.2).

It can also be observed that the measured flow rate curve is steeper than the theoretical curve. It is due to the smaller variable resistance offered by the under sized membrane boss (see section 3.2). Due to the under sized boss (see Figure 3-11), the membrane does not stay parallel with the valve seat and offers less resistance which results in the steeper change in the volume flow. In order to make better approximation, the resistance is split into two resistances as shown in Figure 3-12.

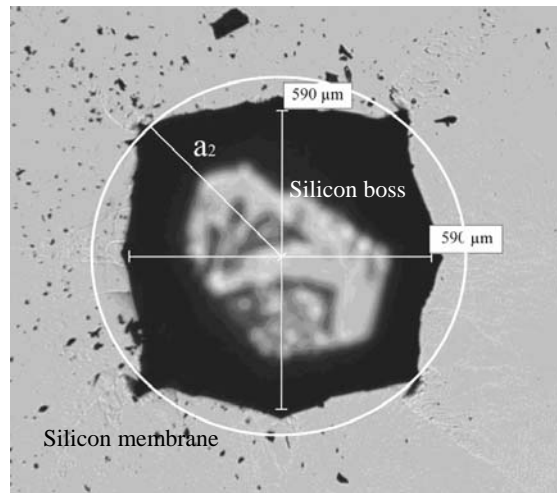


Figure 3-11: An undersized boss on silicon membrane.

The first resistance is calculated by:

$$R_{v1} = \frac{6\mu \ln\left(\frac{a_2}{a_1}\right)}{\pi s^3} \quad (42)$$

For the second resistance it is assumed that the gap height increases linearly with the radius:

$$s(r) = Ar + B \quad (43)$$

By applying the boundary conditions, $s(a_2) = s$ and $s(a_4) = s_4$, equation 43 becomes:

$$s(r) = \frac{(s - s_4)(r - a_4)}{(a_2 - a_4)} \quad (44)$$

The second resistance is then calculated by integrating the resistance per unit length over the radius:

$$R_{v2} = \int_{a_2}^{a_3} \frac{6\mu}{\pi s^3(r)} dr \quad (45)$$

The volume flow is then given by:

$$\phi_v = \frac{60000\Delta P}{R_{v1} + R_{v2} + R_s} \quad (46)$$

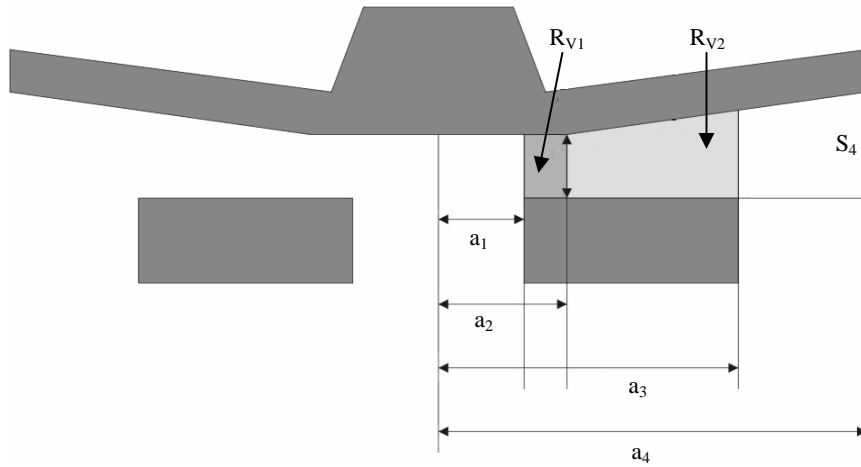


Figure 3-12: Approximated resistance with the undersized boss.

Table 3-2: Variables to calculate volume flow with approximated resistance.

a_1 (mm)	a_2 (mm)	a_3 (mm)	a_4 (mm)	R_s (Pas/m ³)	s_4 (μm)
0.2	0.42	2	3.5	7 E10	80

The dimensions to calculate the volume flow rate are given in Table 3-2. The value of s_4 is determined by the last etching step of the fabrication. The value of a_2 is determined by the size of the boss realized by KOH etching. The side length of the boss (d) is approximately 590 μm (see Figure 3-11). The equivalent radius is then calculated by:

$$a_2 = \frac{1}{2} \sqrt{2d^2} \quad (47)$$

The volume flow rate is calculated and plotted as a function of gap height (see Figure 3-13). It can be seen that the corrected theoretical curve almost coincides with the experimental curve. So it can be said that the results predicted by the incompressible gas flow model are in good agreement with the measurements.

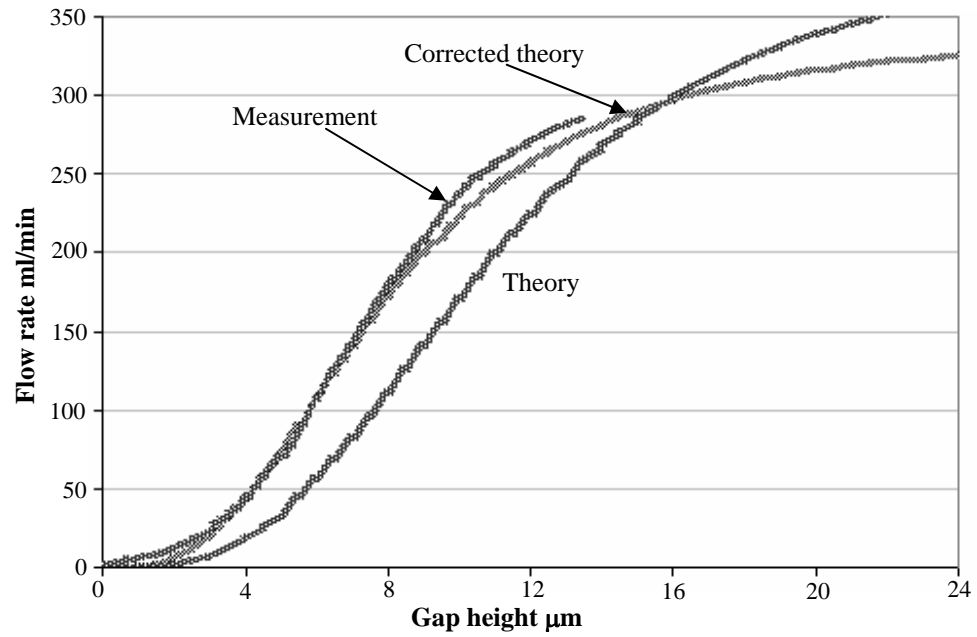


Figure 3-13: Experimental and theoretical curves of volume flow rate as a function of gap height.

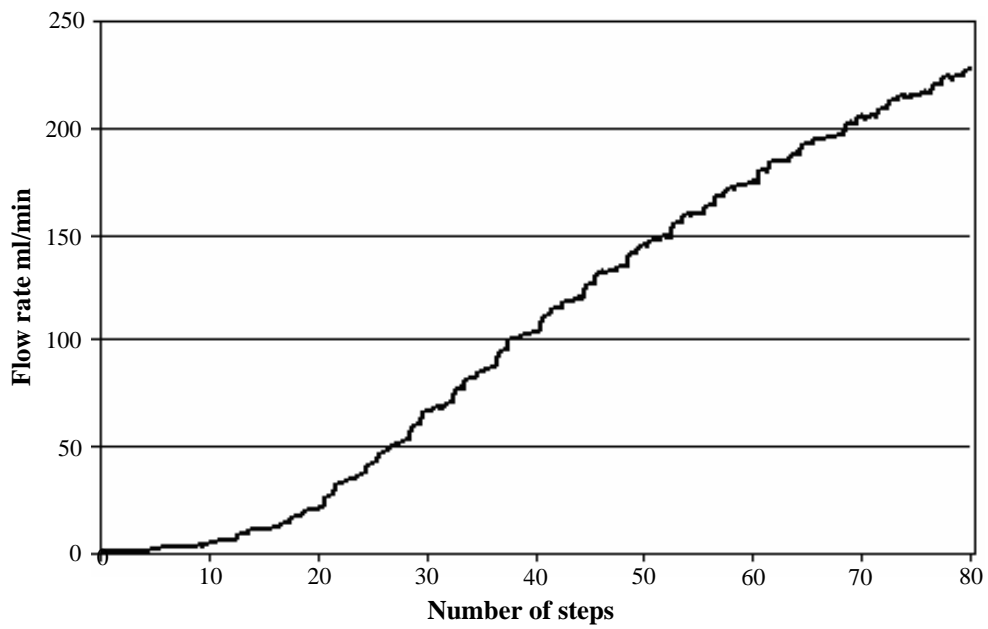


Figure 3-14: Flow characteristic curve to examine stepper motor performance.

3.3.3 Stepper motor performance

The performance of the stepper motor has also been examined. To observe the hysteresis effect in gearbox, two different motors ADM0620 and ADM0820 with respective gear reduction ratios of 256:1 and 120:1 (zero backlash) were used.

A pressure difference of 4 bar is applied between the inlet and the outlet of the valve. The valve is steadily closed till the volume flow reached to 0.6 ml/min. Then the valve is gradually opened by the stepper motor till the flow reaches 220 ml/min. A time delay of 10 sec is used to observe the difference in flow per step. Figure 3-14 shows the volumetric flow rate as a function of number of steps for the stepper motor “ADM0820” with a gear reduction ratio of 120:1. It can be observed from the plot that the volumetric flow rate of 220 ml/min is achieved within the 80 steps and with the equivalent gap height of 9 μm (see Figure 3-10). This corresponds to a mean step size of 112 nm, which differs from the calculated value of 83 nm. This might be caused by the friction in the screw shown in Figure 3-15. It can be observed that a couple of small steps are followed by larger steps. During small steps tension is built up due to the friction and when the force is high enough it takes larger steps to overcome the friction. This phenomenon limits the controllability to 2 to 8 ml/min per step (see Figure 3-15).

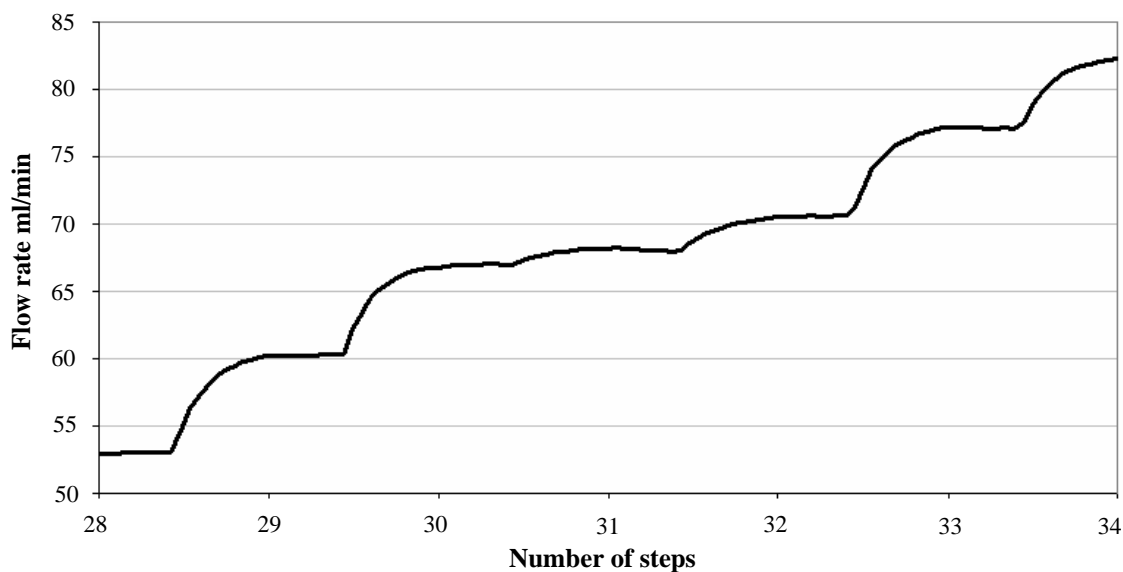


Figure 3-15: Stepper motor (AMD0820): Due to friction couples of small steps are followed by the longer steps. This phenomenon also limits the controllability to 2-8 ml/min.

In order to achieve the required controllability, another stepper motor ADM0620 with 256:1 gear reduction ratio was used. In this case, flow rate change of 0.5 to 4 ml/min per step was achieved (see Figure 3-16). It is due to the smaller mean displacement of 51 nm per step with this stepper motor.

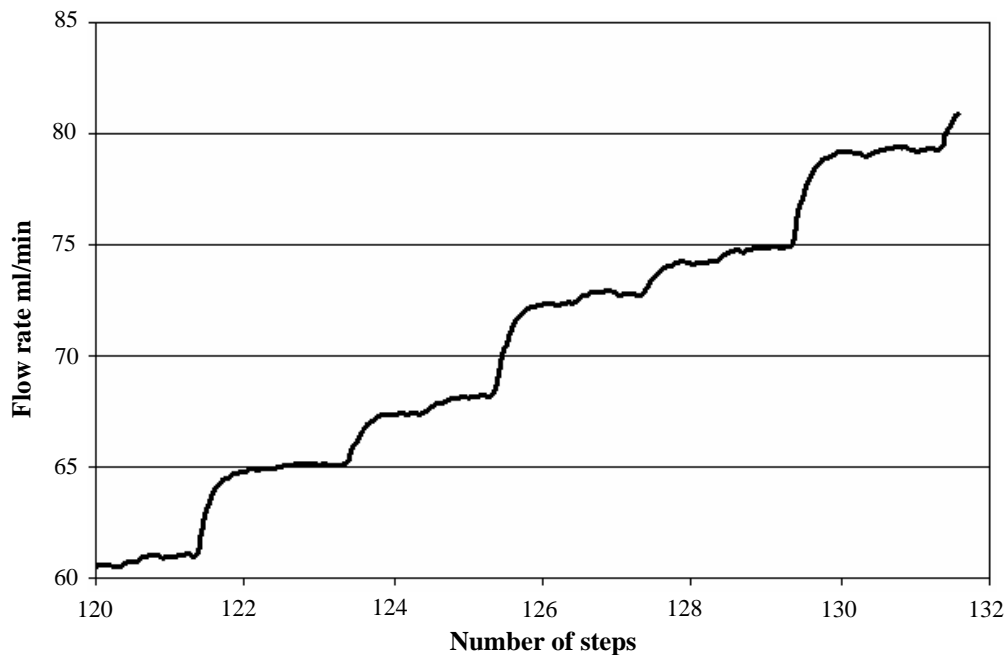


Figure 3-16: Stepper motor AMD0620 (256:1): A required controllability of 4 ml/min can be achieved.

It is also seen that in case of higher reduction ratio, we have a backlash problem, which results in hysteresis in the gearbox (see Figure 3-17). This phenomenon causes delay in changing the direction of rotation of the stepper motor. We can see that the gearbox with reduction ratios of 256:1 needs approximately 60 steps to change direction whereas the gearbox without backlash with a reduction ratio of 120:1 takes 6 steps to change the direction.

To observe the leakage, tests were performed at Bronkhorst Netherlands B. V. Extremely low leak rates of (5.1×10^{-6}) [ml/min] were detected with atmospheric pressure at the inlet and vacuum (1×10^{-9} bar) at the outlet.

Summing up the results, we did not find any deviation from the theory within the accuracy of our measurement. The good agreement of theory and experiment confirms our modeling assumption. Moreover modeling shows that it is very difficult to include more pressure regimes in this particular design as the difference in resistance is large for the pressure difference higher than 5 bar. The valve performance can be affected by several factors including wear and tear in the screw mechanism, hysteresis in the stepper motor and misalignment of the seat to the membrane. The frequent movement of the screw to deflect the membrane can cause wear which ultimately stops the valve operation. Misalignment will increase the power necessary to seal the valve for a given flow. It is difficult to optically verify the alignment after assembly as the valve is in silicon. This new design of the microvalve and its characterization presented above show promising improvement in features such as high flow rates, linearity, controllability at any stage with no power consumption.

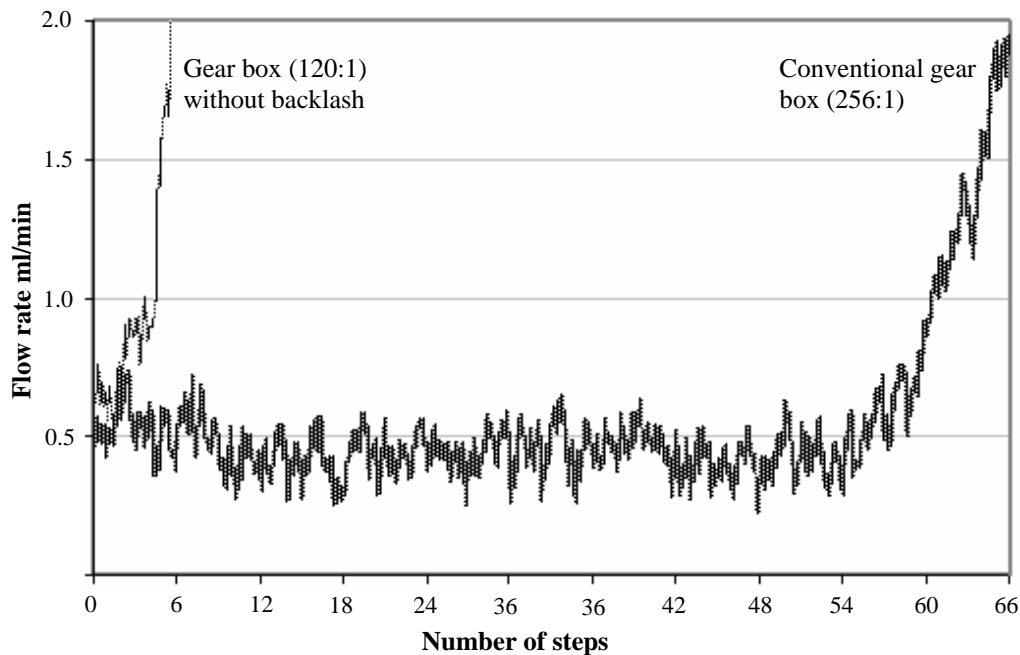


Figure 3-17: The stepper motor AMD0820 (120:1) without backlash shows less hysteresis than the stepper motor AMD0620 (256:1) with conventional gear box.

3.4 Modifications

In this paragraph, the issues described above are addressed. Three following points are considered to enhance the performance of the valve:

- To realize the boss with required size to achieve the necessary variable resistance to control the flow.
- To realize the channel serving for static series resistance with required length to obtain large controllable flow range by optimizing the etching process
- To perform the wear tests for the screw to assure the quality performance for the valve.

A new design shown in Figure 3-18 is presented to fulfill the requirements of precise controllability, larger controllable flow range and better performance of the valve. In the new design the square boss is replaced by the circular boss to achieve the required variable resistance to attain the better controllability. In the previous design it is shown (see Figure 3-13) that experimental curve was bit steeper than the theoretical. It was due to the small size membrane boss which could not provide the required resistance to control the flow (see section 3.3.2). Additionally, the channels with the required length of 32 mm along with the orifice diameter of 200 μm are realized by optimizing the uniformity over the silicon wafer during etching process.

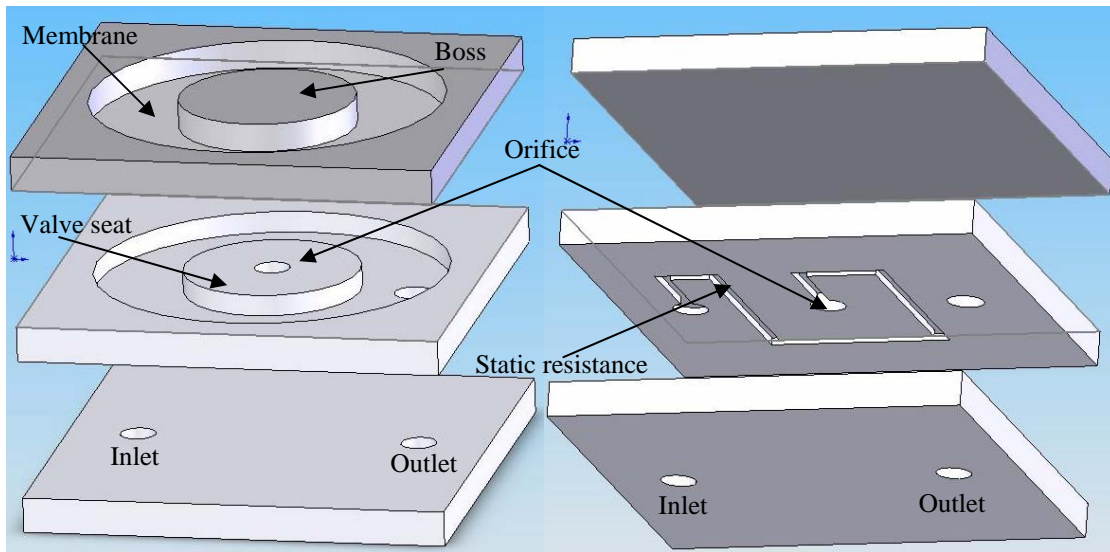


Figure 3-18: Three dimensional view of the valve: The square boss in the previous design is been replaced by the circular boss to achieve the required variable resistance.

3.4.1 Fabrication

The fabrication process for the new design is similar to that as described earlier (see section 2.2). It only includes one new step of realizing silicon membrane with circular boss with DRIE etching. They are fabricated primarily by patterning the mask layer of 908/35 photoresist. Using the photoresist as a mask layer, a 100 μm thick circular membrane with circular boss is realized using BOSCH process for 28 minutes. Finally the photoresist is removed by 100% HNO_3 to get the membrane with the boss as shown in Figure 3-18 a.

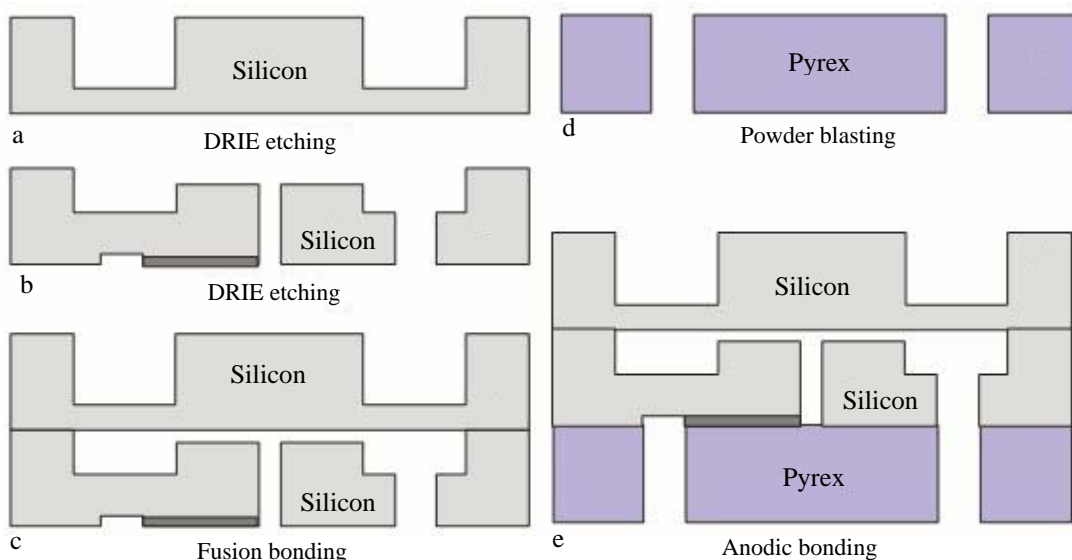


Figure 3-19: Fabrication of the microvalve with circular boss silicon membrane.

The two silicon wafers are fusion bonded at 1100 °C in N₂. An Electronic Visions Aligner is used to align and to pre bond the wafers. The final step is to anodic bond the fusion bonded silicon wafers and Pyrex wafer (see Figure 3-18 c, e). The anodic bonding is performed on a hot plate setup.

3.4.2 Characterization

The valves with circular boss of 4 mm in diameter and with required length of 32 mm for static resistance are characterized as shown in Figure 3-20. The stepper motor of ADM0620 (256:1) is used to control the flow. A pressure difference of 4 bar is applied between the inlet and the outlet of the valve. The valve is first closed till the volumetric flow reaches the value of 0.5 ml/min. Then the valve is gradually opened till it reaches its maximum flow value of 220 ml/min.

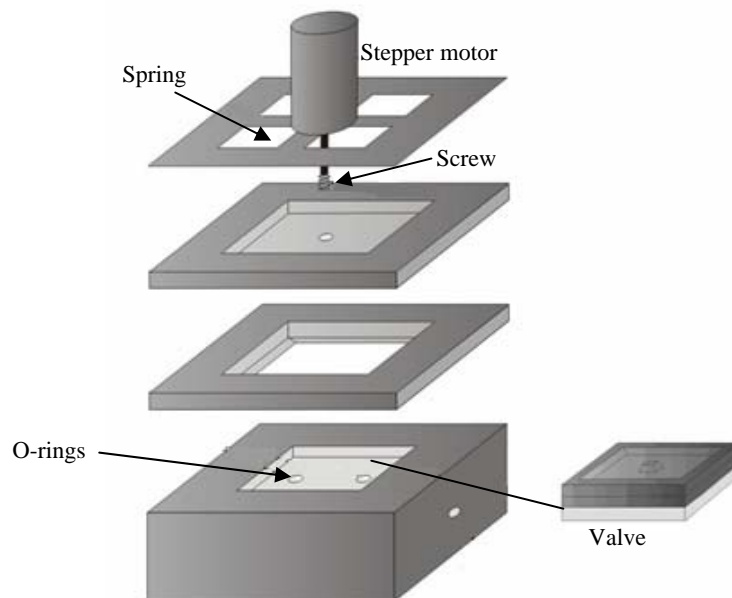


Figure 3-20: Clamping set up for the valve. It is placed on the O-rings in the metal block and then clamped with stepper motor on the top of it.

Figure 3-21 shows the volume flow as a function of gap height. The measured mean displacement per step is calculated as 75 nm. It can be seen that the experimental results are quite in accordance with the theory as the required volume flow of 250 ml/min was achieved with in the gap height of 23 μm. It shows that the realization of the channel (static resistance) with required length of 32 mm provides the expected larger controllable flow range. It can also be observed that the experimental curve is not as steep as it was in the case of under-size KOH etched boss. Because the dry etched circular boss with required size of 2 mm radius provides the necessary variable resistance to control the flow.

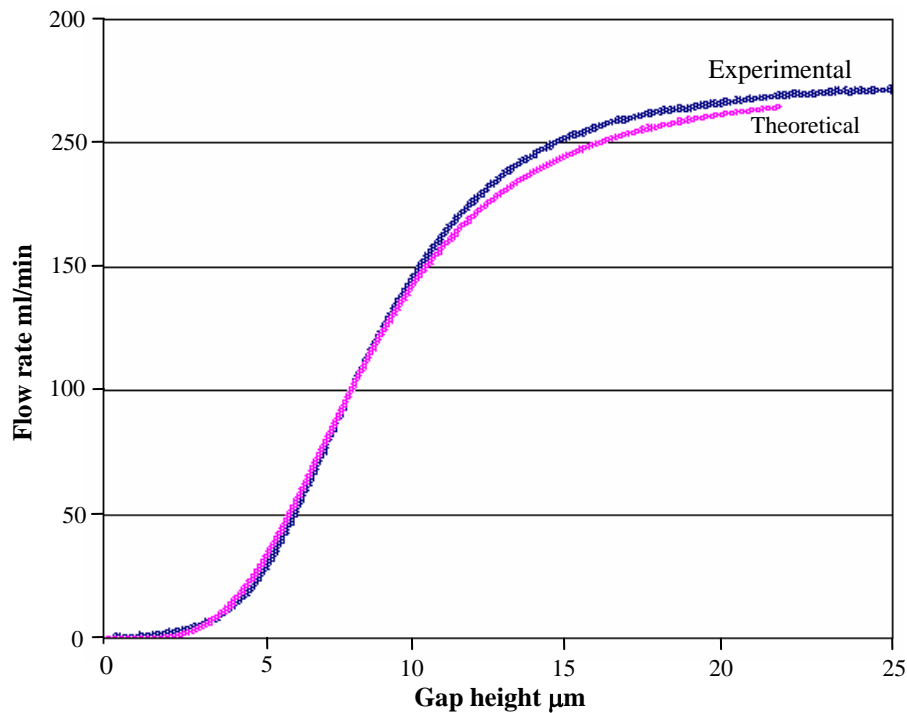


Figure 3-21: Flow rate as a function of gap height for the valve with circular boss realized by DRIE etching.

To examine the performance of the microvalve, wear tests have also been performed for different metallic screws. The typical tensile strengths of several materials are given in the Table 3-3.

Table 3-3: Typical tensile strength for different materials.

Material	Yield strength (MPa)	Ultimate strength (MPa)
Brass	180	250
Titanium alloy (6 % Al, 4 % V)	830	900
Structural steel ASTM A36	250	400
Steel high strength alloy ASTM A-514	690	760
Aluminum alloy 2014-T6	400	455

Titanium and brass screws are characterized to examine the wear during valve operation. The maximum stress on the screw threads for a closed valve with pressure difference of 4 bar is calculated. The stress is calculated for a screw with a basic diameter of 2 mm and is given in Table 3-4. It can be seen that the maximum stress on the screws is much less than their respective tensile strength value.

Table 3-4: Force and the stress on the screw [204].

$F_{Pressure} = 1.88 \text{ N}$	F_{Total} 2.48 N	Stress area for screw
$F_{Deflection} = 0.6 \text{ N}$		$A_t = \frac{\mu}{4}(D - 0.938194P)$
Stress		1.4 MPa << 180 MPa (Brass)
$\sigma = F_{total} / A_t$		1.4 MPa << 830 MPa (Titanium)

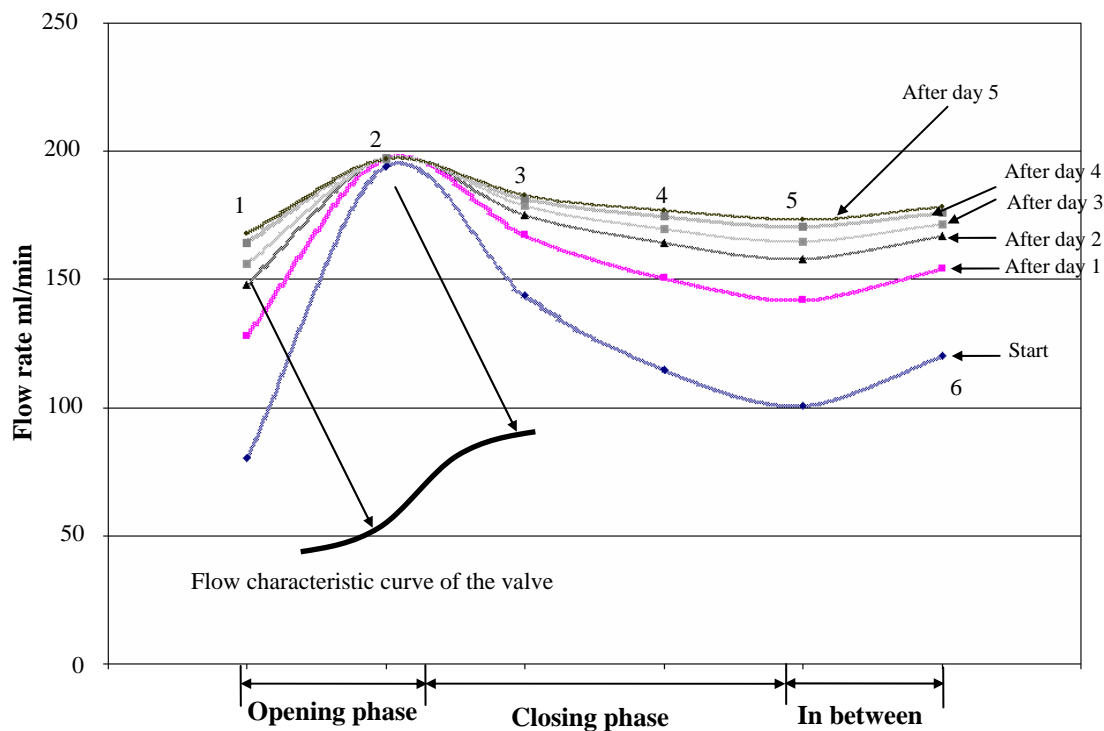


Figure 3-22: Combined effect of Hysteresis in stepper motor, change in ambient conditions and wear in screw cause high difference in flow.

In the beginning the titanium screw was used for mechanical transmission of power to deflect the membrane to control the flow. The valve with titanium screw was set to operate in cycles for 5 days at a pressure difference of 4 bar between the inlet and the outlet. It was opened, closed and kept in different intermediate states for each cycle to observe any difference in the flow rates due to wear in the screw threads. To maintain the stable flow at different states a delay of 10 seconds was provided in between each step. Figure 3-22 shows the flow characteristics curves at different phases. The flow characteristic curve shows three different phases. In the first phase, valve is opened, in the second phase valve is closed in three steps and finally it is opened to a certain value of flow. It can be observed that there is considerable difference in flow at certain points. This high difference in flow rates is likely due to the following reasons:

1-If we will closely examine the results then we can attribute this change mainly to the characteristic flow behavior of the microvalve (see Figure 3-22). Because at points 1, 3, 4, 5 and 6 a little change in gap height gives steeper change in flow as compared to the change at point 2 (see Figure 3-22).

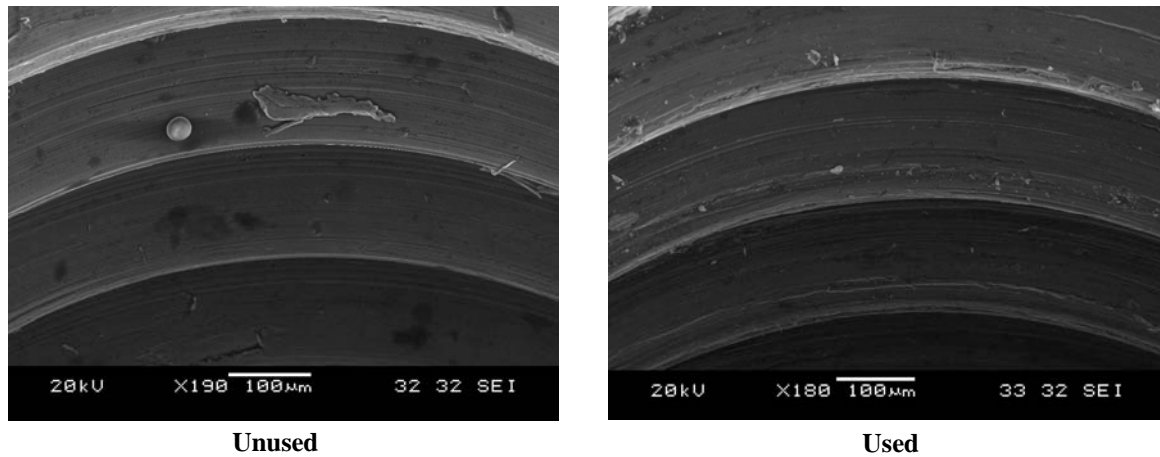


Figure 3-23: Comparison of unused and used screw threads to visualize the fact of wear.

2-It is likely due to the metal residue in between the screw threads due to metal machining during its fabrication (see Figure 3-23). In the beginning the metal residue, which is relatively big in size, cause the bigger difference in the flow. But as the time passes, the surface becomes smoother due to the removal of thin metal residue and the difference in flow becomes smaller. It can be observed from Figure 3-22 that at points 1, 3, 4 and 5, the difference in flow becomes smaller at the end. This small difference in flow corresponds to litter wear in the screw.

3-The hysteresis in the stepper motor and change in ambient conditions affect the flow behavior. The wear in the screw threads is also shown in Figure 3-23 which does not seem to be the dominant factor.

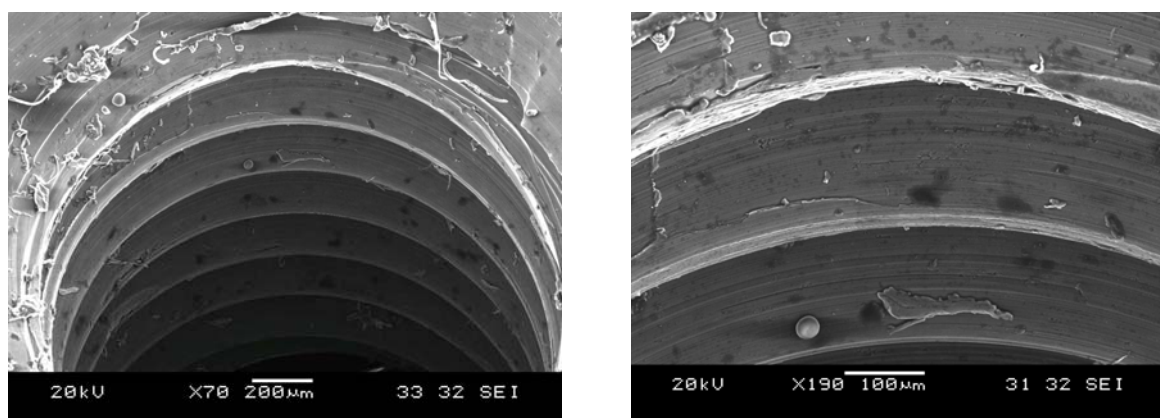


Figure 3-24: Metal residue inside the screw threads during their fabrication due to metal machining.

The silicon membrane boss and the titanium screw tip were examined to see any damage. It was observed that both the membrane boss and the screw tip were not damaged. Further experiments were also performed with the screw made of brass. Similar behavior in flow was observed. Surfaces of both membrane boss and screw tip was examined. It can be seen clearly that the tip of the brass screw was damaged (see Figure 3-25).

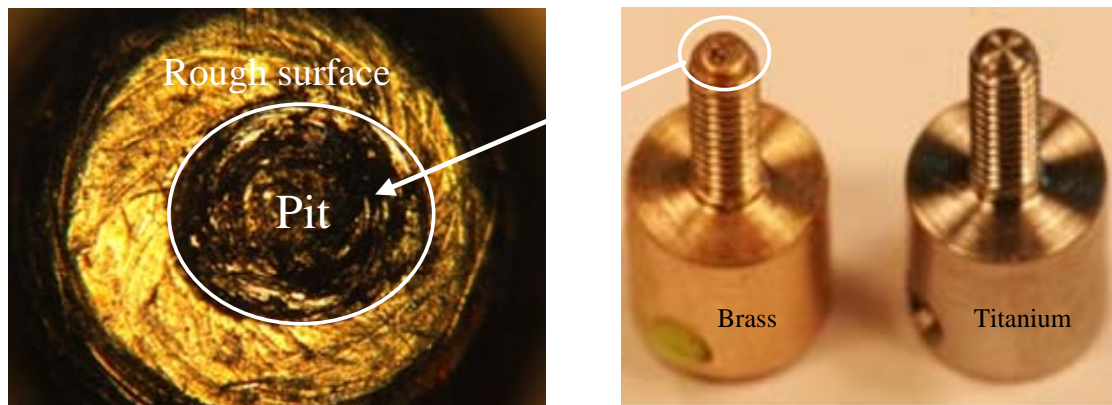


Figure 3-25: Brass screw was damaged as it is softer material than silicon.

The flat surface of the screw became extremely rough and a part of it is eroded. It happened due to the friction between the silicon boss and the bottom of the brass screw. Due to the continuous rotary movement of the screw on the top of the silicon membrane boss, friction increases and makes the screw surface rougher which ultimately eroded the bottom part of the screw (see Figure 3-25). Silicon membrane was undamaged as it is harder material than the brass (see Table 3-3).

3.5 Conclusions

A new technique has been presented to design and develop the microvalve, using the combination of fine and micromachining. This technique enables us to control high flow rates at higher pressure. This new idea of mechanical transmission (conversion of rotational motion into the translation motion using stepper motor) not only allows us to control the valve at any intermediate state but also the valve does not need any power to keep its state. Additionally, this design prevents the interaction of the process gas with the actuation part, which enhances its robustness. A hard seating configuration, using fine and micro machining combination, contributes to the enhanced leak tight microvalve operation. Extremely low leak rates of 5×10^{-6} [ml/min] were detected with atmospheric pressure at the inlet and vacuum (1×10^{-9} bar) at the outlet. Another promising feature is that it uses simple and straightforward fine and micromachining process to realize the microvalve.

The microvalve characterization for its robustness against its repeatability and its aging has been performed. The results assure that the continuous operation of the microvalve can be guaranteed by selecting the right combination of metal for screws and the bolts for the mechanical transmission

There are certain issues for the future study. First is to work on the actuation mechanism for the following reasons:

- The controllability is limited by the friction in the screw threads as the pressure is impinging on membrane. To overcome this friction, stepper motor has to take longer steps than required which affects the controllability.
- The combination of stepper motor of one gear reduction ratio and screw with certain dimensions, limits its use for different applications.
- Similarly the stepper motor with one gear reduction ratio also restricts the controllability hence affects the performance of the valve.
- Hysteresis in the stepper motor causes delay in changing the direction of the stepper motor.

Finally, the geometrical design will be optimized to accommodate more pressure ranges in a single design.

Chapter 4

4 Piezoelectric Actuated Microvalve

Abstract

Stepper motor actuated microvalve based on fine and micromachining techniques exhibit many interesting features such as high flow rates, leak tightness, controlled flow, process gas isolation, no power consumption and fast response but its practical use is limited by hysteresis exhibits by the stepper motor and the wear and tear phenomenon in the screw. In this chapter an approach is introduced to offer the permanent functioning of the valve. The use of the piezoelectric actuator instead of stepper motor provides the continuous operation of the valve with almost no hysteresis and zero backlash behavior.

4.1 Introduction

In this chapter a new design based on piezoelectric actuation is introduced. This new design is an improvement over the stepper motor actuated microvalve. The choice of the piezoelectric actuator made it possible to overcome the following problems/limitations:

- Getting rid of the unnecessary long steps to improve the flow controllability. In the stepper motor actuated microvalve during valve operation the long steps are followed by the smaller steps due to the friction in between the screw threads which limits the controllability (see Figure 3-15).
- Overcoming the hysteresis, exhibited by the stepper motor actuated microvalve.
- Avoid the back lash problem which causes slow response upon switching.

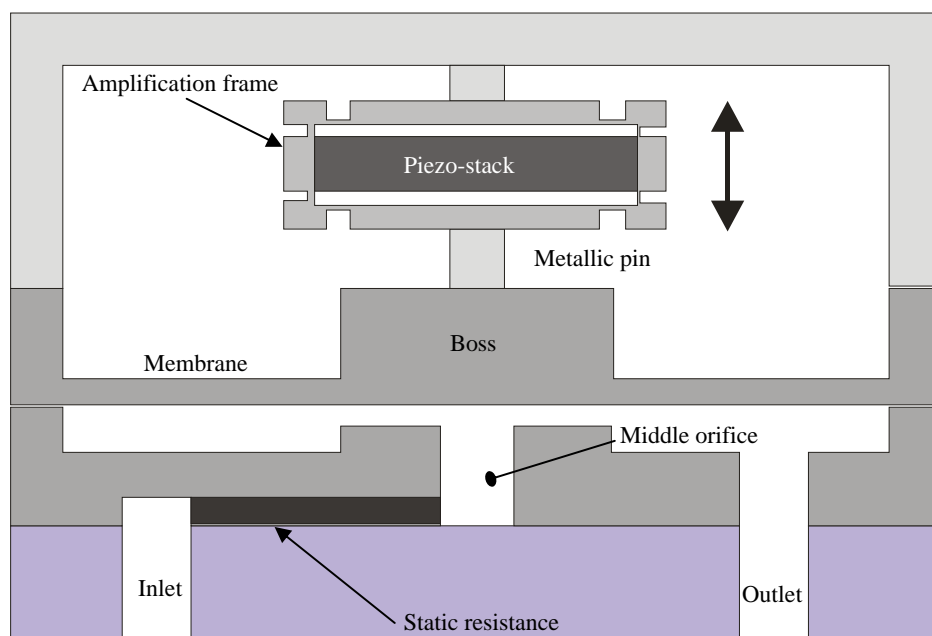


Figure 4-1: Schematic cross-sectional view of piezoelectric microvalve.

4.2 Design description

Figure 4-1 shows the cross section of the device based on fine and micromachined piezoelectric actuated microvalve. The valve is composed of two main components. The first is a fine machined part. It includes the piezo stack along with a metal amplification frame. The metal amplification contains a slot with threads on it in which a metallic pin can be screwed to deflect the membrane upon piezo actuation. The second part is the microvalve, which is realized by standard micro-machined techniques.

In the following sections, a detailed description of the piezo actuator will be provided along with the characterization of the microvalve. The details about the micro-machined part have already been presented in the previous chapters 2 and 3.

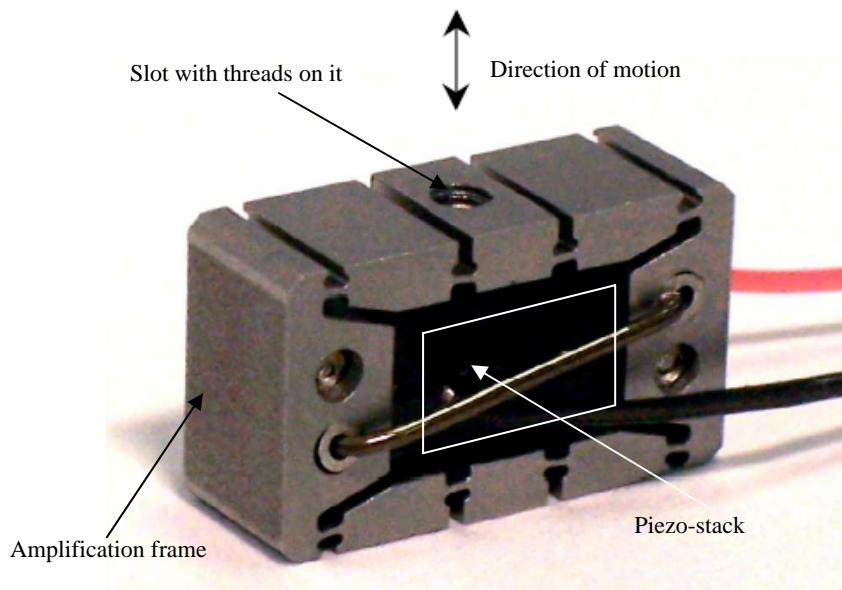


Figure 4-2: A flex-tensional piezoelectric actuator (FPA) consists of a piezo stack and a metal amplification frame around it.

A DSM's (Dynamic Structures and Materials, LLC.) flex tensional piezoelectric actuator (FPA) shown in Figure 4-2 has been selected to overcome the problems addressed in chapter 3. The active element in it is the PZT stack in the centre of the stainless steel mechanical amplification frame. The PZT stack is mechanically pre-loaded to ensure bidirectional movement. As the applied voltage on the piezo stack is varied, the piezo stack expands or contracts. DSM's FPA mechanism design uses mechanical amplification to enhance the small levels of expansion found in PZT materials to create many time greater stroke levels [205]. The specifications for the piezoelectric actuation are given in the Table 4-1. It can produce a blocking force of 40 N which is 10 times larger than the required force and a deflection of 80 μm which is more than the maximum required deflection of 60 μm for 'High flow low pressure' operational mode (see Table 2-7) [205]. In the following section, the characterization of the piezoelectric actuator is presented.

Table 4-1: Piezoelectric actuator specifications.

Stroke	80 $\mu\text{m} \pm 10\%$
Stiffness	0.5 N/ $\mu\text{m} \pm 10\%$
Blocked force	40 N
Resonant Frequency	1700 Hz $\pm 5\%$
Size with metal frame	8 mm x 10 mm x 17 mm

4.3 Characterization of piezoelectric actuated microvalve

4.3.1 Experimental setup

A schematic of the measurement setup is shown in Figure 4-3. A flow meter of Bronkhorst is used to measure the gas flow. The maximum volumetric flow that has been used is 250 ml/min. The precision of the flow meter is 1 % of the maximum flow. In front of the flow meter an air filter is placed to purify air from dust particles, to avoid congestion of the valve. The pressure is measured by the pressure gauge in between the flow meter and the valve.

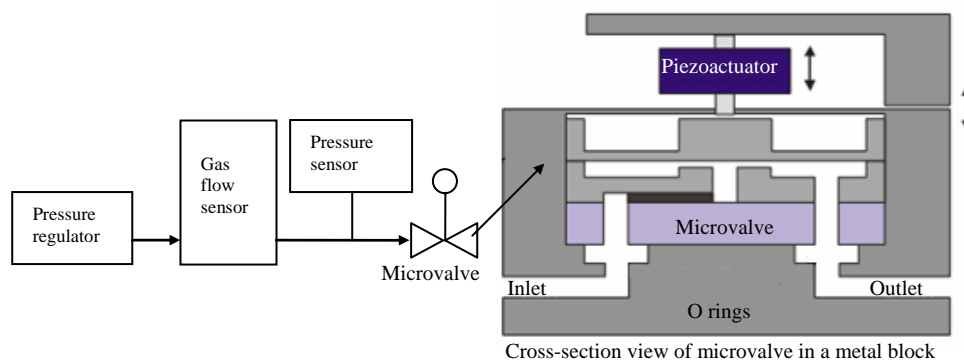


Figure 4-3: Experimental setup.

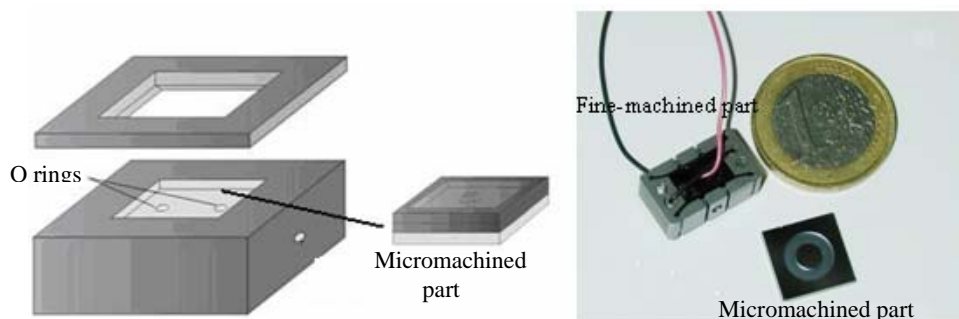


Figure 4-4: Micromachined part is mounted in a metallic holder for characterization.

4.3.2 Volume flow rate measurements

The flow rate is measured as a function of gap height s . The measurement procedure starts by mounting the micromachined part into the holder as shown in Figure 4-4. Then the piezoelectric actuator along with metallic pin is brought into contact with the silicon membrane boss. As soon as the metal pin attached to the piezo comes in contact with the boss of the silicon membrane, a voltage is supplied to the piezoactuator to expand. Continuously increasing voltage is supplied the piezoactuator until the volumetric flow of less than 1 ml/min is reached. Then the valve is gradually opened with 1 micron step size until the flow reaches its maximum constant value. To achieve 1 μm step size, the piezoactuator is supplied with 2.5 volts per step. A delay of 20 seconds for each step is maintained to observe the flow

behavior. The volume flow rate is measured with the pressure differences of 4 bar between inlet and outlet. Valves with three different lengths of the static resistance (30, 32 and 34 mm) are characterized. Figure 4-5 shows the measured volumetric flow rates at a pressure difference of 4 bar for a valve with static resistance of 34 mm in length. It can be seen that the results predicted by the incompressible gas model are in good agreement with the measurements.

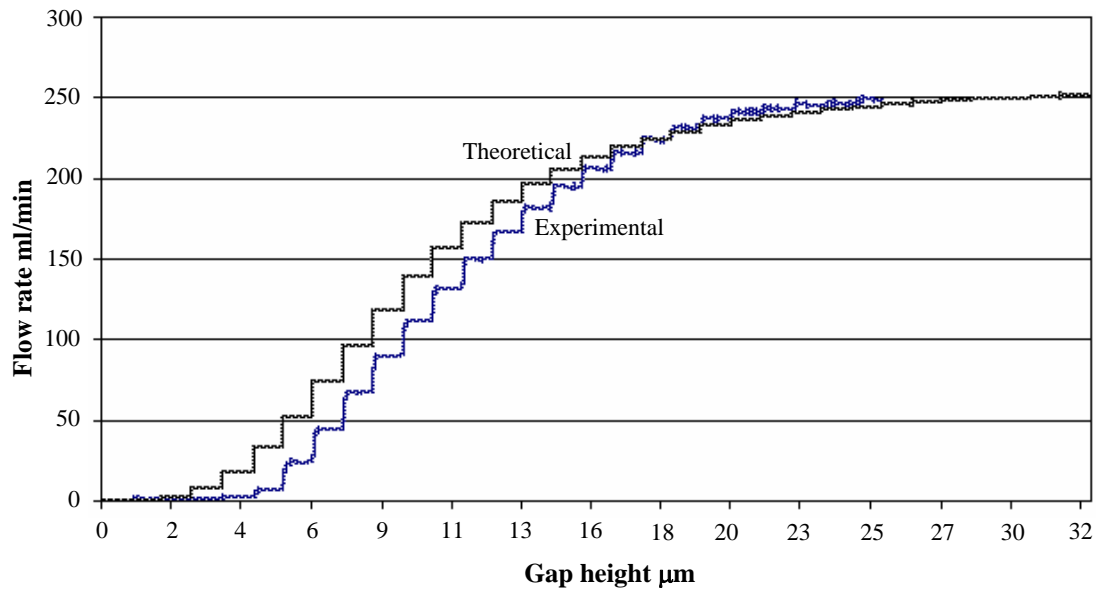


Figure 4-5: Flow rate measured at a pressure difference of 4 bar between inlet and outlet. The results predicted by the incompressible gas model are in accordance with the measurements.

4.3.3 Controllability

To demonstrate the performance of the piezoactuator for precision control, smaller steps of 200 nm are taken by supplying the voltage of 0.5 volts per step. It can be observed from Figure 4-6 that flow can be controlled at any stage with the smooth steps taken by piezoactuator. The controlled flow rate of 4 ml/min confirms that any required flow rate can be achieved by the appropriate supply of voltage per step. Previously, gas flow control was limited by the design parameters of the screw and the gear reduction ratio of the stepper motor used. Additionally the use of piezoelectric actuator makes possible to get rid of the unnecessary longer steps taken by the stepper motor due to the friction in the screw (see Figure 3-15).

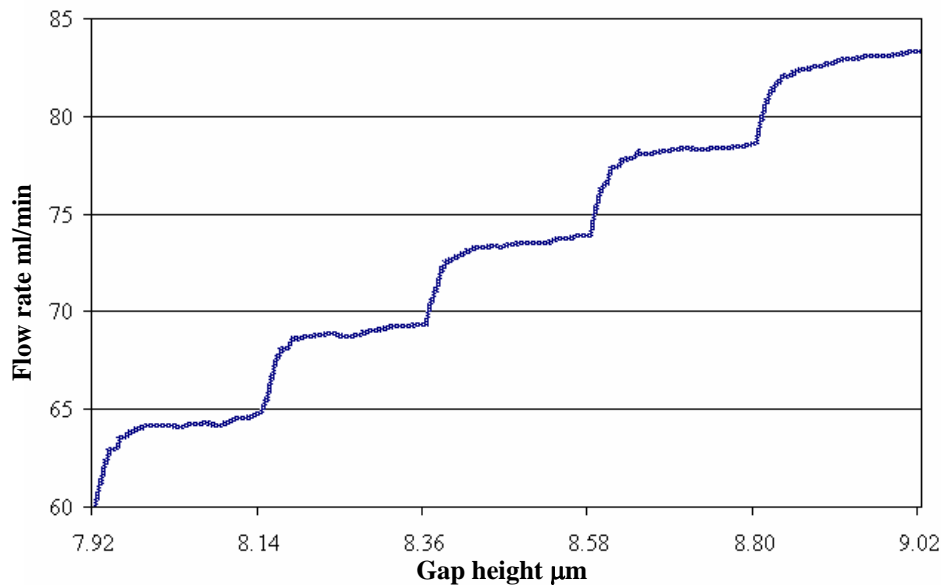


Figure 4-6: Piezoactuator provides the smoother steps as compared to irregular longer steps taken by the stepper motor due to friction.

4.3.4 Backlash behavior

In Figure 4-7, the dynamic behavior of the piezoactuator is shown. The microvalve has been operated back and forth. It is opened, closed and kept in different intermediate states by controlling the voltage supply to the piezoactuator. The time interval in between the steps is kept constant to examine any delay in steps. It can be observed that the flow behavior is same for all the relative steps taken by the piezoactuator. The piezoactuator has shown no backlash during valve operation. Previously the performance of the microvalve was affected by the backlash of the stepper motors used (see Figure 4-7). We can see from the graph that the stepper motors used in the past with different gear reduction ratios of 120:1 (without backlash) and 256:1 (with backlash) needed at least 6 and 60 steps, respectively, to change their direction. Hence the use of piezoactuator improves the performance of the valve operation by having zero backlash behavior.

4.3.5 Hysteresis

Hysteresis effects have also been studied. The microvalve is connected to high pressure a gas reservoir and a constant flow rate is maintained. To observe the hysteresis, the microvalve is operated for different intermediate states with different time steps. The pressure difference of 4 bar is maintained between the inlet and the outlet. Initially the membrane is deflected upward by contracting the piezo in three steps of 5 volts each. A delay of 1 hour for each step is maintained. After the completion of the third step, finally the membrane is deflected downward by piezo expansion in a same manner to reach the initial flow state. Similarly more experiments are performed with a delay of 2 to 4 hours in between steps to observe the difference in relative steps due to hysteresis effect.

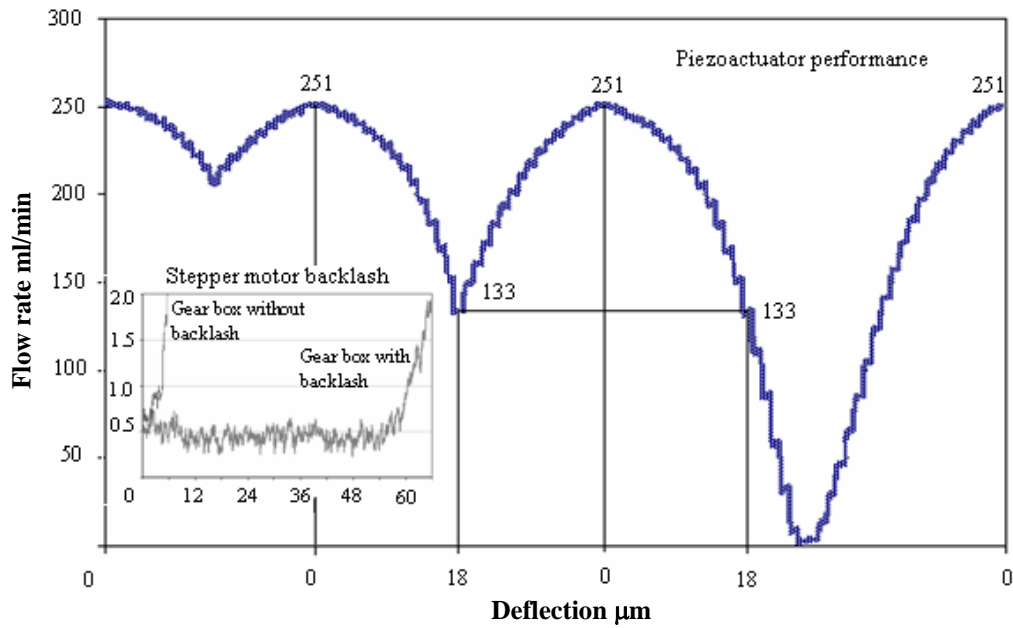


Figure 4-7: The use of piezoactuator improves the performance of the microvalve by reducing the backlash problem previously shown by the stepper motor.

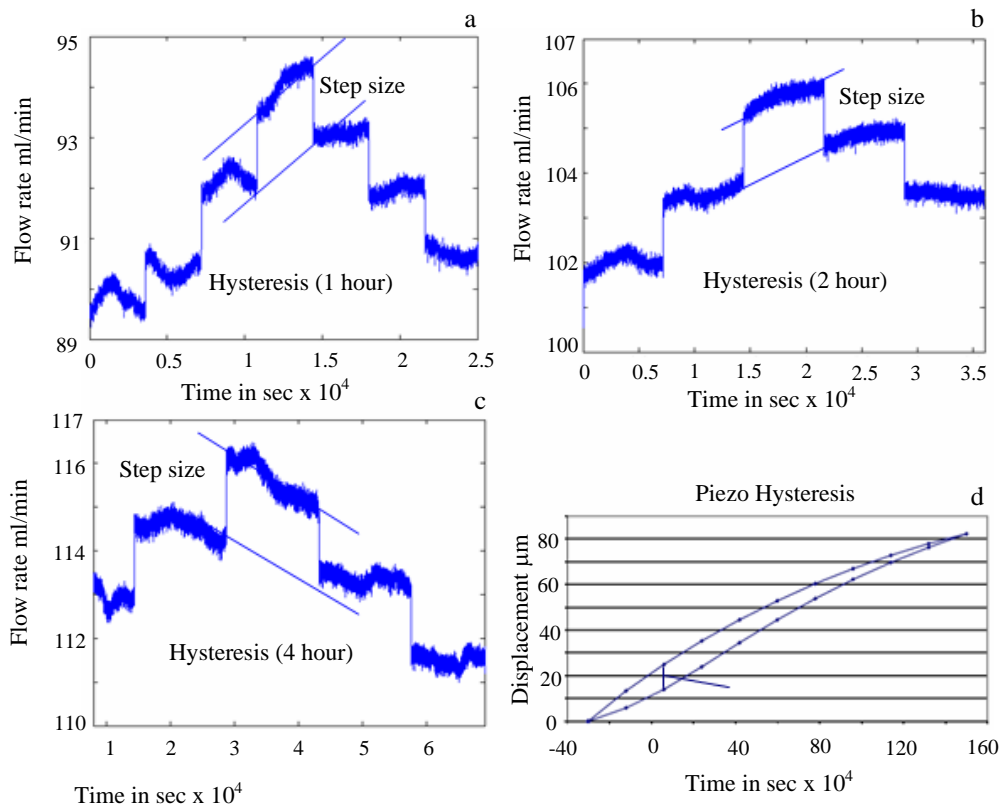


Figure 4-8: Hysteresis: Piezo exhibits almost no hysteresis over a small range of operation as the step size taken by the piezo is same.

Three graphs are shown in the Figure 4-8. It can be seen that the size of the corresponding steps taken by the piezo are same. The graphs illustrate that the piezo exhibits almost no hysteresis over a small range of operation. It can also be seen that there is a little deviation of 1-2 ml/min in flow for comparable steps. This variation might be caused by the change in temperature and pressure over a long period of time. But if the piezo will be used over an entire range of displacement it exhibits the material hysteresis (see Figure 4-8 d). Dipole hysteresis in piezoelectric actuator displacement manifests itself as a difference in displacement path in the forward stroke compared to the return stroke. Therefore, the correlation between voltage and strain in piezoelectric materials is typically not linear. Open-loop hysteresis is generally around 10 to 15% of full scale, depending upon the particular piezo material. The output of the piezo-actuator in a standard displacement graph reflects this variation in forward versus return path displacement (see Figure 4-8 d). To compensate for the change in position, one can drive the piezo actuator to a slightly different voltage in the return move to get back to the same starting position.

4.4 Conclusions

This new design of the microvalve and its characterization presented above show promising improvement in the features like flow rates, continuous control at any stage with low power consumption and low hysteresis as compared to microvalve actuated by the stepper motor. This new approach has made it possible to achieve the following benefits:

- The performance of the microvalve has been improved as the use of piezoelectric actuator makes it possible to get rid of the unnecessary longer steps taken by the stepper motor due to the friction in the screw.
- Piezoelectric actuator provides the benefit of controlling the flow continuously over an entire range of valve operation. Additionally it can control the flow of any desired range by taking smaller voltage steps.
- The use of piezoactuator made it possible to get rid of backlash problem occurred in the stepper motor. It enhances the switching performance of the valve by showing zero backlash behavior.
- Piezoactuator shows almost no hysteresis.

It can deliver a controlled flow rate of 250 ml/minute for a differential pressure of 4 bar. Comparison between predicted and measured flow rates shows good agreement. Testing results at room temperature demonstrated the flow can be controlled continuously at any stage during valve operation. This specific DSM piezoactuator proved to be robust and enhances the performance by showing almost no hysteresis and less power consumption.

The disadvantage is that a voltage supply is required to keep the valve at a fixed position, in comparison to the design described in chapters 2 and 3.

The issue to optimize the geometrical design to accommodate more pressure ranges in a single design will be addressed in the following chapter.

Chapter 5

5 Pressure regulator microvalve

Abstract

The design concept, fabrication and the characterization of the pressure regulator microvalve, which provides the benign feature of accommodating more than one pressure regime, is presented in this chapter. Although the fabricated device delivers the designated features, but there are certain issues such as flow controllable range and the size of the device. These issues are discussed and solutions are proposed.

5.1 Introduction

In the previous chapters it has been demonstrated that a valve can be designed which can fulfill the feature like flow regulation at high inlet pressure, robust against burst pressure, flow control at different intermediate states with certain precision, low power consumption, fast switching and low hysteresis. But at the same time it was not possible to design a single valve which can accommodate different operational regimes as the difference between the resistances was quite large. To fit all operational regimes in a single valve design the size of the static resistance and the orifice needs to be adjustable that is not possible for valve geometry with fixed parameters (see section 2.3).

In this section a new design concept based on the principle of pressure regulation is described. It is a continuation of the piezoelectrically actuated microvalve which is based on the combination of fine and micromachining. The cross sectional view of the valve is shown in Figure 5-1. This new concept has made it possible to accommodate more than one pressure regime in a single design.

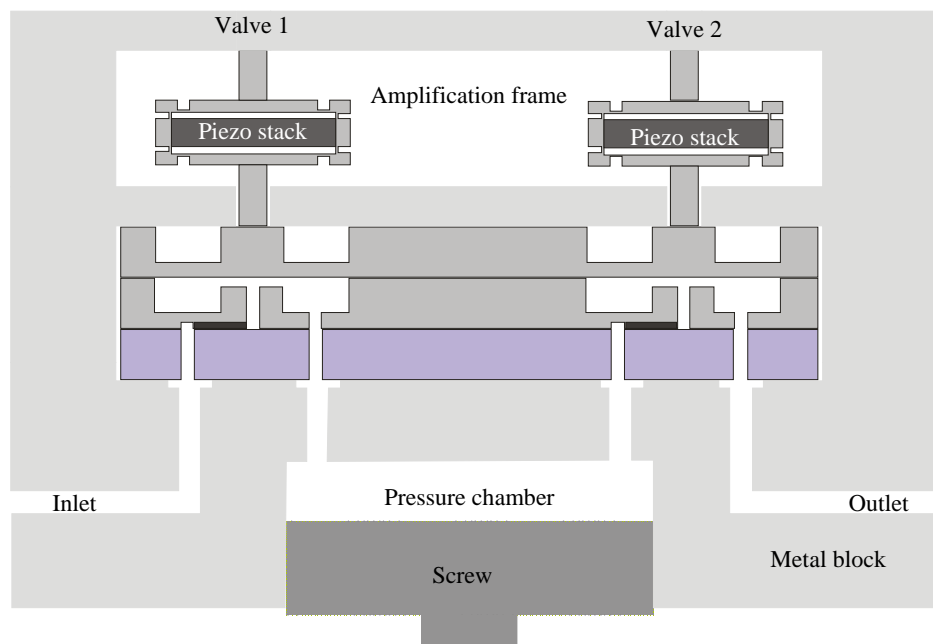


Figure 5-1: Cross-sectional view of the pressure regulator microvalve.

5.2 Valve design and modeling

The design shown in Figure 5-1 is based on the combination of fine and micromachining. To describe the functionality of this concept, it is divided into two sections. Each section (Valve 1 & 2) comprised of piezoelectric actuator which is fine machined part and controls the flow through the micromachined part. The piezoelectric actuators are selected by considering all the requirements given in the chapters 2, 3 and 4. But other actuation principles can be employed depending on the specific requirements. Valve 1 regulates the desired pressure in the pressure chamber for its high inlet pressure. And Valve 2 delivers the required flow for the pressure regulated in the pressure chamber.

Based on the modeling details given in chapter 2, the parameters of the micromachined parts are derived for two operational modes ‘Typical’ and ‘Low flow high pressure’. The design parameters used are given in the Table 5-1.

Table 5-1: Design parameters for micromachined part of section 2.

a_1	a_2	l	w	h	s_1 & s_2
0.1 mm	2mm	20 mm	400 μm	50 μm	50 μm

a_1 and a_2 : inner and outer radius of the valve seat, l : length of the channel (static resistance), w and h : width and the height of the channel.

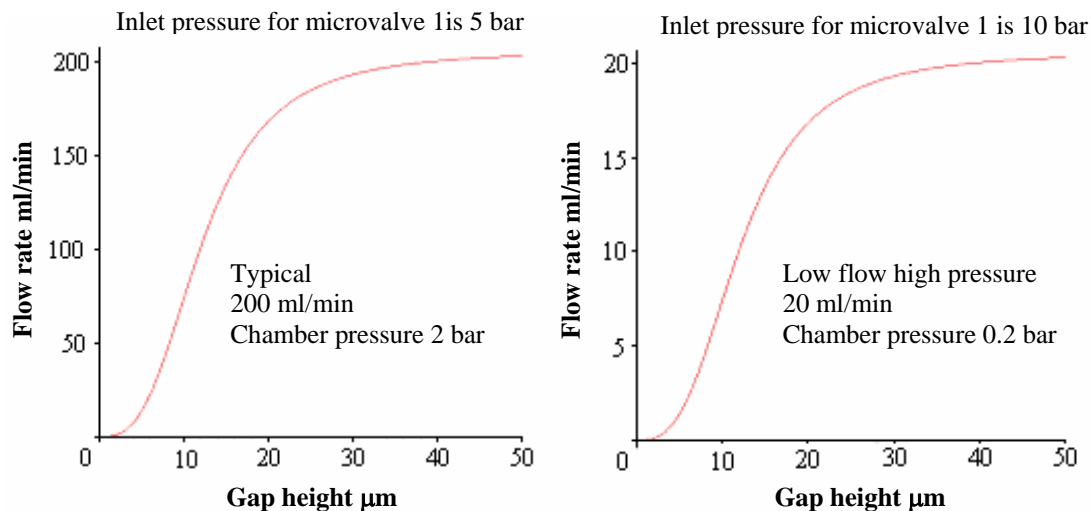


Figure 5-2: Flow characteristic curves for ‘Typical’ and ‘Low flow high pressure’ modes for control valve 2.

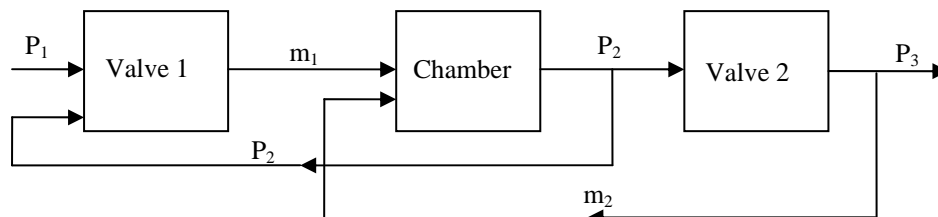
First the design specifications for the micromachined part Valve 2 are derived. To derive these specifications, first it is assumed that the Valve 1 for its inlet pressure of 5 and 10 bar can maintain pressure difference of 2 and 0.2 bar respectively between chamber and the outlet by controlling the flow. Parameters for valve 2 are derived in such a way that it can accommodate more than one pressure regime and deliver the controlled flow rate for the pressure regulated in the chamber. The combination of variable resistance and static resistance is preferred as it provides more linear range of operation (see section 2.1.3). The flow through valve 2 for the pressure difference of 2 and 0.2 bar between chamber and the outlet are shown in Figure 5-2. It can be seen that for the parameters given in Table 5-1 for Valve 2, the flow of 200 and 20 ml/min can be achieved within the same gap height of 50 μm for their respective pressure difference of 2 and 0.2 bar. So it can be concluded that if the Valve 1 can regulate the pressure difference of 2 and 0.2 bar between chamber and the outlet for its inlet pressure of 5 and 10 bar then the valve 2 with the selected parameters can deliver the flow rates of 200 and 20 ml/min respectively.

Table 5-2: Design parameters for microvalve 1.

a_1	a_2	l	w	h	s_1 & s_2
0.1 mm	2mm	20 mm	400 μm	50 μm	25 & 2 μm

a_1 and a_2 : inner and outer radius of the valve seat, l : length of the channel (static resistance), w and h : width and the height of the channel.

Secondly simulations have been performed to examine the operation of the Valve 1 in combination with the chamber and the valve 2. The design parameters used for simulations for Valve 1 are given in Table 5-2. Simulations are performed for different gap heights for the valve 1 while the valve 2 is fully opened.



P_1 : Inlet pressure to valve 1, m_1 : Mass flow rate through valve 1, P_2 : chamber pressure, m_2 : Mass flow rate through valve 2, P_3 : Atmospheric pressure

Figure 5-3: A flow diagram for the simulations performed.

A flow chart is given in Figure 5-3 to describe the simulations process. It consists of three blocks representing valve 1, chamber and valve 2 respectively. P_1 is the inlet pressure to the valve 1, P_2 is the chamber pressure and inlet pressure to valve 2 and P_3 is the atmospheric pressure. Simulations are performed in such a way that valve 1 controls the flow to the chamber by changing the gap height of the membrane to maintain the required chamber pressure. For different gap heights of 25 μm and 2 μm of valve 1, the characteristics curves for the chamber pressure and flow through the valve 2 are shown in Figure 5-4. It can be seen that valve 1 for its inlet pressure of 5 bar can maintain the chamber pressure of 3 bar for a gap height of 25 μm . It can also be seen that valve 2 delivers flow rate of 200 ml/min (1.2×10^{-5} kg/s) for its inlet pressure of 3 bar (chamber pressure). Similarly it can be observed that a chamber pressure of 1.2 bar and its corresponding flow of 20 ml/min (4.5×10^{-7}) through valve 2 can be obtained by controlling the flow through valve 1 with a gap height of 2 μm .

It can be concluded from all the modeling details that it is feasible to accommodate more than one pressure regime in single design. Based on this concept of pressure regulation, a valve is fabricated and characterized.

5.3 Fabrication

The three dimensional view of the micromachined part is shown in Figure 5-5. It is comprised of three wafers. The bottom wafer is Pyrex which contains the inlet and the outlet orifices. The middle wafer is from silicon and carries the valve seats which act as variable resistances and also contains a rectangular channel at its bottom, which act as a static resistance. The inlet in the Pyrex wafer opens in the static resistance of the valve 1 which is connected to the valve seat by the middle orifice. The outlet of the valve 1 opens into the

pressure chamber which is connected to the valve 2 via another orifice (see Figure 5-5). The top wafer is also from silicon having circular membranes with boss, which controls the gas flow upon deflection.

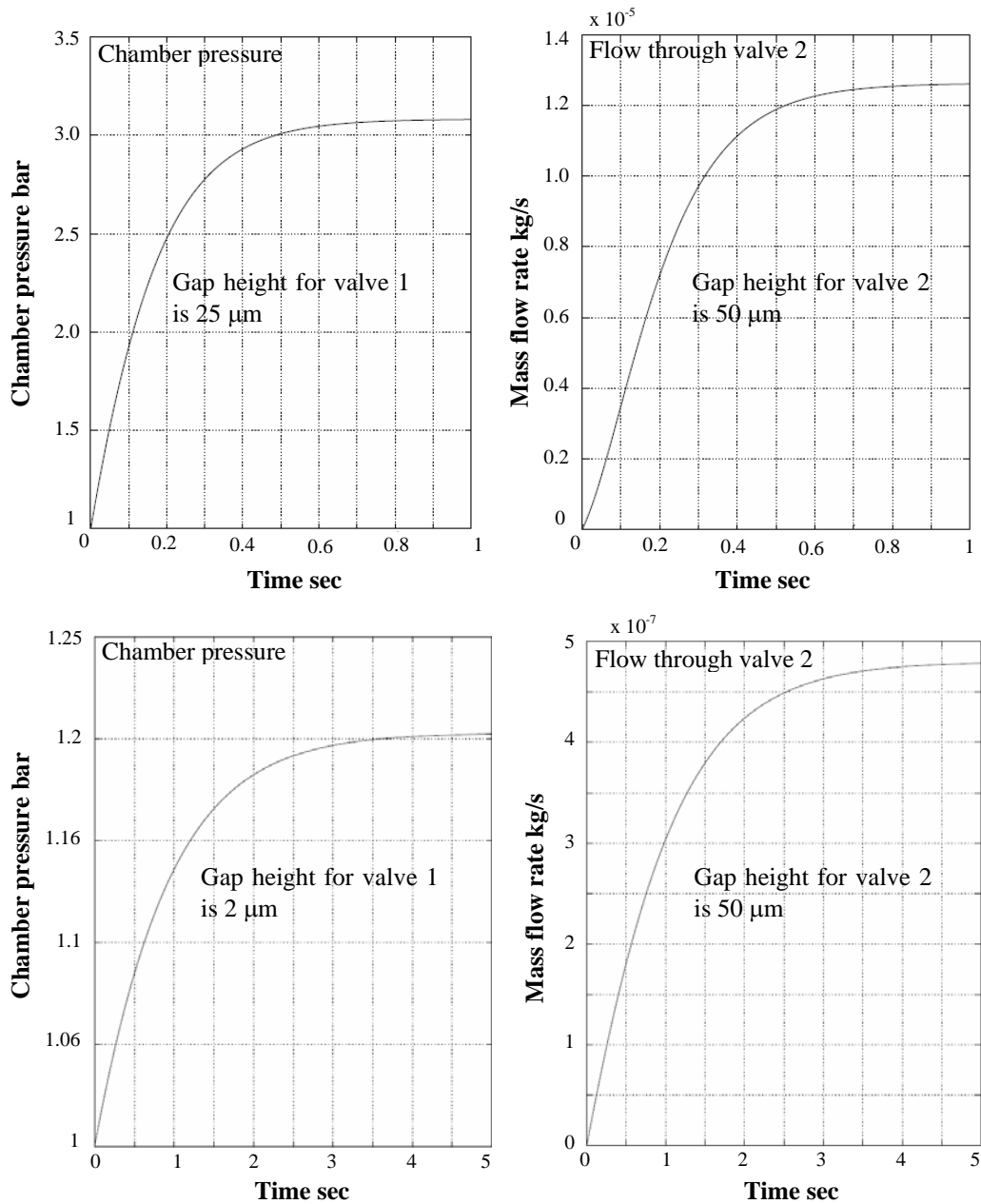


Figure 5-4: Flow characteristic curves for chamber pressure and flow through the valve 2.

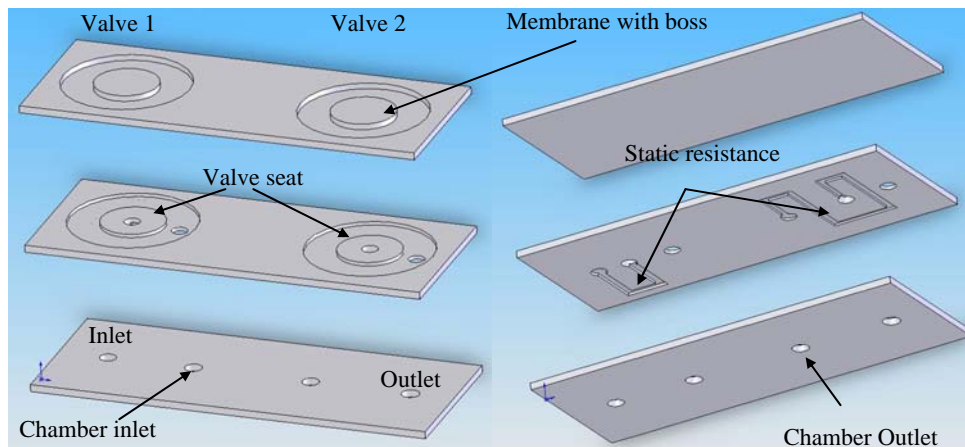


Figure 5-5: Three dimensional view of pressure regulator valve.

The two silicon wafers are fusion bonded at 1100 °C in N₂ atmosphere (see Figure 5-6). An electronic Vision Aligner is used to align and to pre bond the wafers. The final step is to anodic bond the fusion bonded silicon wafers and Pyrex wafer. The anodic bonding is performed on a hot plate set up. Finally the wafers are diced from topside. Dicing foil is applied on the backside of the stack of the three wafers to protect the inlet and the outlet from the particle contamination.

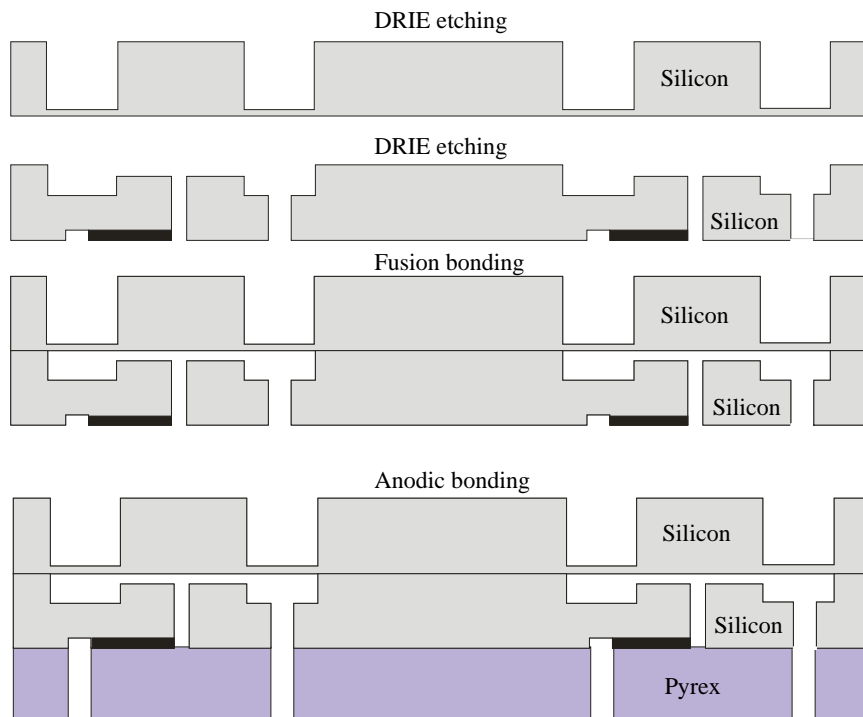


Figure 5-6: Fabrication process for micromachined part.

5.4 Characterization

In this section the characterization of pressure regulator microvalve is described. The performance of the valve 1 is examined by maintaining the required pressure in the chamber and the volume flow rate through the valve 2 is measured as a function of applied voltage to the piezoelectric actuator.

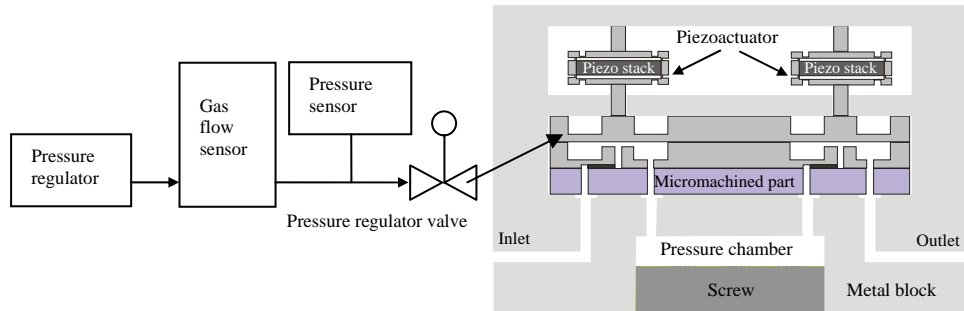


Figure 5-7: Experimental setup.

Two different piezoelectric actuators are used to characterize the pressure regulator valve. The piezoactuator used previously for the single valve design (see chapter 4) is coupled to valve 2 and for valve 1 a new piezoelectric actuator with the following parameters is used.

Table 5-3: Piezoelectric actuator specifications used for valve 1.

Stroke	145 $\mu\text{m} \pm 10\%$
Stiffness	1 N/ $\mu\text{m} \pm 10\%$
Blocked force	145 N
Resonant Frequency	1400 Hz $\pm 5\%$
Size with metal frame	17 mm x 28.5 mm x 12 mm

5.4.1 Chamber pressure measurements

The pressure difference between chamber and the outlet is measured as a function of applied voltage to the piezoelectric actuator. The measurement procedure starts by mounting the micromachined part into the holder as shown in Figure 5-7. Then the piezoelectric actuators along with metallic pin are brought into contact with the membrane boss. As soon as the metal pin attached to the piezoelectric actuators came in contact with the boss of the silicon membrane, a pressure of 5 bar is applied to the inlet of valve 1 by a pressure reservoir connected to it. Then the pressure difference between the chamber and the outlet is examined when both valves are fully opened. The size of the chamber used for characterization is 1 cm³ (see Figure 5-1). It can be varied by adjusting the screw at the bottom of the holder. Figure 5-8 shows the pressure difference between the chamber and the outlet as a function of voltage applied to the piezoelectric actuator of valve 1. It can be seen that for an inlet pressure of 5 bar, the pressure difference between the chamber and the outlet is 2.4 bar. Now in order to achieve the required pressure difference of 2 bar, a continuous voltage is supplied to the piezoactuator to expand. Upon actuation, the piezoelectric actuator deflects the membrane to

control the flow till the required pressure difference is achieved. It can be seen that the pressure difference of 2 bar between chamber and the outlet can be achieved for the voltage supply of 46 volts. Similarly it can also be observed that a pressure difference of 0.2 bar can also be achieved by controlling the flow through valve 1 for a voltage supply of 60 volts. An inlet pressure of 5 bar is applied at the inlet of the valve 1 in both cases. We could not characterize the device for the inlet pressure of 10 bar as there was a leakage in the system if the inlet pressure is more than 8 bar.

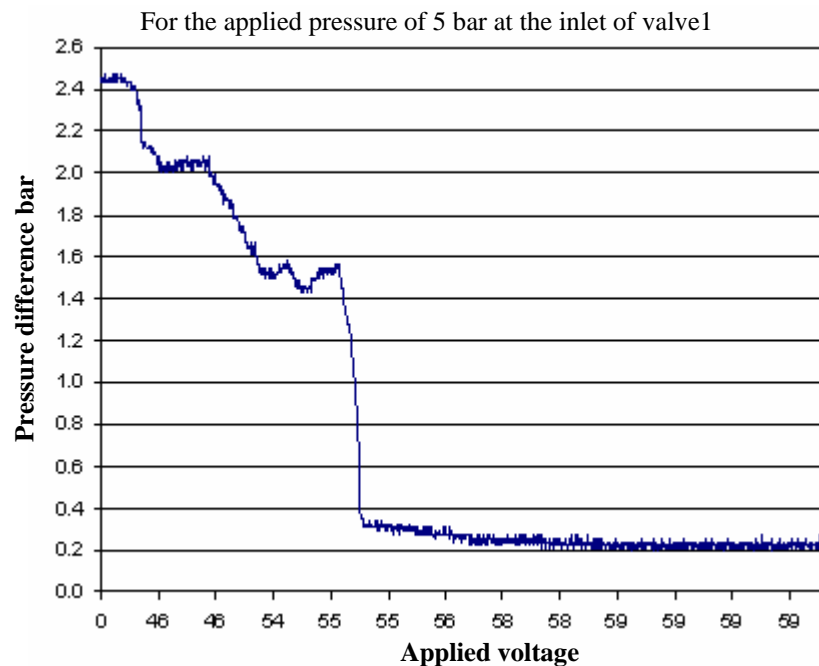


Figure 5-8: Pressure difference in between chamber and the outlet as a function of voltage supply to piezoactuator. The inlet pressure to the valve 1 is 5 bar for this measurement.

The device for the flow control through valve 2 is also characterized. It is examined whether it is possible to control the flow for different intermediate states in combination with chamber pressure and the valve 1. Figure 5-9 shows the flow rate through valve 2 as a function of applied voltage to the piezoelectric actuator for the pressure difference of 2 bar between the chamber and the outlet. It can be seen that flow starts from 100 ml/min because it is not possible to start from 0 as the pressure difference between the chamber and the outlet will be no longer equal to 2 bar as the valve 2 is closed. Similarly, it is difficult to control the flow through the valve 2 at the initial state as flow rises steeply for a smaller change in the gap height which makes it difficult to maintain the required chamber pressure. The linear part of the flow characteristic curve is chosen to examine the flow rate at different intermediate states. To start this experiment, first a flow of 100 ml/min is achieved by maintaining a pressure difference of 2 bar between chamber and the outlet. It is done manually by actuating both piezoelectric actuators till the required pressure difference of 2 bar and its relative flow of 100 ml/min is achieved. Then a small step is taken by the piezoelectric actuator coupled to the valve 2 by decreasing the voltage supply to it. It deflects the membrane up. This results in

the pressure change in the chamber. In order to maintain the pressure in the chamber valve 1 is further opened by reducing the voltage to the piezoactuator coupled to valve 1 until the pressure reaches its required value. The same procedure is repeated till the flow through valve 2 reaches its maximum value of 200 ml/min. It can be seen from Figure 5-9 that flow through valve 2 in combination with chamber pressure and valve at different intermediate states can be controlled.

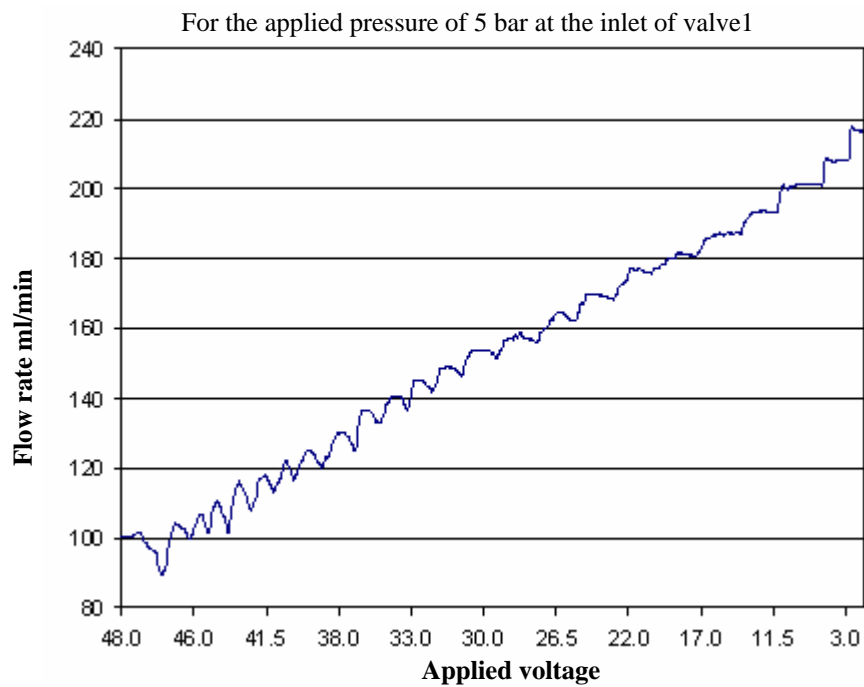


Figure 5-9: Flow rate through valve 2 as a function of voltage supply for a pressure difference of 2 bar between chamber and the outlet.

A similar approach is adopted to characterize the device for the low flow regime of 20 ml/min. The flow rate through valve 2 is examined for a pressure difference of 0.2 bar between the chamber and the outlet. Figure 5-10 shows that it is possible to control the flow at different intermediate states through valve 2 in combination with chamber pressure and valve 1 for a pressure difference of 0.2 bar.

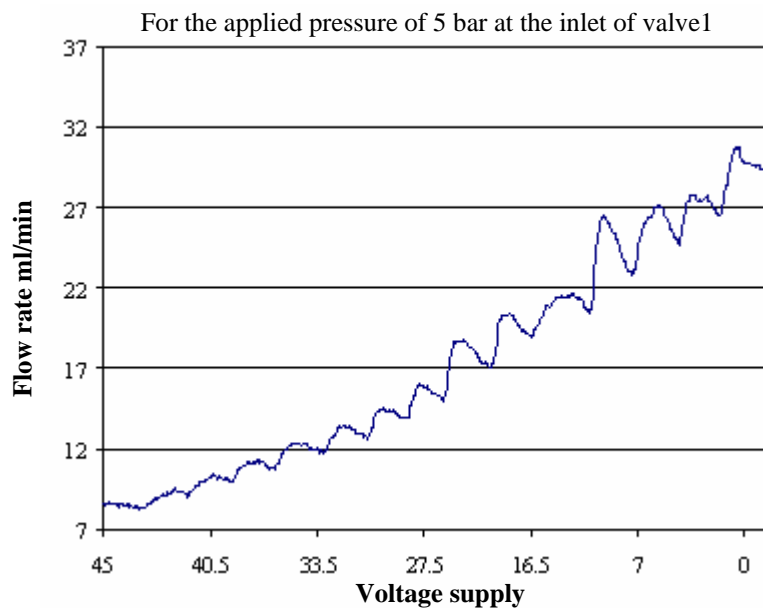


Figure 5-10: Flow rate through valve 2 as a function of supplied voltage for a pressure difference of 0.2 bar between the chamber and the outlet.

5.5 Conclusions

A new concept has been presented to design and develop a valve using the combination of fine and micromachining. It is based on the principle of pressure regulation for different inlet pressures. This new concept and its characterization have made it possible to achieve the following features:

- Pressure can be regulated to any desired value for the inlet pressure of 2 to 10 bar. This characteristic provides the benevolent feature to accommodate more than one pressure regime with in a single setup.
- Flow at any intermediate state can be controlled in combination with this pressure regulation.

It is not possible accommodate ‘Low pressure high flow’ regime because of the high difference in resistance. This new approach can also be used directly to control the flow without pressure regulation in the pressure chamber. The valve 1 can provide the enough resistance for high inlet pressures and the valve 2 can control the flow accordingly.

Chapter 6

6 Fusion Bonded Fluidic Interconnects

Abstract

The fabrication and characterization of fusion bonded fluidic interconnects is presented in this chapter. Fluidic interconnects of glass tubes with plain silicon wafers and coated with silicon dioxide and silicon nitride are characterized. Results obtained for high pressure testing and the cause of their breakage are discussed.

6.1 Introduction

The connection of micro devices to the outside world plays a significant role in MEMS applications such as micro flow controllers, micro reactors and fluidic devices in general. With the increase in demand and priority in device reliability issues, one cannot afford to allow flaws in the quality or complexity in the fluidic interconnects. Reliable fluidic interconnects are one of the basic building blocks of integrated fluidic systems.

Different schemes have been introduced for a variety of interconnections. Few used gluing [206, 207], which poses problems such as contamination, low operating temperature and misalignment. Even high temperature ceramic epoxies were used and were found to be prone to leakage at high temperatures [208, 209]. Some introduced soldering (eutectic bonding) on silicon [210], which needs an intermediate layer in between two materials to be bonded and which can't withstand the high temperature. A few have discussed about press fittings [211, 212]. Kovar anodic bonding technique has been used to avoid thermal stresses due to considerably less thermal mismatch with Pyrex at high temperature of 400 °C, however thermal stresses induced during processing led to fracture in the silicon [213]. The previous problem was addressed by bonding of Kovar tubes to silicon with a Pyrex ring, which helped to raise the operating temperature to 600 °C at high holding pressure of 5 atm. [214].

In the following section a new technique is presented which establishes a reliable packaging technology for the connection of MEMS components which operate even at more than 600 °C. This new approach differs from the previous techniques as the interconnections are realized by the direct fusion bonding of glass tubes to the silicon (see Figure 6-1). This is done by annealing the glass tubes to the silicon at their softening temperature of 800°C. Fabrication of the device is discussed in the next section which is followed by the characterization and the conclusions.

6.2 Fabrication

In this section we discuss the surface preparation and annealing conditions of the device. Fusion bonding proceeds by mating silicon and tube surfaces, which are pre-cleaned. At room temperature wafers and tubes positions are fixed by attractive interactions between the hydrophilic surfaces. The wafer and glass tubes adhere at room temperature via hydrogen bonds of chemisorbed water molecules that react during the annealing to form Si-O-Si bonds. With the increase in temperature (400 °C to 800 °C), oxidation reactions take place, which increase the bond strength at the interface [215].

Standard silicon wafers with 10 cm diameter and with a thickness of 525 μm and glass tubes with 6 mm diameter were used for the bonding experiments. Standard Duran glass tubes have been chosen to provide this fluidic interconnection, because they are adapted to standard swage lock connectors. Moreover, the almost identical thermal expansion coefficient of glass tubes and silicon up to 400 °C prevents failure by the thermal mismatch during thermal cycling. To observe the difference in bonding behavior, wafers with silicon oxide and silicon nitride were used, too. For complete process scheme see Appendix E.

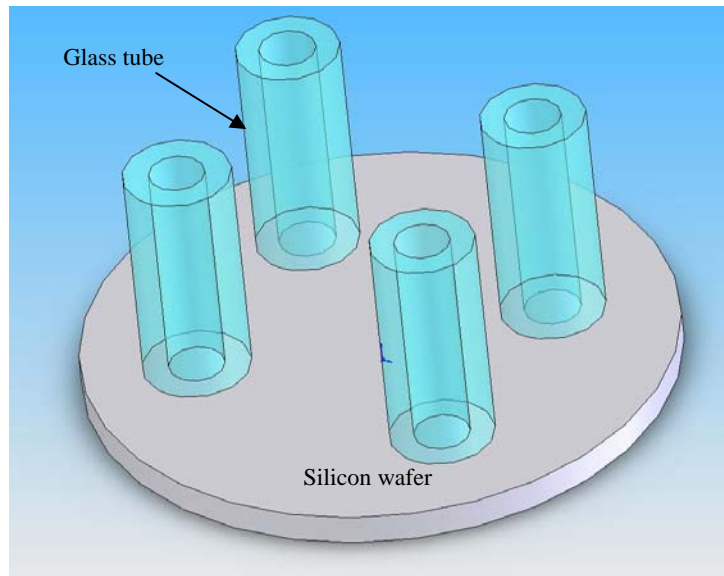
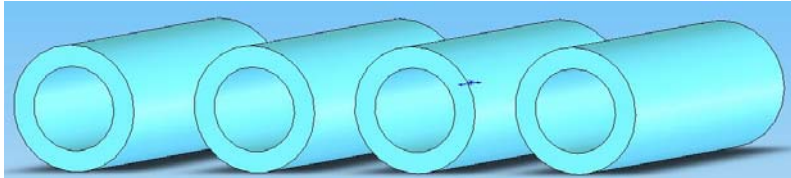

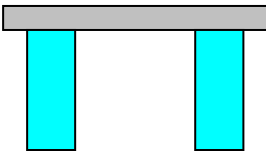



Figure 6-1: Direct fusion bonding of glass tubes with silicon.

Table 6-1: Process steps for fusion bonded fluidic interconnects.

<p>Selection + Dicing of glass tubes + Cleaning</p>	 <p>Duran tubes</p>
<p>Selection of silicon wafer + cleaning</p>	 <p>Silicon wafer</p>
<p>Pre aligning + Fusion bonding + Powder blasting</p>	<div style="display: flex; justify-content: space-around; align-items: center;"> <div style="text-align: center;">  <p>Cross sectional view</p> </div> <div style="text-align: center;">  <p>Three dimensional view</p> </div> </div>

Three groups of experiments were performed.

- Bonding of glass tubes to bare silicon.
- Bonding glass tubes to oxidized silicon.
- Bonding glass tubes to silicon nitride layer

Silicon wafers were cleaned by following a standard procedure; 10 minutes treatment in 100 % HNO₃ and in 69 % HNO₃ (95 °C) respectively, rinsed in DI water and dried with N₂. Standard glass tubes were diced manually into different lengths, cleaned for 20 minutes with 1 % HF to avoid contamination due to wax used in dicing. After cleaning, wafers were placed in the oven at 400 °C and at room temperature) and later on glass tubes were positioned on the silicon wafers in the oven for annealing. Table 6-1 shows the process steps followed in these experiments.

The wafers with glass tubes were annealed at 800 °C for 30 minutes in a controlled way with a temperature ramp of 10 °C per minute as shown in Figure 6-2. Samples were annealed in two different ways as shown in Figure 6-2, to observe how the quality of the bond is affected by this change. All cleaning steps were performed in the clean room but samples were annealed in clean room environment as well as in open lab. The fabricated devices are shown in Figure 6-3.

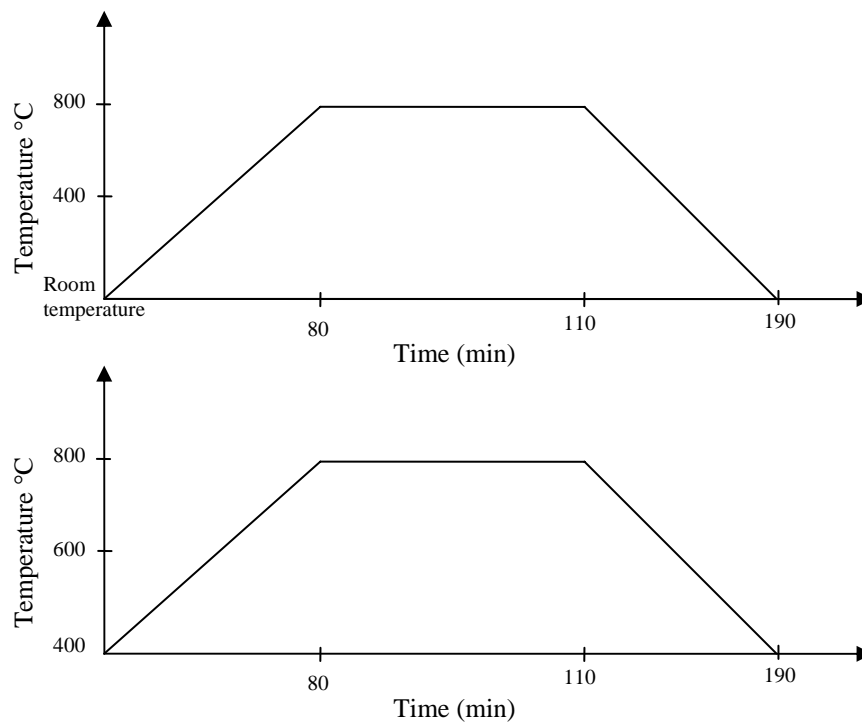


Figure 6-2: Annealing a) From room temperature to 800 °C b) From 400 °C to 800 °C.

The standard Duran glass tubes, diced to the appropriate size of 15-20 mm, have been chosen to provide this fluidic interconnection, because they are adapted to standard swage lock connectors. The glass tubes with outer diameter of 6 mm and with the wall thickness of 1 and 1.5 mm were used.

Additionally, samples with 1 micron of silicon oxide and silicon nitride layers were prepared. The oxide was thermally grown at 1150 °C to a thickness of 1 micron. Low stress silicon nitride of 1 micron thickness was deposited with LPCVD at 850 °C.

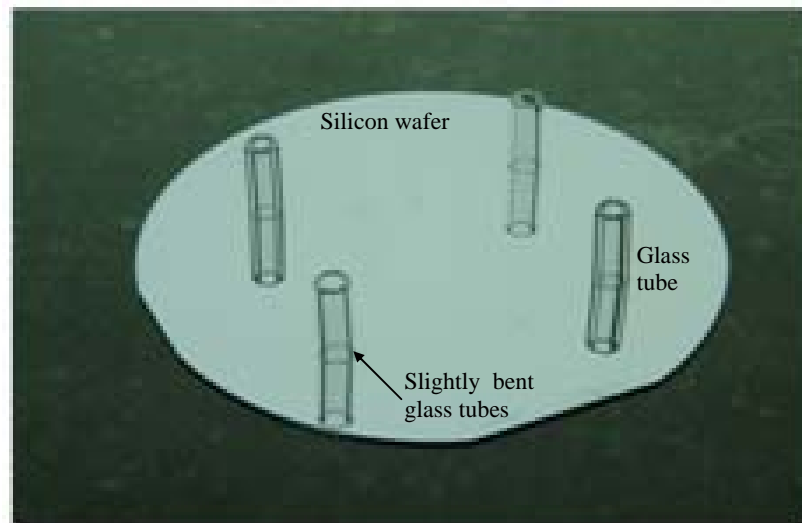


Figure 6-3: Glass tubes bonded to silicon. Glass tubes are slightly bent as they don't have perfect smooth surface due to manual dicing.

6.3 Characterization

6.3.1 Experimental setup

A high-pressure apparatus as shown in Figure 6-4 was used to test the bond strength of the samples fabricated. The maximum pressure that could be measured by the apparatus was 600 bar. Standard swage locks were used to connect the specimens to the test apparatus through connector and fiber. Water flow rate of 100 $\mu\text{l/s}$ was set to increase the pressure gradually till the sample breaks. The pressure increases at the rate of 15 bar per minute approximately. The maximum pressure at which the sample breaks can be obtained from the data acquisition system.

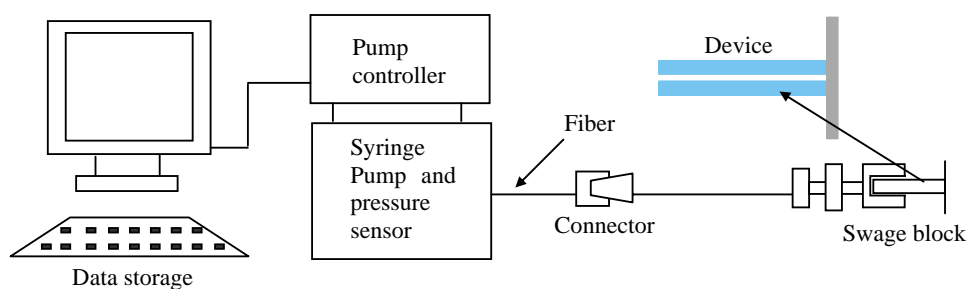


Figure 6-4: Block diagram for high pressure experimental apparatus.

6.3.2 Bond strength analysis

Prior to experiments, it was observed that, after annealing, the glass tubes with 20 mm in length were slightly bent as shown Figure 6-3. It was due to fact that the glass tubes were manually diced which leaves the tube circumferential surface uneven and caused the glass tubes to bend slightly during annealing at high temperature of 800 $^{\circ}\text{C}$ (which is close to the

softening temperature of Duran glass tubes, 825°C). It was also observed that the glass tubes with 20 mm length bend more than the tubes with 15 mm length, which caused problem to connect the specimen with swage lock to perform bond strength test. Moreover, it was observed that there were no non-bonding areas between glass tubes and silicon wafer interface as shown in Figure 6-5. The voids due to particles were expected, as the specimens were prepared in clean room environment as well as in lab. This observation was confirmed after performing bond strength tests.

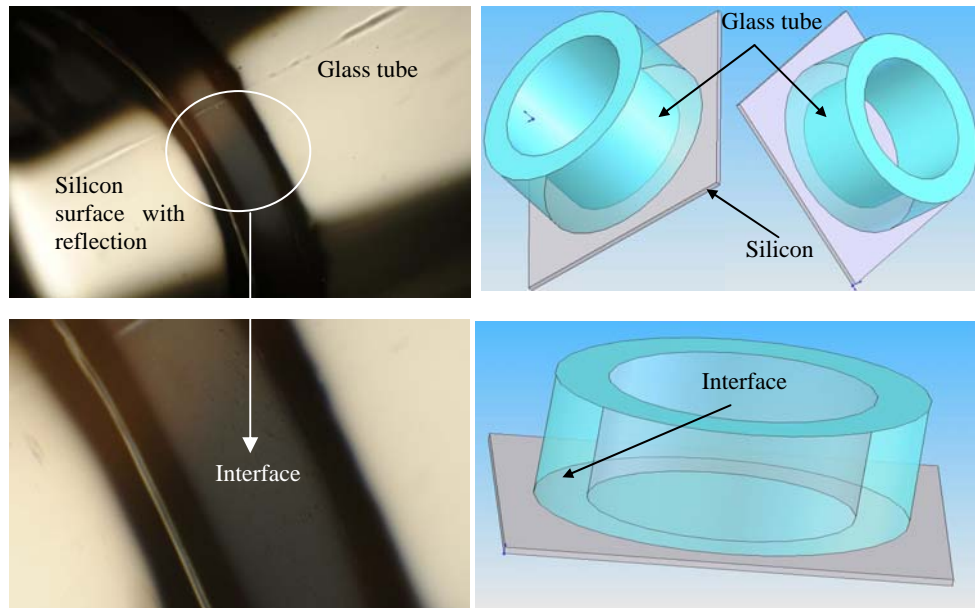


Figure 6-5: Zoom in view for the interface between glass tube the silicon wafer. No voids can be seen due to particles.

To evaluate the fusion bond strength of an interconnection, statistical tests have been performed using the high pressure set up. Results are presented in Table 6-2. It is found from this table that in case of plain silicon, the average burst pressure was 43 bar and 65 bar for the glass tubes with the wall thickness of 1 mm and 1.5 mm respectively. There was 50 % increase in the burst pressure with 50 % increase in wall thickness. It was also observed that in case of large thickness of the tube, breakage was observed in silicon while in case of smaller wall thickness, the glass tubes split from the silicon by leaving some traces of glass on it as shown in Figure 6-6 a, b. The burst pressures in case of the oxide layer are identical with bare silicon. However, the burst pressure differs significantly in case of a silicon nitride layer. The minimum and the maximum burst pressures found were 20 and 30 bar respectively. No breakage in silicon and no traces of glass were found on the silicon nitride as shown in Figure 6-6 c. Parameters shown in Figure 6-6 are given in Table 6-3.

This low burst pressure might results in case of silicon nitride layer, as silicon nitride is dense and hard material. The dense structure of silicon nitride does not provide the open channels to grow oxide, so oxygen diffuses very slowly through the nitride and prevents oxidation of underlying layer. So in case of native oxide layer bond strength quality is good

as interfacial oxide grows almost completely at high annealing temperature of 800 °C. It was also observed that there was no considerable difference in bond strength for the specimens, prepared in clean room and in the normal lab (65 ± 3 bar).

Table 6-2: Burst pressure results for 20 samples each.

Wafer	Wall thickness (mm)	Tube inner diameter (mm)	Average burst pressure (bar)	Standard deviation σ (bar)
Silicon	1.0	4	43	± 2.7
	1.5	3	65	± 4.0
Silicon + SiO ₂	1.0	4	43	± 0.8
	1.5	3	65	± 1.7
Silicon + Si ₃ N ₄	1.0	4	20	± 1.0
	1.5	3	31	± 1.7

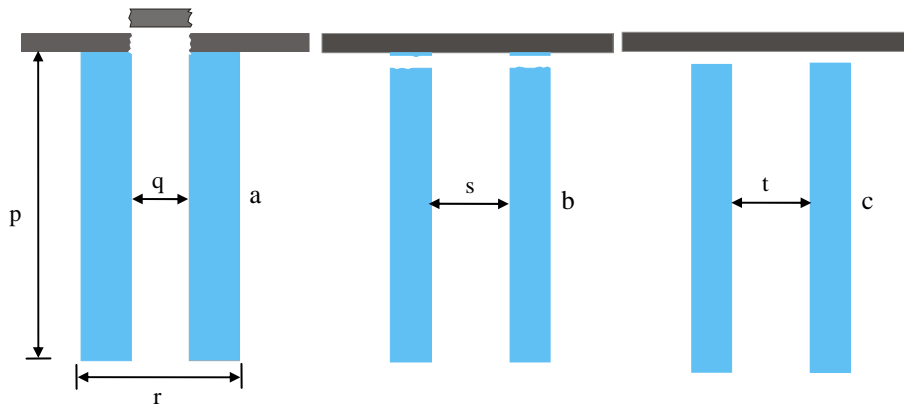


Figure 6-6: a) Breakage in silicon b) Traces of glass in silicon c) No breakage in glass and in silicon.

Table 6-3: Geometrical parameters shown in Figure 6-6.

Parameters	p	q	r	s	t
mm	15	3	6	4	3-4

The burst pressure obtained during experiments is high enough for many applications in Microsystems such as for micro flow controllers, micro reactors and fluidic devices in general. Theory suggests that the burst pressure values should be higher than the values obtained. It is assumed that this difference is due to the thermal stresses produced due to thermal mismatch between the glass tubes and the silicon at high temperatures. It can be seen from Figure 6-7, the thermal expansion coefficient for Pyrex increases rapidly above 450 °C. (Pyrex and Duran, both are borosilicate glass, thus having almost same properties). During cooling the silicon and the glass surfaces experience compressive and the tensile stresses respectively due to thermal mismatch (see Figure 6-7). It is also assumed that the buckling of silicon membrane may occur for the high thermal stress induced. The value of the thermal stress can be calculated as:

$$\sigma_{Thermal} = E\Delta\alpha\Delta T \quad (48)$$

where E is elastic modulus of the material, ΔT is the temperature change $\Delta\alpha$ is the change in thermal expansion coefficient over the process range with change in temperature.

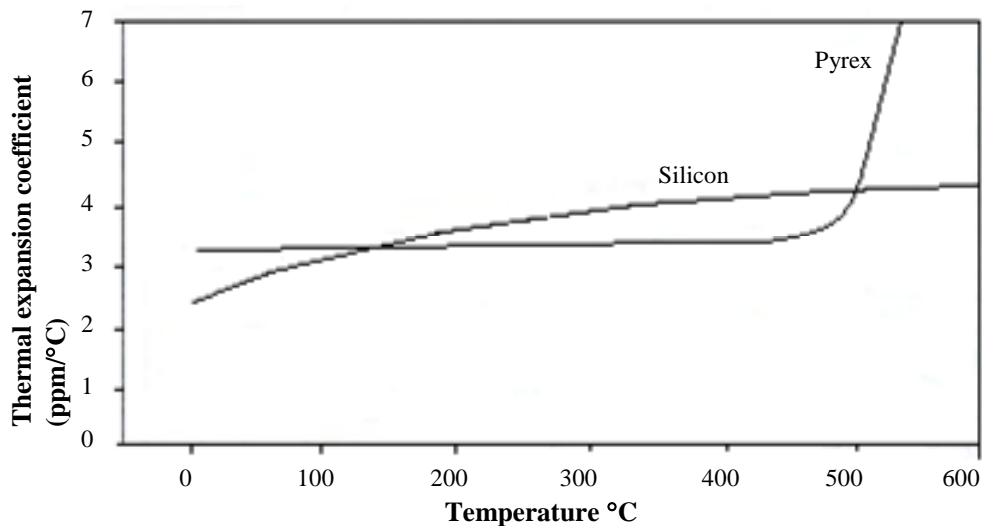


Figure 6-7: Thermal expansion coefficient of Pyrex compared with silicon [216].

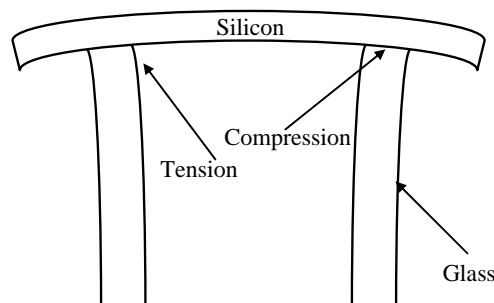


Figure 6-8: Compression on silicon surface while glass surface is in tension due to thermal mismatch during cooling.

To calculate the thermal stress values, thermal properties of borosilicate glass and silicon are needed. But the thermal properties of borosilicate glass are available only up to 600 °C. But Jean et al. [217] pointed out that when borosilicate glass is treated above 700 °C depending upon the time period, the cristobalite gradually precipitates out of the initial amorphous mixture. The precipitation of the cristobalite in the initially amorphous glass mixture is discouraging because its large thermal expansion coefficient (50 ppm/°C) and its volume change associated with its martensitic transformation from tetragonal to the cubic phase at about 150-200°C dramatically reduces the thermal shock resistance and the mechanical strength of the borosilicate glass. To get an improved estimate of $\sigma_{Thermal}$, an

average value of thermal expansion coefficient of 27 ppm of SiO₂ cristobalite is used instead of 50 ppm [218]. It gives the thermal stress value of 4 GPa which is much higher than the compressive yield strength of silicon 120 MPa [219] and tensile strength 90 MPa of Duran glass [220]. Above these values glass and silicon will not yield but break as both are brittle materials. To examine whether the silicon membrane buckles due to this high thermal stress, critical stress value for buckling is also calculated:

$$\sigma_{cr} = \frac{\pi^2 EI}{A(KL)^2} \quad (49)$$

where E is the modulus of elasticity, I is the moment of inertia, A is cross-sectional area, K is the effective length factor (0.2 for both ends clamped) and L is the length of the column.

Table 6-4: Parameters used to calculate the critical stress value for buckling.

E	L	K	b	h
190 x 10 ⁹ Pa	6 x 10 ⁻³ m	0.5	6 x 10 ⁻³ m	525 x 10 ⁻⁶ m

E: modulus of elasticity for silicon, L: length of membrane, K: effective length factor, b: breadth of the membrane, h: thickness of the membrane.

The critical stress value for the device used in experiment is calculated and found to be 4.7 GPa which is comparable with the thermal stress value of 4 GPa in combination with applied pressure during burst pressure test. The device's parameters used are given in Table 6-4.

On the basis of the above calculations following conclusions are drawn to clarify the cause of silicon and glass breakage at low pressure:

- It is assumed that the presence of cristobalite during annealing produces the cracks at the interface of glass and silicon while cooling due to high thermal mismatch. And when the devices are characterized for the burst pressure they tend to break at lower pressure.
- It is assumed that for high thermal stress induced the silicon membrane may buckle and while characterizing it for burst pressure it breaks at lower pressure.
- The breakage in the glass in case of smaller wall thickness (see Figure 6-6 b) is might be due to the formation of the cristobalite which dramatically reduces the thermal shock resistance and the mechanical strength of the borosilicate glass.
- The breakage phenomenon is unclear yet. It is assumed that the fracture initiated at the interface of silicon and glass (due to thermal mismatch) propagates through the glass or silicon during tests and causes the material to break.

6.4 Conclusions

Glass tube to silicon fusion bonding is a simple process for the fabrication of quality fluidic interconnects. The procedure is rather simple and needs only the standard semiconductor process equipments. The bond strength obtained is high enough for many MEMS applications such as micro flow controller, micro reactor and for fluidics in general. Reducing the surface roughness of diced glass tubes can increase the bond strength. Additionally, smooth dicing and use of smaller glass tubes can reduce leaning.

The high thermal stressed induced during cooling of the devices due to the formation of cristobalite might cause the breakage in silicon and the glass. The breakage phenomenon is unclear yet. It is assumed that the fracture initiated at interface of silicon and glass (due to thermal mismatch) propagates through the glass or silicon during tests and causes the material to break.

Both silicon and silicon oxide layer can be chosen for good quality bonding depending upon the application. However silicon nitride can be excluded for high pressure applications.

Chapter 7

7 Conclusions and Future Aspects

Abstract

In this final chapter, I summarize the work presented in this thesis and give general conclusions and recommendations for future work.

The thesis is focused on the development of the microvalve. The aim was to realize a microvalve using the combination of micro and fine machining to achieve the preferred characteristics of microvalves such as no leakage, controlled flow for high inlet pressures, control flow at different intermediate states with certain precision such as with 1-2% of full scale flow, low power consumption, robust against burst pressure, insensitivity to particular contamination, fast response time, potential for linear operation, ability to control the flow for different pressure regimes with single design. Additionally the valve should be capable of controlling the flow without power consumption at different intermediate states during valve operation.

In this thesis different design aspects for the valve have been discussed. For modeling fluid flows, the theory discussed in the 2nd chapter about using the static and the variable resistance in combination is very valuable. The principle of combination of the static resistance in series with the variable resistance is used for obtaining larger and linear controllable flow range. Additionally it also provides the benign feature to lower the Mach and Reynolds number to avoid the compressibility effects for high inlet pressures. With this method it is demonstrated that for simple geometries such as DRIE etched rectangular channels and valve seats, good analytical models can be achieved.

In the chapter 3, a new design concept based on the combination of fine and micromachining is presented. A stepper motor actuated valve has been developed and characterized using the combination of fine and micromachining. This technique enables us to control high flow rates at higher pressure. This new idea of mechanical transmission (conversion of rotational motion into the translation motion using stepper motor) not only allows us to control the valve at any intermediate state but also the valve does not need any power to keep its state. Additionally, this design prevents the interaction of the process gas with the actuation part, which enhances its robustness. A hard seating configuration, using fine and micro machining combination, contributes to the enhanced leak tight microvalve operation. Extremely low leak rates of 5×10^{-6} [ml/min] were detected with atmospheric pressure at the inlet and vacuum (1×10^{-9} bar) at the outlet. Another promising feature is that it uses simple and straightforward fine and micromachining process to realize the microvalve. The microvalve characterization for its robustness against its repeatability and its aging has been performed. The results assure that the continuous operation of the microvalve can be guaranteed by selecting the right combination of metal for screws and the bolts for the mechanical transmission

A new design based on piezoelectric actuation is described in chapter 4. The choice of the piezoelectric actuation made it possible to achieve the followings:

- Getting rid of the unnecessary long steps to improve the flow controllability. In the stepper motor actuated microvalve during valve operation the long steps are followed by the smaller steps due to the friction in between the screw threads which limits the controllability (see Figure 3-15).
- Overcoming the hysteresis, exhibited by the stepper motor actuated microvalve.
- Avoid the back lash problem which causes slow response upon switching.

This specific DSM piezoactuator proved to be robust and enhances the performance by showing almost no hysteresis and little power consumption. But the disadvantage is required power to keep the valve at a fixed position, in comparison to the design described in chapter 2 and 3.

Besides the stepper motor and piezoelectric actuated valve, a new concept based on the principle of pressure regulation is presented in chapter 5. This design also uses the concept of combination of fine and micromachining. This new design and its characterization show that it is possible to accommodate more than one pressure regimes in a single design. It has shown the promising feature of regulating the high inlet pressures to the desired low pressure value for optimum flow control. Additionally it has shown that the flow at different intermediate states in combination with the pressure regulation can be achieved.

Despite the advantages of these designs still there are certain issues for the future study. The miniaturization of the reported valve is limited by the actuator as it is the biggest component of the valve. To reduce the size of the valve the bottleneck is to reduce the actuator size. Actuators in connection with micromachined part need to be design in such a way that its integration is no more complex.

In order to make a single valve design to accommodate more pressure regimes, static resistance and the orifice and the orifice needs to be programmable.

To make the pressure regulator valve more economical, the piezoelectric actuator coupled to valve1 can be replaced by a single screw. A certain pressure depends on the application can be reached by controlling the flow with membrane deflection upon screw rotation.

Bibliography

- [1] Kwang W. Oh. and Chong H. Ahn, “A review of microvalves”, *J. Micromech. Microeng.* **16** R13-R39 (2006).
- [2] Terry S. C., Jerman J. H. and Angell J. B. “A gas chromatographic air analyzer fabricated on a silicon wafer”, *IEEE Trans. Electron Devices* **26** pp.1880–1886 (1979).
- [3] Yanagisawa K., Kuwano H. and Tapo A. “An electromagnetically driven microvalve”, *Proc. Transducers’93* pp. 102–105 (1993).
- [4] Meckes A., Behrens J., Kayser O., Benecke W., Becker T. and Muller G. “Microfluidic system for the integration and cyclic operation of gas sensors”, *Sensors Actuators A* **76** pp. 478–483 (1999).
- [5] Bae B, Kee H, Kim S, Lee Y, Sim T, Kim Y and Park K 2003 In vitro experiment of the pressure regulating valve for glaucoma implant *J. Micromech. Microeng.* **13** 613–9
- [6] Bae B., Kim N., Kee H., Kim S-H., Lee Y., Lee S. and Park K. “Feasibility test of an electromagnetically driven valve actuator for glaucoma treatment”, *J. Microelectromech. Systems.* **11** 344–354 (2002).
- [7] Krusemark O, Feustel A and Muller J 1998 Micro ball valve for fluidic micropumps and gases *Proc. Micro Total Analysis Systems ’98 Workshop* pp. 399–402
- [8] Oh. K. W., Rong R. and Ahn C. H. “In-line micro ball valve through polymer tubing”, *Proc. microTAS 2001* pp. 407–408 (2001).
- [9] Fu C., Rummeler Z. and Chomburg W. “Magnetically driven micro ball valves fabricated by multilayer adhesive film bonding”, *J. Micromech. Microeng.* **13** S96–102 (2003).
- [10] Choi J-W., Oh K. W., Thomas J. H., Heineman W. R., Halsall H. B., Nevin J. H., Helmicki A. J., Henderson H. T. and Ahn C. H. “An integrated microfluidic biochemical detection system for protein analysis with magnetic bead-based sampling capabilities”, *Lab. Chip* **2** pp. 27–30 (2002).
- [11] Oh K. W., Rong R. and Ahn C. H. “Miniaturization of pinch-type valves and pumps for practical micro total analysis system integration”, *J. Micromech. Microeng.* **15** pp. 2449–2455 (2005).
- [12] Sadler D. J., Oh K. W., Ahn C. H., Bhansali S. and Henderson H. T. “A new magnetically actuated microvalve for liquid and gas control applications” *10th Int. Conf. on Solid-State Sensors and Actuators (Transducers’99)* pp. 1812–1815 (1999).
- [13] Cho H. J., Oh K.W., Ahn C. H., Boolchand P. and Nam T-C. “Stress analysis of silicon membranes with electroplated permalloy films using Raman scattering”, *IEEE Trans. Magn.* **37** pp. 2749–2751 (2001).
- [14] Choi J-W. et. al. “Development and characterization of microfluidic devices and systems for magnetic bead-based biochemical detection”, *Biomed. Microdevices* **3** pp.191–200 (2001).
- [15] Oh K. W., Han A., Bhansali S. and Ahn C. H. “A low-temperature bonding technique using spin-on fluorocarbon polymers to assemble microsystems “ *J. Micromech. Microeng.* **12** pp. 187–91 (2002).

- [16] Sato K. and Shikida M. “An electrostatically actuated gas valve with an S-shaped film element”, *J. Micromech. Microeng.* **4** pp. 205–209 (1994).
- [17] Shikida M., Sato K., Tanaka S., Kawamura Y. and Fujisaki Y. “Electrostatically driven gas valve with high conductance”, *J. Microelectromech. Systems.* **3** pp.76–80 (1994).
- [18] Goll C., Bacher W., Bustgens B., Maas D., Ruprecht R. and Schomburg W. K. “An electrostatically actuated polymer microvalve equipped with a movable membrane electrode”, *J. Micromech. Microeng.* **7** pp. 224–226 (1997).
- [19] Robertson J. K. and Wise K. D. “A low pressure micromachined flow modulator”, *Sensors Actuators A* **71** pp. 98–106 (1998).
- [20] Schaible J., Vollmer J., Zengerle R., Sandmaier H. and Strobel T. “Electrostatic microvalves in silicon with 2-way function for industrial applications”, *11th Int. Conf. on Solid-State Sensors and Actuators (Transducers '01)* pp. 928–931 (2001).
- [21] Van der Wijngaart W., Ask H., Enoksson P. and Stemme G. “A high-stroke, high-pressure electrostatic actuator for valve applications”, *Sensors Actuators A* **100** pp. 264–271 (2002).
- [22] Yobas L., Durand D. M., Skebe G. G., Lisy F. J. and Huff M. A. “A novel integrable microvalve for refreshable braille display system”, *J. Microelectromech. Systems.* **12** pp. 252–263 (2003).
- [23] Yobas L., Huff M. A., Lisy F. J. and Durand D. M. “A novel bulk micromachined electrostatic microvalve with a curved-compliant structure applicable for a pneumatic tactile display”, *J. Microelectromech. Systems.* **10** pp. 187–196 (2001).
- [24] Teymoori M. M. and Abbaspour-Sani E. “Design and simulation of a novel electrostatic peristaltic micromachined pump for drug delivery applications”, *Sensors Actuators A* **117** pp. 22–229 (2005).
- [25] Epstein A. H. et. al. “Power MEMS and microengines”, *Proc. IEEE Conf on Solid State Sensors and Actuators (Transducer '97)* pp. 753–756 (1997).
- [26] Moon H. S., Choi D. and Spearing S. M. “Development of Si/SiC hybrid structures for elevated temperature micro-turbomachinery”, *J. Microelectromech. Systems***13** pp. 676–687 (2004).
- [27] Yang X., Holke A., Jacobson S. A., Lang J. H., Schmidt M. A. and Umans S. D. “An electrostatic, on/off microvalve designed for gas fuel delivery for the MIT Microengine”, *J. Microelectromech. Systems* **13** pp. 660–668 (2004)
- [28] Kirby B. J., Shepodd T. J. and Hasselbrink E. F. “Voltage-addressable on/off microvalves for high-pressure microchip separations”, *J. Chromatogr. A* **979** pp. 147–154 (2002).
- [29] Li H. Q., Roberts D. C., Steyn J. L., Turner K. T., Yaglioglu O., Hagood N. W., Spearing S. M. and Schmidt M. A. “Fabrication of a high frequency piezoelectric microvalve”, *Sensors Actuators A* **111** pp. 51–56 (2004).
- [30] Roberts D. C., Li H., Steyn J. L., Yaglioglu O. and Spearing S. M. “A piezoelectric microvalve for compact high-frequency, high-differential pressure hydraulic micropumping systems”, *J. Microelectromech. Systems* **12** pp. 81–92 (2003).

- [31] Rogge T., Rummeler Z. and Schomburg W. K. "Polymer micro valve with a hydraulic piezo-drive fabricated by the AMANDA process", *Sensors Actuators A* **110** pp. 206–212 (2004).
- [32] Shao P., Rummeler Z. and Schomburg W. K. "Polymer micro piezo valve with a small dead volume", *J. Micromech. Microeng.* **14** pp. 305–309 (2004).
- [33] Peirs J., Reynaert D. and van Brussel H. "Design of miniature parallel manipulators for integration in a self-propelling endoscope", *Sensors Actuators A* **85** pp.409–417 (2000).
- [34] Chakraborty I., Tang W. C., Bame D. P. and Tang T. K. "MEMS micro-valve for space applications", *Sensors Actuators A* **83** pp. 188–193 (2000).
- [35] Yang E-H., Lee C., Mueller J. and George T. "Leak-tight piezoelectric microvalve for high-pressure gas micropropulsion", *J. Microelectromech. Systems* **13** pp. 799–807 (2004).
- [36] Waibel G., Kohnle J., Cernosa R., Storz M., Schmitt M., Ernst H., Sandmaier H., Zengerle R. and Strobel T. "Highly integrated autonomous microdosage system", *Sensors Actuators A* **103** pp. 225–230 (2003).
- [37] Ernst H., Willmann M., Goettsche T., Kohnle J., Sandmaier H. and Zengerle R. "Microvalves for implantable microdosage systems", *Proc. Conf. on EMBS/BMES 2002* pp. 1840–1841 (2002).
- [38] Goettsche T., Kohnle J., Willmann M., Ernst H., Spieth S., Tischler R., Messner S., Zengerle R. and Sandmaier H. "Novel approaches to particle tolerant valves for use in drug delivery systems", *Sensors Actuators A* **118** pp. 70–77 (2005).
- [39] Jerman H. "Electrically activated, normally closed diaphragm valves", *J. Micromech. Microeng.* **4** pp. 210–216 (1994).
- [40] Barth P. W. "Silicon microvalves for gas flow control", *Proc. 8th Int. Conf. on Solid-State Sensors and Actuators (Transducers '95)* pp. 276–277 (1995).
- [41] Rich C. A. and Wise K. D. "A high-flow thermopneumatic microvalve with improved efficiency and integrated state sensing", *J. Microelectromech. Systems* **12** pp. 201–208 (2003).
- [42] Ruzzu A., Bade K., Fahrenberg J. and Maas D. "Positioning system for catheter tips based on an active microvalve system", *J. Micromech. Microeng.* **8** pp. 161–164 (1998).
- [43] Takao H., Miyamura K., Ebi H., Ashiki M., Sawada K. and Ishida K. "A MEMS microvalve with PDMS diaphragm and two-chamber configuration of thermo-pneumatic actuator for integrated blood test system on silicon", *Sensors Actuators A* **119** pp. 468–475 (2005).
- [44] Ho C-M., Yang X., Grosjean C. and Tai Y-C. "A MEMS thermopneumatic silicone rubber membrane valve", *Sensors Actuators A* **64** pp. 01–08 (1998).
- [45] Yang X., Grosjean C. and Tai Y-C. "Design, fabrication, and testing of micromachined silicone rubber membrane valves", *J. Microelectromech. Systems* **8** pp. 393–402 (1999).
- [46] Baechi D., Buser R. and Dual J. "A high density microchannel network with integrated valves and photodiodes", *Sensors Actuators A* **95** pp. 77–83 (2002).
- [47] Baechi D. and Buser R. "Suspension handling system", *Sensors Actuators B* **63** pp. 195–200 (2000).

- [48] Kim J-H., Na. K-H., Kang C. J., Jeon D. and Kim Y-S. “A disposable thermopneumatic-actuated microvalve stacked with PDMS layers and ITO-coated glass”, *Microelectron. Eng.* **73–74** pp. 864–869 (2004).
- [49] Wolf R. H. and Heuer A. H. “TiNi (shape memory) films on silicon for MEMS applications”, *J. Microelectromech. Systems* **4** pp. 206–212 (1995).
- [50] Kahn H., Huff M. A. and Heuer A. H. “The TiNi shape-memory alloy and its applications for MEMS”, *J. Micromech. Microeng.* **8** pp. 213–221 (1998).
- [51] Kohl M., Skrobanek K. D. and Miyazaki S. “Development of stress-optimised shape memory microvalves”, *Sensors Actuators A* **72** pp. 243–250.
- [52] Kohl M., Dittmann D., Quandt E., Winzek B., Miyazaki S. and Allen D. M. “Shape memory microvalves based on thin films or rolled sheets”, *Mater. Sci. Eng. A* pp. 273–755 784–288 (1999)..
- [53] Kohl M., Dittmann D., Quandt E. and Winzek B. “Thin film shape memory microvalves with adjustable operation temperature”, *Sensors Actuators A* **83** pp. 214–219 (2000).
- [54] Liu Y., Kohl M., Okutsu K. and Miyazaki S. A. “TiNiPd thin film microvalve for high temperature applications” *Mater. Sci. Eng. A* **378** pp. 205–209 (2004).
- [55] Reynaerts D., Peirs J. and Van Brussel H. “An implantable drug-delivery system based on shape memory alloy micro-actuators”, *Sensors Actuators A* **61** pp. 455–462 (1997).
- [56] Pemble C. M. and Towe B. C. “A miniature shape memory alloy pinch valve”, *Sensors Actuators A* **77** pp. 145–148 (1999).
- [57] Tamanaha C. R., Whitman L. J. and Colton R. J. “Hybrid macro–micro fluidics system for a chip-based biosensor”, *J. Micromech. Microeng.* **12** pp. N7–17 (2002).
- [58] Lisee T., Kreutzer M. and Wagner B. “A bistable pneumatic microswitch for driving fluidic components”, *Sensors Actuators A* **54** pp. 746–749 (1996).
- [59] Schomburg W. K. and Goll C. “Design optimization of bistable microdiaphragm valves”, *Sensors Actuators A* **64** pp. 259–264 (1998).
- [60] Schomburg W. K., Ahrens R., Bacher W., Martin J. and Saile V. “AMANDA—surface micromachining, molding, and diaphragm transfer”, *Sensors Actuators A* **76** pp. 343–348 (1999).
- [61] Goll C., Bacher W., Bustgens B., Maas D., Menz W. and Schomburg W. K. “Microvalves with bistable buckled polymer diaphragms”, *J. Micromech. Microeng.* **6** pp. 77–79 (1996).
- [62] Ren H. and Gerhard E. “Design and fabrication of a current-pulse-excited bistable magnetic microactuator”, *Sensors Actuators A* **58** pp. 259–264 (1997).
- [63] Bohm S., Burger G. J., Korthorst M. T. and Roseboom F. “A micromachined silicon valve driven by a miniature bi-stable electro-magnetic actuator”, *Sensors Actuators* **80** pp. 77–83 (2000).
- [64] Capanu M., Boyd J. G. and Hesketh P. J. “Design, fabrication, and testing of a bistable electromagnetically actuated microvalve”, *J. Microelectromech. Systems* **9** pp. 181–189 (2000).

- [65] Wagner B., Quenzer H. J., Hoerschelmann S., Lisec T. and Juerss M. “Bistable microvalve with pneumatically coupled membranes”, *9th Ann. IEEE Int. MEMS Workshop* pp. 384–388 (1996).
- [66] Bosh D., Heimhofer B., Muck G., Seidel H., Thumser U. and Welser W. “A silicon microvalve with combined electromagnetic/electrostatic actuation”, *Sensors Actuators A* **37/38** pp. 684–692 (1993).
- [67] Neagu C. R., Gardeniers J. G. E., Elwenspoek M. C. and Kelly J. J. “An electrochemical microactuator: principle and first results” *J. Microelectromech. Systems* **5** pp. 2–9 (1996).
- [68] Neagu C. R., Gardeniers J. G. E., Elwenspoek M. C. and Kelly J. J. “An electrochemical active valve”, *Electrochim. Acta* **42** pp. 3367–3373 (1997).
- [69] Suzuki H. and Yoneyama R. “Integrated microfluidic system with electrochemically actuated on-chip pumps and valves”, *Sensors Actuators B* **96** pp. 38–45 (2003).
- [70] Hua S. Z., Sachs F., Yang D. X. and Chopra H. D. “Microfluidic actuation using electrochemically generated bubbles”, *Anal. Chem.* **74** pp. 6392–6396 (2002).
- [71] Takahashi K., Yoshino K., Hatano S., Nagayama K. and Asano T. “Novel applications of thermally controlled microbubble driving system”, *Proc. IEEE MEMS 2001* pp. 286–289 (2001).
- [72] English A. E., Edelman E. R. and Tanaka T. “Polymer hydrogel phase transitions Experimental Methods in Polymer”, *Science: Modern Methods in Polymer Research & Technology (New York: Academic)* pp. 547–589 (2000).
- [73] Beebe D. J., Moore J. S., Bauer J. M., Yu Q., Liu R. H., Devadoss C. and Jo B. H. “Functional hydrogel structures for autonomous flow control inside microfluidic channels”, *Nature* **404** pp. 588–590 (2000).
- [74] Liu R., Yu Q. and Beebe D. J. “Fabrication and characterization of hydrogel-based microvalves”, *J. Microelectromech. Systems* **11** pp. 45–53 (2002).
- [75] Eddington D. T. and Beebe D. J. “A valved responsive hydrogel microdispensing device with integrated pressure source”, *J. Microelectromech. Systems* **13** pp. 586–593 (2004).
- [76] Baldi A., Gu Y., Loftness P. E., Siegel R. A. and Ziaie B. “A hydrogel-actuated environmentally sensitive microvalve for active flow control”, *J. Microelectromech. Systems* **12** pp. 613–621 (2003).
- [77] Richter A., Kuckling D., Howitz S., Gehring T. and Arndt K-F. “Electronically controllable microvalves based on smart hydrogels: magnitudes and potential applications”, *J. Microelectromech. Systems* **12** pp. 748–753 (2003).
- [78] Richter A., Howitz S., Kuckling D. and Arndt K-F. “Influence of volume phase transition phenomena on the behavior of hydrogel-based valves”, *Sensors Actuators B* **99** pp. 451–458 (2004).
- [79] Yu C, Mutlu S., Selvaganapathy P., Mastrangelo C. H., Svec F. and Frechet J. M. J. “Flow control valves for analytical microfluidic chips without mechanical parts based on thermally responsive monolithic polymers”, *Anal. Chem.* **75** pp. 1958–1961 (2003).
- [80] Hu Z., Zhang X. and Li. Y. “Synthesis and application of modulated polymer gels”, *Science* **269** pp. 525–527 (1995).

- [81] Low L-M., Seetharaman S., He K-Q. and Madou M. J. “Microactuators toward microvalves for responsive controlled drug delivery”, *Sensors Actuators B* **67** pp. 149–160 (2000).
- [82] Tanaka T., Nishio I., Sun S-T. and Ueno-Nishio S. “Collapse of gels in an electric field”, *Science* **218** pp. 467–669 (1982)
- [82] Suzuki A. and Tanaka T. “Phase transition in polymer gels induced by visible light”, *Nature* **346** pp. 345–347 (1990).
- [83] Kataoka K., Miyazaki H., Bunya M., Okano T. and Sakurai Y. “Totally synthetic polymer gels responding to external glucose concentration: their preparation and application to on–off regulation of insulin release”, *J. Am. Chem. Soc.* **120** pp. 694–695 (1998).
- [84] Miyata T., Asami N. and Urugami T. “A reversibly antigen-responsive hydrogel”, *Nature* **399** pp. 766–769 (1999).
- [85] Liu Y., Rauch C. B., Stevens R. L., Lenigk R., Yang J., Rhine D. B. and Grodzinski P. “DNA amplification and hybridization assays in integrated plastic monolithic devices”, *Anal. Chem.* **74** pp. 3063–3070 (2002).
- [86] Tashiro K., Ikeda S., Sekiguchi T., Shoji S., Makazu H., Funatsu T. and Tsukita S., *Proc. Micro Total Analysis Systems (MicroTAS 2001)* pp. 471–473 (2001).
- [87] Carlen E. T. and Mastrangelo C. H. “Surface micromachined paraffin-actuated microvalve”, *J. Microelectromech. Systems* **11** pp. 408–420 (2002).
- [88] Selvaganapathy P., Carlen E. T. and Mastrangelo C. H. “Electrothermally actuated inline microfluidic valve”, *Sensors Actuators A* **104** pp. 275–282 (2003)..
- [89] Klintberg L., Karlsson M., Stenmark L., Schweitz J-A. and Thornell G. “A large stroke, high force paraffin phase transition actuator”, *Sensors Actuators A* **96** pp. 189–195 (2002).
- [90] Klintberg L., Svedberg M., Nikolajeff F. and Thornell G. “Fabrication of a paraffin actuator using hot embossing of polycarbonate”, *Sensors Actuators A* **103** pp. 307–316 (2003).
- [91] Klintberg L., Karlsson M., Stenmark L. and Thornell G. “A thermally activated paraffin-based actuator for gas-flow control in a satellite electrical propulsion system”, *Sensors Actuators A* **105** pp. 237–246 (2003).
- [92] Pal R., Yang M., Johnson B. N., Burke D. T. and Burns M. A. “Phase change microvalve for integrated devices”, *Anal. Chem.* **76** pp. 3740–3748 (2004).
- [93] Liu R. H., Yang J., Lenigk R., Bonanno J. and Grodzinski P. “Single-use, thermally actuated paraffin valves for microfluidic applications”, *Sensors Actuators B* **98** pp. 328–336 (2004).
- [94] Liu R. H., Yang J., Lenigk R., Bonanno J. and Grodzinski P. “Self-contained, fully integrated biochip for sample preparation, polymerase chain reaction amplification, and DNA microarray detection”, *Anal. Chem.* **76** pp.1824–1831 (2004).
- [95] Gui L. and Liu J. “Ice valve for a mini/micro flow channel”, *J. Micromech. Microeng.* **14** pp. 242–246 (2004).
- [96] Yoshida K., Kikuchi M., Park J-H. and Yokota S. “Fabrication of micro electro-rheological valves (ER valves) by micromachining and experiments”, *Sensors Actuators A* **95** pp. 227–233 (2002).

- [97] Hatch A., Kamholz A. E., Holman G., Yager P. and Boringer K. F. "A ferrofluidic magnetic micropump" *J. Microelectromech. Systems* **10** pp. 215–221(2001).
- [98] Yamahata C., Chastellain M., Parashar V. K., Petri A., Hofmann H. and Gijs M. A. M. "Plastic micropump with ferrofluidic actuation", *J. Microelectromech. Systems* **14** pp. 96–102 (2005).
- [99] Hartshorne H., Backhouse C. J. and Lee W. E. "Ferrofluid-based microchip pump and valve", *Sensors Actuators B* **99** pp. 592–600 (2004).
- [100] Hartshorne H., Ning Y., Lee W. E. and Backhouse C. J. "Development of microfabricated valves for μ TAS", *Proc. microTAS '98 Workshop* pp. 379–381 (1998).
- [101] Oh K. W., Namkoong K. and Chinsung P. "A phase change microvalve using a meltable magnetic material: ferro-wax", *Proc. microTAS* (2005).
- [102] Oh K. W., Park C. and Namkoong K. "A world-to-chip microfluidic interconnection technology with dual functions of sample injection and sealing for a multichamber micro PCR chip", *Proc. IEEE MEMS 2005* pp. 714–717 (2005).
- [103] Oh K. W., Park C., Namkoong K., Kim J., Ock K-C., Kim S., Kim Y-A., Cho Y-K. and Ko C. "World-to-chip microfluidic interface with built-in valves for multichamber chip-based PCR assays", *Lab. Chip* **5** pp. 845–850 (2005).
- [104] Yang Z. and Maeda R. "A world-to-chip socket for microfluidic prototype development" *Electrophoresis* **23** pp.3474–3478 (2002).
- [105] Yang Z. and Maeda R. "Socket with built-in valves for the interconnection of microfluidic chips to macro constituents", *J. Chromatogr. A* **1013** pp. 29–33 (2003).
- [106] Hasegawa T., Ikuta K. and Nakashima K. "10-way micro switching valve chip for multi-directional flow control", *Proc. microTAS 2003 Workshop* pp. 215–218 (2003).
- [107] McMillan W. "A 2002 Real-time point-of-care molecular detection of infectious disease agents", *Am. Clin. Lab. January/February* pp. 29–31 (2003).
- [108] Cepheid "Sample in answer out" *GeneXpert brochure* http://www.cepheid.com/Sites/cepheid/litpdfs/GX_Brochure_V2.pdf (2005).
- [109] Takao H., Ishida M. and Sawada K. "A pneumatically actuated silicon microvalve and its application to functional fluidic integrated circuits", *Tech. Dig. Papers 11th Int. Conf. on Solid-State Sensors and Actuators (Transducers '01)* pp. 946–949 (2001).
- [110] Takao H., Ishida M. and Sawada K. "A pneumatically actuated full in-channel microvalve with MOSFET-like function in fluid channel networks", *J. Microelectromech. Systems* **11** 421–426 (2002).
- [111] Takao H. and Ishida M. "Microfluidic integrated circuits for signal processing using analogous relationship between pneumatic microvalve and MOSFET", *J. Microelectromech. Systems* **12** pp. 497–505 (2003).
- [112] Esashi M. "Silicon micromachining for integrated microsystems", *Vacuum* **47** pp. 469–474 (1996).
- [113] Luque A., Quero J. M., Hibert C., Fluckiger P. and Ganan-Calvo A. M. "Integrable silicon microfluidic valve with pneumatic actuation", *Sensors Actuators A* **118** pp. 144–151(2005).

- [114] Lagally E. T., Simpson P. C. and Mathies R. A. “Monolithic integrated microfluidic DNA amplification and capillary electrophoresis analysis system”, *Sensors Actuators B* **63** pp. 138–146 (2000).
- [115] Lagally E. T., Medintz I. and Mathies R. A. “Single molecule DNA amplification and analysis in an integrated microfluidic device”, *Anal. Chem.* **73** pp. 565–570 (2001).
- [116] Lagally E. T., Emrich C. A. and Mathies R. A. “A. Fully integrated PCR-capillary electrophoresis microsystem for DNA analysis”, *Lab. Chip* **1** pp.102–107 (2001).
- [117] Grover W. H., Skelley A. M., Liu C. N., Lagally E. T. and Mathies R. A. “Monolithic membrane valves and diaphragm pumps for practical large-scale integration into glass microfluidic devices”, *Sensors Actuators B* **89** pp. 315–323 (2003).
- [118] Lagally E. T., Scherer J. R., Blazej R. G., Toriello N. M., Diep B. A., Ramchandani M., Sensabaugh G. F., Riley L. W. and Mathies R. A. “Integrated portable genetic analysis microsystem for pathogen/infectious disease detection”, *Anal. Chem.* **76** 3162–3170 (2004).
- [119] Ohori T., Shoji S., Miura K. and Yotsumoto A. “Partly disposable three-way microvalve for a medical micro total analysis system”, *Sensors Actuators A* **64** pp. 57–62 (1998).
- [120] Go J. S. and Shoji S. “A disposable, dead volume-free and leak-free in-plane PDMS microvalve” *Sensors Actuators A* **114** pp. 438–444 (2004).
- [121] Kanai M., Abe H., Munaka T., Fujiyama Y., Uchida D., Yamayoshi A., Nakanishi H., Murakami A. and Shoji S. “Micro chamber for cellular analysis integrated with negligible dead volume sample injector”, *Sensors Actuators A* **114** pp. 129–134 (2004).
- [122] Lee S, Jeong W. and Beebe D. J. “Microfluidic valve with cored glass microneedle for microinjection”, *Lab. Chip* **3** pp. 164–167 (2003).
- [123] Baek J. Y., Park J. Y., Ju J. I., Lee T. S. and Lee S. H. “A pneumatically controllable flexible and polymeric microfluidic valve fabricated via in situ development”, *J. Micromech. Microeng.* **15** pp. 1015–1020 (2005).
- [124] Hosokawa K. and Maeda R. “A pneumatically-actuated three-way microvalve fabricated with polydimethylsiloxane using the membrane transfer technique”, *J. Micromech. Microeng.* **10** pp. 415–420 (2000).
- [125] Taylor M. T., Nguyen P., Ching J. and Petersen K. E. “Simulation of microfluidic pumping in a genomic DNA blood-processing cassette”, *J. Micromech. Microeng.* **13** pp. 201–208 (2003).
- [126] Yuen P. K., Kricka L. J. and Wilding P. “Semi-disposable microvalves for use with microfabricated devices or microchips”, *J. Micromech. Microeng.* **10** pp. 401–409 (2000).
- [127] Unger M. A., Chou H-P., Thorsen T., Scherer A. and Quake S. R. “Monolithic microfabricated valves and pumps by multilayer soft lithography”, *Science* **288** pp. 113–116 (2000).
- [128] Quake S. R. and Scherer A. “From micro to nano fabrication with soft materials”, *Science* **290** pp. 1536–1540 (2000).
- [129] Fu A. Y., Chou H-P., Spence C., Arnold F. A. and Quake S. R. “An integrated microfabricated cell sorter”, *Anal. Chem.* **74** pp. 2451–2457 (2000).
- [130] Studer V., Jameson R., Pellereau E., Pepin A. and Chen Y. “A microfluidic mammalian cell sorter based on fluorescence detection”, *Microelectron. Eng.* **73–74** pp. 852–857 (2004).

- [131] Wheeler A. R., Thronset W. R., Whelan R. J., Leach A. M., Zare R. N., Liao Y. H., Farrell K., Manger I. D. and Daridon A. "Microfluidic device for single-cell analysis", *Anal. Chem.* **75** pp. 3581–3586 (2003).
- [132] Leach A M, Wheeler A R and Zare R N 2003 Flow injection analysis in a microfluidic format *Anal. Chem.* **75** 967–72
- [133] Wang Y-C., Choi M. H. and Han J. "Two-dimensional protein separation with advanced sample and buffer isolation using microfluidic valves", *Anal. Chem.* **76** pp. 4426–4431 (2004).
- [134] Chou H-P., Unger M. A. and Quake S. R. "A microfabricated rotary pump", *Biomed. Microdevices* **2** pp. 323–330 (2001).
- [135] Liu J., Enzelberger M. and Quake S. R. "A nanoliter rotary device for polymerase chain reaction", *Electrophoresis* **23** pp. 1531–1536 (2002).
- [136] Liu J., Hansen C. and Quake S. R. "Solving the 'World-to-Chip' interface problem with a microfluidic matrix" *Anal. Chem.* **75** pp. 4718–4723 (2003).
- [137] Thorsen T., Maerkl S. J. and Quake S. R. "Microfluidic large-scale integration", *Science* **298** pp. 580–584 (2002).
- [138] Lee J. N., Park C. and Whitesides G. M. "Solvent compatibility of poly(dimethylsiloxane)-based microfluidic devices", *Anal. Chem.* **75** pp. 6544–6554 (2003).
- [139] Rolland J. P., Van Dam R. M., Schorzman D. A., Quake S. R. and DeSimone J. M. "Solvent-resistant photocurable 'Liquid Teflon' for microfluidic device fabrication", *J. Am. Chem. Soc.* **126** pp. 2322–2323 (2004).
- [140] Zengerle R. and Richter M. "Simulation of microfluid systems", *J. Micromech. Microeng.* **4** pp. 192–204 (1994).
- [141] Zengerle R., Ulrich J., Kluge S., Richter M. and Richter A. "A bidirectional silicon micropump", *Sensors Actuators A* **50** pp. 81–86 (1995).
- [142] Xu D., Wang L., Ding G., Zhou Y., Yu A. and Cai B. "Characteristics and fabrication of NiTi/Si diaphragm micropump", *Sensors Actuators A* **93** pp. 87–92 (2001).
- [143] Yang E. H., Han S. W. and Yang S. S. "Fabrication and testing of a pair of passive bivalvular microvalves composed of p + silicon diaphragms", *Sensors Actuators A* **57** pp. 75–58 (1996).
- [144] Voigt P., Schrag G. and Wachutka G. "Electrofluidic full-system modelling of a flap valve micropump based on Kirchhoffian network theory", *Sensors Actuators A* **66** pp. 9–14 (1998).
- [145] Gong Q., Zhou Z., Yang Y. and Wang X. "Design, optimization and simulation on microelectromagnetic pump", *Sensors Actuators A* **83** pp. 200–207 (2000).
- [146] Koch M., Evans A. G. R. and Brunnschweiler A. "Simulation and fabrication of micromachined cantilever valves", *Sensors Actuators A* **62** pp. 756–759 (1997).
- [147] Koch M., Evans A. G. R. and Brunnschweiler A. "Characterization of micromachined cantilever valves", *J. Micromech. Microeng.* **7** pp. 221–223 (1997).
- [148] Ulrich J. and Zengerle R. "Static and dynamic flow simulation of a KOH-etched microvalve using the finite-element method", *Sensors Actuators A* **53** pp. 379–385 (1996).

- [146] Oosterbroek R. E., Berenschot J. W., Schlautmann S., Krijnen G. J. M., Lammerink T. S. J., Elwenspoek M. C. and van den Berg A. “Designing, simulation and realization of in-plane operating micro valves, using new etching techniques”, *J. Micromech. Microeng.* **9** pp. 194–198 (1999).
- [150] Sim W. Y., Yoon H. J., Jeong O. C. and Yang S. S. “A phase-change type micropump with aluminum flap valves”, *J. Micromech. Microeng.* **13** pp. 286–294 (2003).
- [151] Yun K-S., Cho I-J., Bu J-U., Kim C. J. and Yoon E. “A surface-tension driven micropump for low-voltage and low-power operations”, *J. Microelectromech. Systems* **11** pp. 454–461 (2002).
- [152] Paul B. K. and Terhaar T. “Comparison of two passive microvalve designs for microlamination architectures”, *J. Micromech. Microeng.* **10** pp. 15–20 (2000).
- [153] Feng G-H. and Kim E. S. “Micropump based on PZT unimorph and one-way parylene valves”, *J. Micromech. Microeng.* **14** pp. 429–435 (2004).
- [154] Li B., Chen Q., Lee D-G., Woolman J. and Carman G. P. “Development of large flow rate, robust, passive micro check valves for compact piezoelectrically actuated pumps”, *Sensors Actuators A* **117** pp. 325–330 (2005).
- [155] Bien D. C. S., Mitchell S. J. N. and Gamble H. S. “Fabrication and characterization of a micromachined passive valve”, *J. Micromech. Microeng.* **13** pp. 557–562 (2003).
- [156] Hu M., Du H., Ling S-F., Fu Y., Chen Q., Chow L. and Li. B. “A silicon-on-insulator based micro check valve”, *J. Micromech. Microeng.* **14** pp. 382–387 (2004).
- [157] Chung S., Kim J. K., Wang K. C., Han D-C. and Chang J-K. “Development of MEMS-based cerebrospinal fluid shunt system”, *Biomed. Microdevices* **5** pp. 311–321 (2003).
- [158] Nguyen N-T. and Truong T-Q. “A fully polymeric micropump with piezoelectric actuator”, *Sensors Actuators B* **97** pp. 137–143 (2004).
- [159] Truong T-Q. and Nguyen N-T. “A polymeric piezoelectric micropump based on lamination technology”, *J. Micromech. Microeng.* **14** pp. 632–638 (2004).
- [160] Nguyen N-T., Truong T-Q., Wong K-K., Ho S-S. and Low C. L-N. “Micro check valves for integration into polymeric microfluidic devices”, *J. Micromech. Microeng.* **14** pp. 69–75 (2004).
- [161] Wego A. and Pagel L. “A self-filling micropump based on PCB technology”, *Sensors Actuators A* **88** pp. 220–226 (2001)
- [162] Wego A., Richter S. and Pagel L. “Fluidic microsystems based on printed circuit board technology”, *J. Micromech. Microeng.* **11** pp. 528–531 (2001).
- [163] Bohm S., Olthuis W. and Bergveld P. “A plastic micropump constructed with conventional techniques and materials”, *Sensors Actuators A* **77** pp. 223–228 (1999).
- [164] Santra S., Holloway P. and Batich C. D. “Fabrication and testing of a magnetically actuated micropump”, *Sensors Actuators B* **87** pp. 358–64 (2002)
- [165] Jensen O. S. and Gravesen P. “Flow characteristics of a micromachined diaphragm valve designed for liquid flows above 1 ml min⁻¹”, *J. Micromech. Microeng.* **3** pp. 236–238 (1993).
- [166] Gott V. L., Alejo D. E. and Cameron D. E. “Mechanical heart valves: 50 years of evolution”, *Ann. Thorac. Surg.* **76** pp. S2230–S2239 (2003).

- [167] Carrozza M. C., Croce N., Magnani B. and Dario P. “A piezoelectric-driven stereolithography-fabricated micropump”, *J. Micromech. Microeng.* **5** 177–179 (1995).
- [168] Accoto D., Carrozza M. C. and Dario P. “Modelling of micropumps using unimorph piezoelectric actuator and ball valves”, *J. Micromech. Microeng.* **10** pp. 277–281 (2000).
- [169] Yamahata C., Lacharme F., Burri Y. and Gijs M. A. M. “A ball valve micropump in glass fabricated by powder blasting”, *Sensors Actuators B* **110** pp. 1–7 (2005).
- [170] Pan T., McDonald S. J., Kai E. M. and Ziaie B. “A magnetically driven PDMS micropump with ball check-valves”, *J. Micromech. Microeng.* **15** pp. 1021–1026 (2005).
- [171] Hasselbrink E. F., Shepodd T. J. and Rehm J. E. “High-pressure microfluidic control in lab-on-a-chip devices using mobile polymer monoliths”, *Anal. Chem.* **74** pp. 4913–4918 (2002).
- [172] Reichmuth D. S., Shepodd T. J. and Kirby B. J. “On-chip high-pressure picoliter injector for pressure-driven flow through porous media”, *Anal. Chem.* **76** pp. 5063–5068 (2004).
- [173] Seidemann V., Butefisch A. and Buttgenbach S. “Fabrication and investigation of in-plane compliant SU8 structures for MEMS and their application to micro valves and micro grippers”, *Sensors Actuators A* **97–98** pp. 457–461 (2002).
- [174] Stemme E. and Stemme G. “A valveless diffuser/nozzle-based fluid pump” *Sensors Actuators A* **39** pp. 159–167 (1993).
- [175] Olsson A., Stemme G. and Stemme E. “Numerical and experimental studies of flat-walled diffuser elements for valve-less micropump”, *Sensors Actuators A* **84** pp. 165–175 (2000).
- [176] Gerlach T. and Wurmus H. “Working principle and performance of the dynamic micropump”, *Sensors Actuators A* **50** pp. 135–140 (1995).
- [177] Gerlach T. “Microdiffusers as dynamic passive valves for micropump applications”, *Sensors Actuators A* **69** pp. 181–191 (1998).
- [178] Koch M., Evans A. G. R. and Brunnschweiler A. “The dynamic micropump driven with a screen printed PZT actuator”, *J. Micromech. Microeng.* **8** pp. 119–122 (1998).
- [179] Schabmueller C. G. J., Koch M., Mokhtari M. E., Evans A. G. R., Brunnschweiler A. and Sehr H. “Self-aligning gas/ liquid micropump”, *J. Micromech. Microeng.* **12** pp. 420–424 (2002).
- [180] Olsson A., Enoksson P., Stemme G. and Stemme E. “Micromachined flat-walled valveless diffuser pumps”, *J. Microelectromech. Systems* **6** pp. 161–166 (1997).
- [181] Ullmann A. and Fono I. “The piezoelectric valve-less pump-improved dynamic model”, *J. Microelectromech. Systems* **11** pp. 655–664 (2002).
- [182] Tsai J-H. and Lin J.L. “A thermal-bubble-actuated micronozzle-diffuser pump”, *J. Microelectromech. Systems* **11** pp. 665–671 (2002).
- [183] Andersson H., van der Wijngaart W., Nilsson P., Enoksson P. and Stemme G. “A valve-less diffuser micropump for microfluidic analytical systems”, *Sensors Actuators B* **72** pp. 259–266 (2001).
- [184] Jang W I., Choi C. A., Jun C-H., Kima Y. T. and Esashi M. “Surface micromachined thermally driven micropump”, *Sensors Actuators A* **115** pp. 151–158 (2004).

- [185] Morris C. J. and Forster F. K. “Low-order modeling of resonance for fixed-valve micropumps based on first principles pump”, *J. Microelectromech. Systems* **12** pp. 325–334 (2003).
- [186] Feldt C. and Chew L. “Geometry-based macro-tool evaluation of non-moving-part valvular microchannels”, *J. Micromech. Microeng.* **12** pp. 662–669 (2002).
- [187] Ahn C. H., Choi J-W., Beaucage G., Nevin J H., Lee J-B., Puntambekar A. and Lee J. Y. “Disposable smart lab on a chip for point-of-care clinical diagnostics”, *Proc. IEEE* **92** pp. 154–173 (2004).
- [188] Yamada M. and Seki M. “Nanoliter-sized liquid dispenser array for multiple biochemical analysis in microfluidic devices”, *Anal. Chem.* **76** pp. 895–899 (2004).
- [189] Man P. F., Mastrangelo C. H., Burns M. A. and Burke D. T. “Microfabricated capillary-driven stop valve and sample injector”, *MEMS’98* pp. 45–50 (1998).
- [190] Yokoyama Y., Takeda M., Umemoto T. and Ogushi T. “Thermal micro pumps for a loop-type micro channel”, *Sensors Actuators A* **111** pp. 123–128 (2004).
- [191] Melin J., Roxhed N., Gimenez G., Griss P., van der Wijngaart W. and Stemme G. “A liquid-triggered liquid microvalve for on-chip flow control”, *Sensors Actuators B* **100** pp. 463–468 (2004).
- [192] Duffy D. C., Gillis H. L., Lin J., Sheppard N. F. and Kellogg G. J. “Microfabricated centrifugal microfluidic systems: characterization and multiple enzymatic assays”, *Anal. Chem.* **71** pp. 4669–4678 (1999).
- [193] Johnson R. D., Badr I. H. A., Barrett G., Lai S., Lu Y., Madou M. J. and Bachas L. G. “Development of a fully integrated analysis system for ions based on ion-selective optodes and centrifugal microfluidics”, *Anal. Chem.* **73** pp. 3940–3946 (2001).
- [194] Puckett L. G., Dikici E., Lai S., Madou M., Bachas L. G. and Daunert S. “Investigation into the applicability of the centrifugal microfluidics platform for the development of protein–ligand binding assays incorporating enhanced green fluorescent protein as a fluorescent reporter”, *Anal. Chem.* **76** pp. 7263–7268 (2004).
- [195] Leu T-S. and Chang P-Y. “Pressure barrier of capillary stop valves in micro sample separators”, *Sensors Actuators A* **115** pp. 508–515 (2004).
- [196] Andersson H., van der Wijngaart W., Griss P., Niklaus F. and Stemme G. “Hydrophobic valves of plasma deposited octafluorocyclobutane in DRIE channels”, *Sensors Actuators B* **75** pp. 136–141 (2001).
- [197] Andersson H., van der Wijngaart W. and Stemme G. “Micromachined filter-chamber array with passive valves for biochemical assays on beads”, *Electrophoresis* **22** pp. 249–257 (2001).
- [198] Khatait J. P., Lin W. and Lin W. J. “Design and development of orifice-type aerostatic thrust bearing”, *SIMTech Technical Reports* **6**, pp. 7-15 (2005).
- [199] Van der Pol F. C. M. “A pump based on micro-engineering techniques”, *University of Twente, FEBO, Enschede, The Netherlands*.
- [200] Bruce R., Munson, Donald F., Young and Theodore H. Okiishi, “Fundamentals of fluid mechanics”, *Fifth edition John Wily and Sons, Inc.*
- [201] Shah R. K. and London A. K., “Laminar flow forced convection in ducts”, *Academic press New York, 1993*.

- [202] Stephen P. Timischenko and Woinowsky-Krieger S., "Theory of plates and shells", McGraw Hill Book Company, Inc.
- [203] Bhushan B. and X. Li., "Micromechanical and tribological characterization of doped single-crystal silicon and polysilicon films for microelectromechanical systems devices" *J. Mater. Res.* **12**, pp.53-64 (1997).
- [204] Howatson A. M., Lund P. J. and Todd J. D., "Engineering tables and data, 2nd Edition, John Wiley and Sons, Inc.(1992)
- [205] http://www.dynamic-structures.com/piezo_actuators.html
- [206] Bings N. H., Wang C., Skinner C. D., Coyler C. L., P. Thibbault, Harrison D. J., "Microfluidic devices connected to fused silica capillaries with minimal dead volume" *Anal. Chemistry* **71** pp. 3292-3296 (1999)
- [207] Moourlas N. J., Jaeggi D., Flannery A., "Novel interconnections and channel technologies for microfluidics" *Sensors and Actuators A* **77**, pp. 57-65 (1999).
- [208] T. S. Harrison, "Packaging of the MIT microengine" S. M., Mass Inst. Technology, Cambridge MA 2000.
- [209] Harrison T. S., London A. P. and Spearing S. M., "High temperature, high pressure fluid connections for power Microsystems" *Mater. Res. Soc. Proc.*, **654** (2001).
- [210] Shoaf S. E., Feinerman A. D., "Aligned Au-Si eutectic bonding of silicon structures", *J. Vac. Sci. Tech. A* **12**, pp. 19-22 (1994).
- [211] You T. J., Lee S., Fang W., Tai Y. C., "Micromachined rubber O-ring microfluidic couplers", *Proceedings MEMS Miyazaki, Japan*, pp. 624-627 (2000).
- [212] Puntambekar A., Ahn C. H., "Self aligning microfluidic interconnects with low dead volume", *Proceedings of μ Tas, Enschede, The Netherlands*, pp. 323-326 (2000).
- [213] Marko Blom "On chip separation and sensing systems for hydrodynamic chromatography" *University of Twente, Enschede, The Netherlands*, (2000).
- [214] Yoav P., Sarkar V. T., Harrison T. S., Christopher P., Anna M. and S. Mark Spearing "Fluid packaging of microengine and microrocket devices for high pressure and high temperature operation", *J. Micromechanical Systems*, **13**, (2004).
- [215] Harendt C., Wolfgang A., Heinz-Gerd G., Bernd H. and Elisabeth P. "Wafer fusion bonding and its application to silicon on insulator fabrication", *J. Micromech. Microeng.* **1** pp. 145-151 ((1991).
- [216] Elwenspoek M. C. and Jansen H. "Silicon Micromachining" Cambridge University Press, (1998).
- [217] J. H. Jean and T. K. Gupta , Crystallization inhibitors during sintering of Pyrex borosilicate glass *J. Material Sciences Letters* **14** (1995) 1068-1070.
- [218] P. W. Macmillan, Glass-Ceramics, Academic Press, 1964.
- [219] www.matweb.com/search/SpecificMaterial.asp?bassnum=AMESi00
- [220] H. G. Pfaender, Schott Guide to Glass, Chapman & Hall, 1996.
- [221] <http://www.netmotion.com/>

List of Publications

Journals

- I. Fazal, M. C. Louwse, H. V. Jansen and M. C. Elwenspoek, “Design fabrication and characterization of a novel gas microvalve based on micro- and finemachining”, *Journal of Micromechanics and Microengineering* **16**, pp. 1207-1214 (2006).
- I. Fazal and M. C. Elwenspoek, “Design and analysis of a piezoelectric actuated microvalve for precise control of flow” *Journal of Micromechanics and Microengineering* **17**, pp. 1-14 (2007).
- I. Fazal and M. C. Elwenspoek, “Pressure regulator microvalve”, submitted to *Journal of Micromechanics and Microengineering* (2007).
- I. Fazal and M. C. Elwenspoek, “Fusion bonded fluidic interconnects” submitted to *Journal of Micromechanics and Microengineering* (2007).

Proceedings

- I. Fazal and M. C. Elwenspoek, “Piezoelectric microvalve for precise control of gas flow”, *Proceedings of ASME International Design Engineering Technical Conferences* Sep. 4-7, Las Vegas Nevada, (2007).
- I. Fazal, M. C. Louwse, H. V. Jansen and M. C. Elwenspoek, “Stepper motor actuated microvalve”, *Journal of Physics: Conference series* **34** pp. 1032-1037, *International MEMS Conference* (2006).

Posters

- I. Fazal, J. W. Berenschot, R. Deboer, H. V. Jansen and M. C. Elwenspoek, “Bond strength tests between silicon wafers and Duran tubes (Fusion bonded fluidic interconnects)”, *Proceedings of Transducers 05* pp. 936-939 (2005).
- I. Fazal and M. C. Elwenspoek, “Development and analysis of a microvalve”, *Annual Mesa+ meeting, September 2006, Enschede*.
- I. Fazal and M. C. Elwenspoek, “Design challenges for stepper motor actuated microvalve based on fine and micromachining”, *Proceedings of MME’ 07* pp.219-222 (2007).

Acknowledgements

The research presented in this thesis is the result of work carried out in the Transducers Science and Technology group with Micro and Miniaturized Flow Controller for Gas Chromatography. Support and encouragement of several people made these four years an unforgettable episode of my life. Hereby I would like to acknowledge the support I received from other persons in professional career as well as in private life.

First and foremost I would like to thank Allah Almighty for His blessings to achieve this milestone in my life.

Furthermore I would like to thank my supervisor Miko Elwenspoek for giving me the opportunity to start this PhD under his guidance. I always admire him for creating an inspiring and creative atmosphere with in the group. I have particularly enjoyed a freedom granted to me in conducting this research. Although Miko has a busy schedule but his door was always open for questions. I highly appreciate everything he did for me, not only as a supervisor but also at the human level. I thank him for his confidence and trust.

I would like to thank Erwin, Rik and Meint deBoer for their great support in development of the microfabrication methods presented in this thesis. Special thanks to Pino for designing and building my experimental setups. I also would like to thank Henk for his generous help for solving my computer problems.

I am very lucky to be part of the Transducers Science & Technology group known as MicMec all over the campus. As it is said once a MicMecer is always a MicMecer and I feel proud and honored to be a Micmecer. I thank all my current and former MicMecers for a pleasant and enjoyable time: Antonela, Arjan, Berker, Boudewijn, Dannis, Dick, Deladi Dennis, Doekle, Duy, Edin, Gijs, Hahn, Hien, Ingrid, Jeroen, John, Joost, Judith, Kees, Laura, Lisebeth, Luis, Marcel, Maryana, Marcus, Mink, Natalya, Nima, Niels, Remco, Ram, Roald, Sandeep, Saravanan, Shahina, Susan, Srinivas, Theo, Toon, Vitaly, Yipping and to everybody I have forgotten to mention.

Thanks to Mesa+ clean room, Gerard, Huib, Hans, Ite, Marion, Peter, Rene and Samantha, were extremely supportive and helpful during fabrication.

I am grateful for the nice time spent in the company of my friends: Assed, Khurren, Tania, Little angels Ayan and Elaina, Aunty and Uncle (Mr. and Mrs.

Acknowledgements

Jehangir), Obaid (Jeddah), Ehtisham (Chamma Jee), Salim, Tamalika, Rauf, Waqar and Fawad Munir.

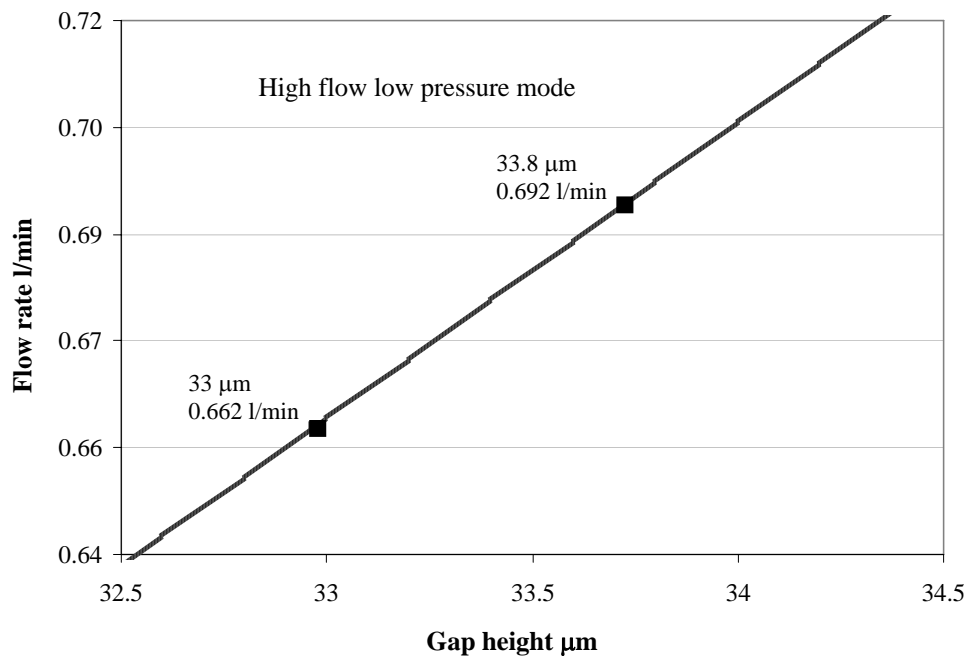
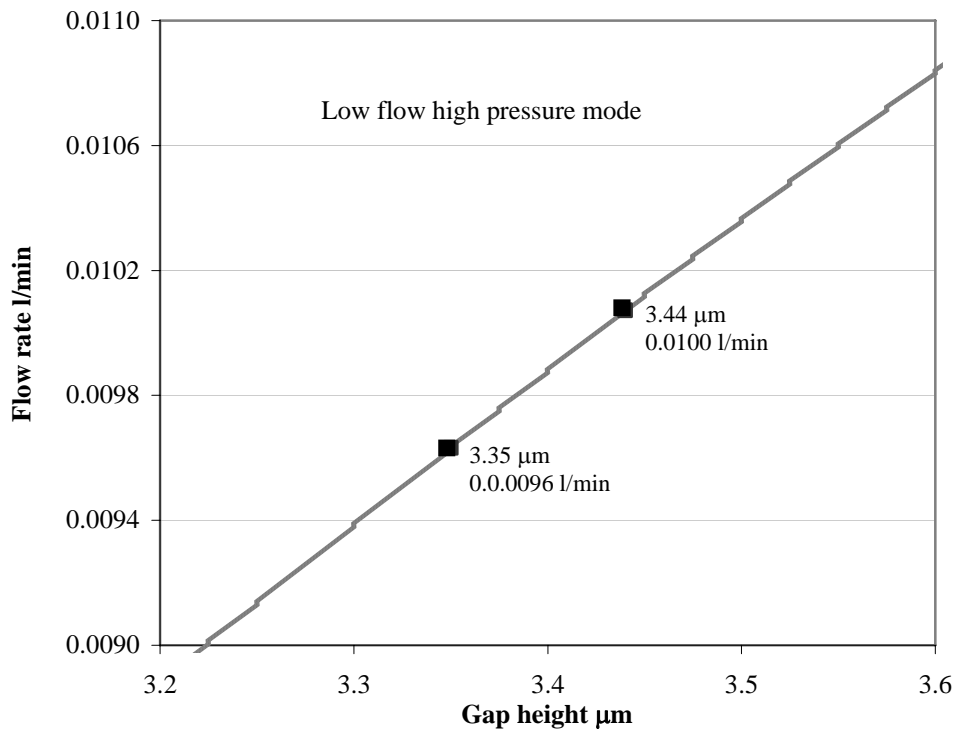
The permanent support and love of my parents is priceless. Today whatever I am is only due to their love, support and prayers for me. I consider myself blessed and extremely lucky to have such a wonderful, very loving and caring wife Samina and the center of my world my son Hussain. It would not have been possible to accomplish this milestone if I hadn't had the patience, support and prayers of my wife Samina. I am also thankful to my parents in laws for their support, love and prayers. I am always proud to have brothers like Tariq, Irfan, Kamran and Rehan who have never hesitated to be on my side whenever I needed them the most. I would also like to take this opportunity to thank my younger sisters Nadia, Sadia and my sister in laws Najma (a mother figure) & Samra along with her gorgeous three daughters Fatima, Haleema and Amna for their continuous faith and well wishes.

Imran Fazal
Enschede, October 2007

Biography

Imran Fazal was born in Lahore (Punjab), Pakistan, on 12th of November 1975. He received his B. Sc. degree in Mechanical Engineering in September 1999 from the University of Engineering and Technology, Lahore, Pakistan. In September 2003, he completed his M. Sc. degree in Mechatronics from Technical University Hamburg-Harburg after completing his dissertation work at Bosch GmbH, Reutlingen, Germany. Since November 2003 he worked as doctoral student in the Transducers Science and Technology group at University of Twente, The Netherlands, on “Development of a gas microvalve based on the combination of fine- and micromachining”.

Precession plots



Process Document for Microvalve

Single Sided Circular Membrane Microvalve

1. Introduction
 - 1.1 Design Description
 - 1.2 Explanation of Typical Process Steps
 - 1.3 Testing Apparatus
2. Mask Lay out (Overview)
3. Process Outline
4. Specific Design Parameters
5. Process Description

1 Introduction

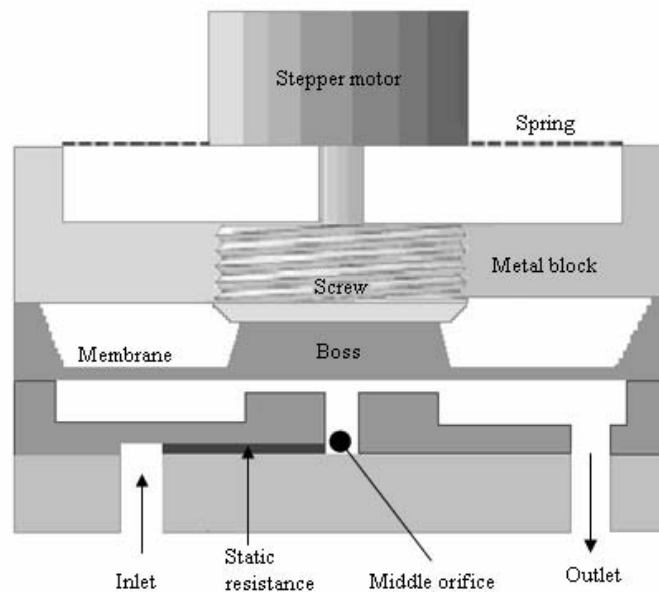
1.1 Design description

Single Sided Processing of Top Wafer

*This design is the modification of the “Double sided membrane micro valve”. In this design we used single sided circular membrane with boss etched with dry etching (BOSCH). This is done to reduce the fracture probability of membrane as the stress concentrates at the sharp edges produced by the KOH etching. It also helps to realize boss with required specifications which is not possible with KOH etching without applying edge compensation techniques.

The aim of this project is to design and develop a microvalve, which currently forms the bottleneck in the development of miniature flow controllers. Flow controllers comprise of controllable valves, flow sensors and control electronics. An important application of the flow controller is in gas chromatography, which is a system for chemical analysis of gases. The valve is an adjustable obstruction in the flow channel. Most valves are in a closed or open state when not powered. In the literature many miniaturized valves have been purposed, most of these are normally open valves. Here we want to fabricate a valve with an indifferent state: An obstruction, which keeps its geometry without requiring any power.

The current design consists of two fusion bonded Silicon <100> wafers with an additional glass wafer in order to obtain a micro stepper motor actuated active valve shown in Figure 1. Circular membranes with boss are obtained with DRIE (BOSCH), channels, variable resistance and orifice are also obtained by DRIE etching. Inlet and outlet are realized by powder blasting of Pyrex wafer.



*The process described in this document is for 3 wafers.

1.2 Explanation of typical process steps

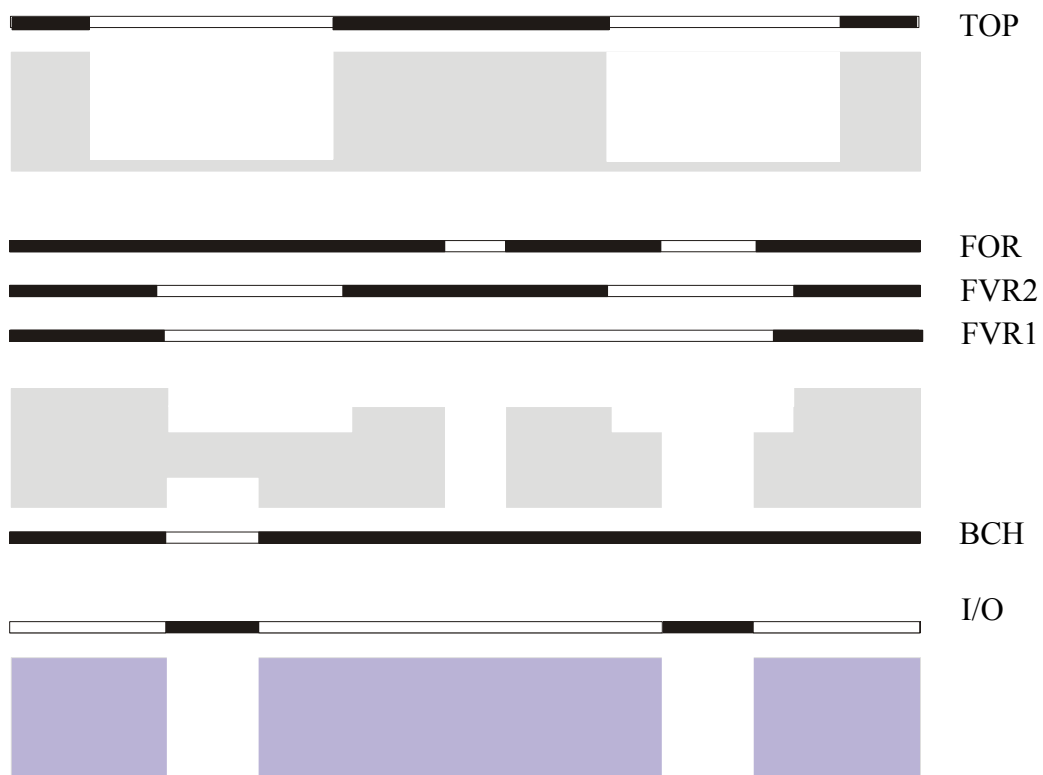
- 1- Silicon Membranes: Single sided circular membranes are realized in the top wafer with DRIE etching (BOSCH)
- 2- Channels and Holes: Channels and holes in the middle wafer are realized with DRIE.
- 3- Inlet/Out let in Glass wafers: Inlet and out let orifices are obtained with the help of powder blasting.
- 4- Fusion Bonding: Two silicon wafers are bonded to each other with fusion bonding technique.
- 5- Anodic Bonding: Two bonded silicon wafers are anodically bonded to glass wafers with inlet and out let.

2 Mask Lay Out (Overview)

2.1 Masks

Five masks are needed:

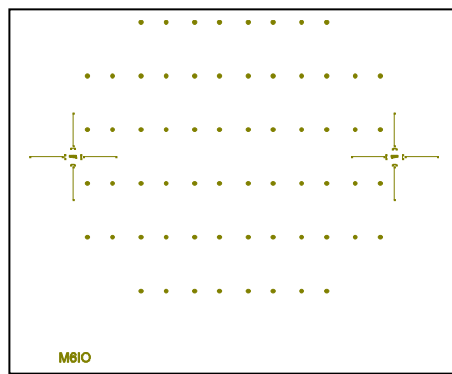
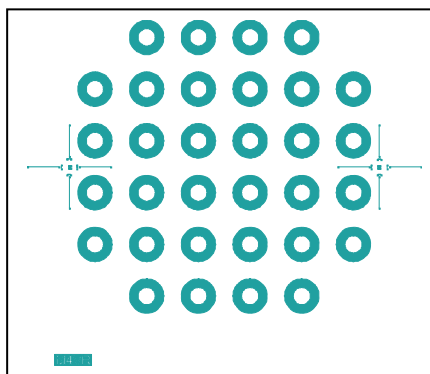
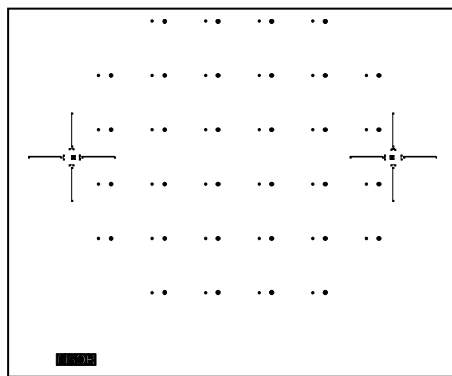
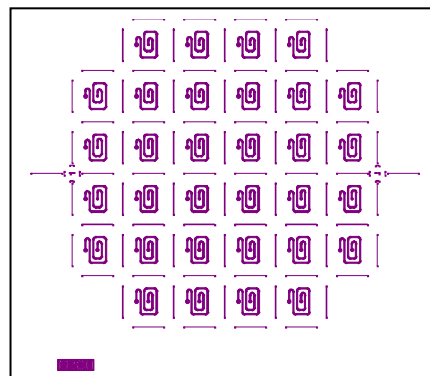
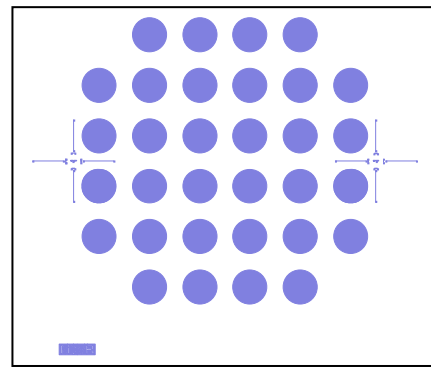
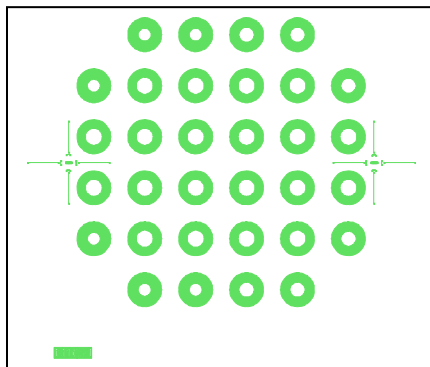
- TOP : Top side opening Dry etching (Membrane)
- BCH : Bottom side channels with RIE
- FOR : Front side orifices with RIE
- FVR1 : Front side variable resistance 1
- FVR2 : Front side variable resistance 1
- I/O : Inlet and out let in glass wafer (Powder Blasting)



2.2 Layout (over view)

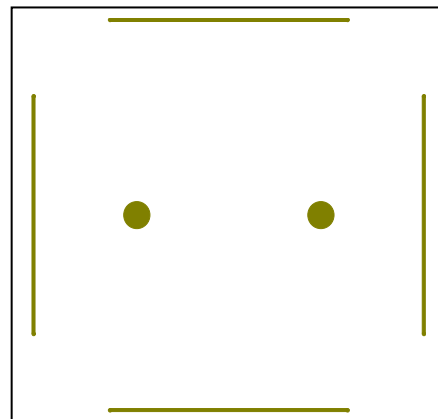
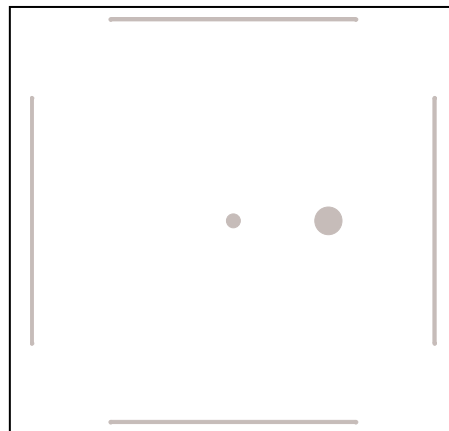
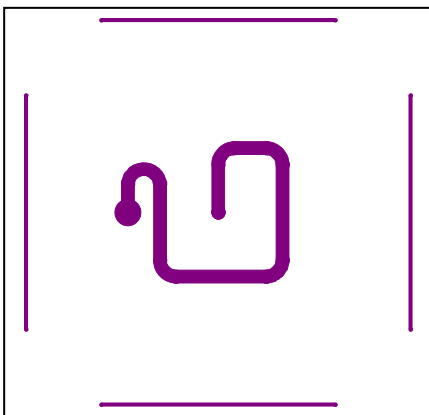
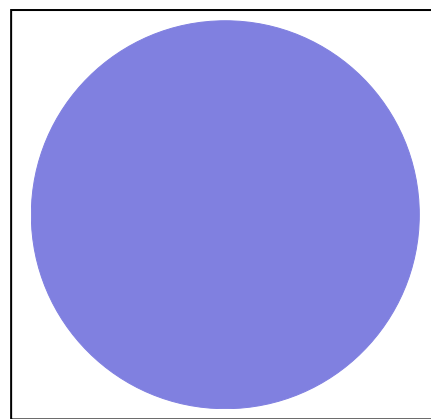
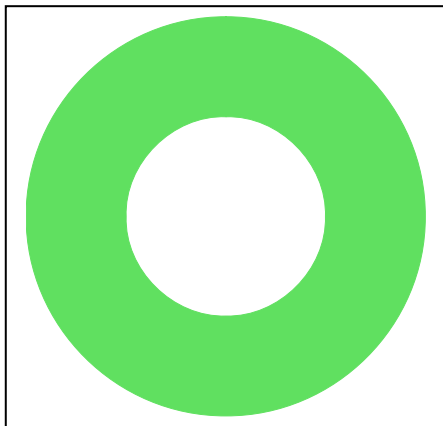
File Name: Single sided membrane microvalve

position	description	code	layer	inside white / black
Top Left	Membrane etching from topside	TOP	0	white
Top Right	Control area of membrane deflection	FVR1	1	white
Mid Left	Channels in the bottom side of 2 nd wafer	BCH	5	white
Mid Right	Orifices in the 2 nd wafer	FOR	4	white
Bottom Left	Variable resistance on front of 2 nd wafer	FVR2	3	white
Bottom Right	Inlet and outlet inside the glass wafer	I/O	6	Black




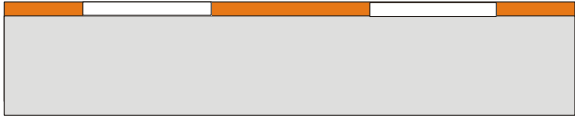

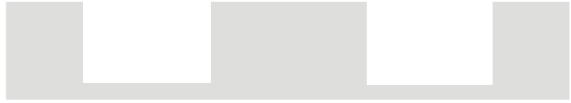
2.3 Mask Layout (Zoom IN)

position	description	code	layer	inside white / black
Top Left	Membrane etching from topside	TOP	0	white
Top Right	Control area for membrane deflection	FVR1	1	white
Mid Left	Channels in the bottom side of 2 nd wafer	BCH	5	white
Mid Right	Orifices in the 2 nd wafer	FOR	4	white
Bottom Left	Variable resistance on front of 2 nd wafer	FVR2	3	white
Bottom Right	Inlet and outlet inside the glass wafer	I/O	6	Black



3 Process outline

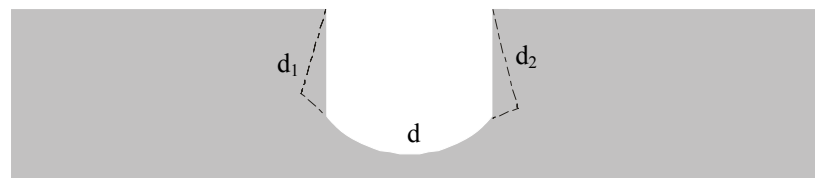
3.1 Process outline for 1st wafer (Silicon membrane)

Step	Process description	After process
1-3	Selection of Si- wafer +measurement of thickness+ Cleaning	
3-11	Patterning of Photo resist mask	
12	Dry etching of silicon	
13-16	Stripping off Photoresist and cleaning standard	



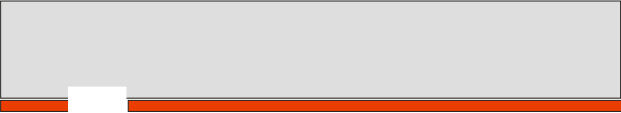
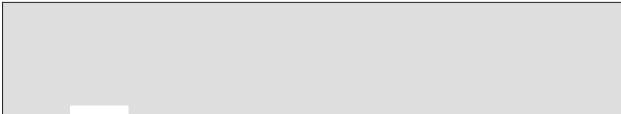
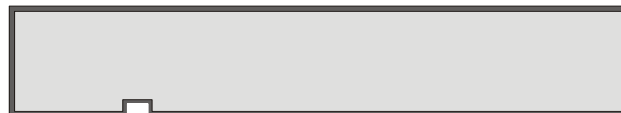
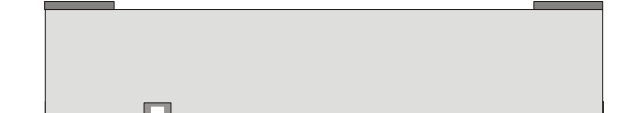

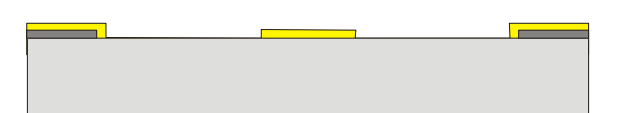
- 10 wafers with 908/35 resist, not post baked.
- Use/start with B-FAST recipe

Characterize membrane here

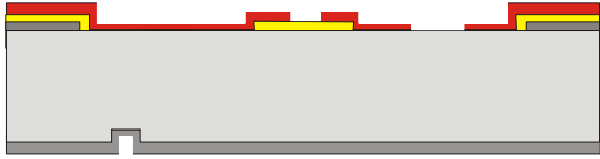
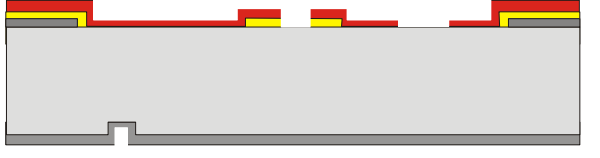
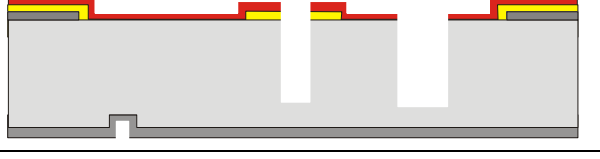
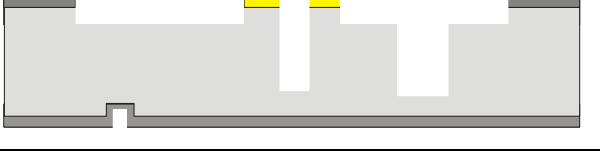
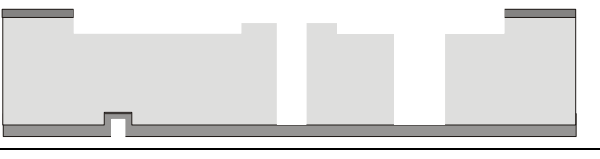
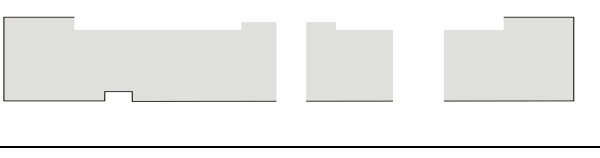
Inspect membranes and try to optimize straight trenches





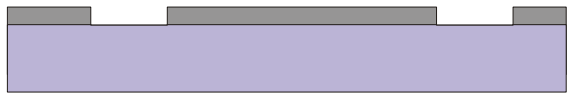


3.2 Process outline for 2nd wafer (Channels and variable resistance in Silicon wafer)

Steps	Process description	After process
1-6	Selection of silicon wafer + cleaning (Protection of Front side of the wafer with photoresist) (wafer bottom side processing) + wafer thickness measurements	
7-10	Masking of M2 (Channels)	
11	Plasma etching by Adixon	
12-13	Stripping of photo resist + Standard cleaning	
14	Wet Oxidation of SiO ₂ (Front side wafer processing)	
15-23	Wet etching of SiO ₂ (Application of Mask 3, area for membrane deflection)+ stripping off HNO ₃ +cleaning standard	
24	Chromium sputtering	
25-31	Patterning of chromium (Application of mask 4, variable resistance)	

Appendix B

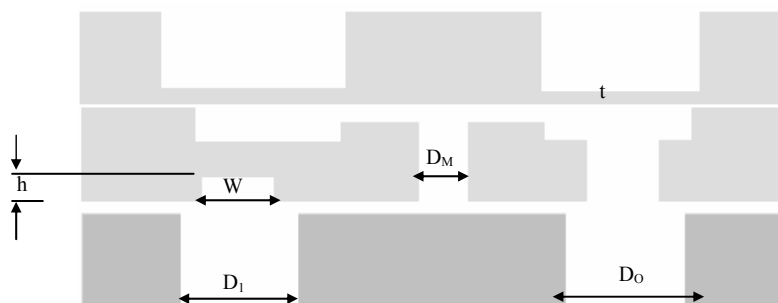
32-36	Application of Mask 5	
37-38	Etching of Chromium	
39-40	Etching of Silicon by Adixen (Orifices at the top)	
41-42	Etching of Variable resistance (Adixen silicon etching)	
43-44	(Strip off chromium) Etching of membrane deflection and through the whole wafer area by Adixen	
45-46	Wet etching of Silicon Oxide +	

3.3 Process outline for 3rd wafer

Steps	Process description	After process
1-2	Selection of Pyrex wafer + Standard cleaning	
3-4	Lamination	
5	Development	
6	Powder blasting of holes	
7-8	Removal of Lamination	

4 Specific Design Parameters

Length of Memb. : L : 7 mm
 Thickness of Memb. : t : 50 μ m
 Dia. of Inlet : D_I : 800 μ m
 Dia. of Outlet : D_O : 800 μ m
 Dia. of Main orifice : D_M : 400 μ m
 Width of Channel : W: 400 μ m
 Height of the channel : h : 60 μ m



5 Process Description

5.1 Process description for 1st wafer (Silicon membrane)

No	Process	Details	Comments
1	Substrate selection - Silicon <100> DSP (#subs002)	CR112B / Wafer Storage Cupboard Supplier: Orientation: <100> Diameter: 100mm Thickness: 525 μ m +/- 25 μ m Polished: Double side Resistivity: 5-10 Ω cm Type: p	
2	Wafer thickness measurement (#char012)	CR112B-1 / LEE-Tool01	Measure the thickness at 5 points
3	Cleaning Standard (#clean003)	CR112B / Wet-Bench 3-2 HNO ₃ (100%) Selectipur: MERCK 100453 HNO ₃ (69%) VLSI: MERCK 116445 <ul style="list-style-type: none"> • Beaker 1: fuming HNO₃ (100%), 5min • Beaker 2: fuming HNO₃ (100%), 5min • Quick Dump Rinse <0.1μS • Beaker 3: boiling (95°C) HNO₃ (69%), 10min • Quick Dump Rinse <0.1μS • Spin drying 	
4	Lithography - Priming (liquid) (#lith001)	CR112B / Suss Micro Tech Spinner (Delta 20) Hotplate 120 °C HexaMethylDiSilazane (HMDS) <ul style="list-style-type: none"> • Dehydration bake (120°C): 5min • Spinning acceleration: 4000rpm/s • Spinning speed: 4000rpm • Spinning time: 20s 	<i>To protect the Front side of the wafer</i>
5	Lithography - Coating Olin907-17 (#lith005)	CR112B / Suss Micro Tech Spinner (Delta 20) Hotplate 95 °C Olin 907-17 <ul style="list-style-type: none"> • Spinning acceleration: 4000rpm/s • Spinning speed: 4000rpm • Spinning time: 20s • Prebake (95°C): 90s 	<i>To protect the Front side of the wafer</i>
6	Lithography - Postbake standard (#lith009)	CR112B / Hotplate 120°C <ul style="list-style-type: none"> • Time: 30min 	<i>Skip post bake:</i>
7	Lithography - Priming (liquid) (#lith001)	CR112B / Suss Micro Tech Spinner (Delta 20) Hotplate 120 °C HexaMethylDiSilazane (HMDS) <ul style="list-style-type: none"> • Dehydration bake (120°C): 5min 	<i>Application of mask 1 for circular</i>

		<ul style="list-style-type: none"> • Spinning acceleration: 4000rpm/s • Spinning speed: 4000rpm • Spinning time: 20s 	<i>membrane</i>																																										
8	Lithography - Coating Olin908-35 (#lith006)	CR112B / Headway Spinner Olin 908-35 <ul style="list-style-type: none"> • Spinning speed: 4000rpm • Spinning time: 20s • Prebake (95°C): 120s1 	3000 rpm																																										
9	Lithography - Alignment & Exposure Olin 908-35 (EV)	CR117B / EVG 20 Electronic Vision Group 20 Mask Aligner <ul style="list-style-type: none"> • Exposure Time: 12 sec 	Vacuum contact Exposure time should be 22 seconds as the photo resist layer will be 5 microns																																										
10	Lithography - Development Olin Resist (#lith011)	CR112B / Wet-Bench 11 Developer: OPD4262 Hotplate 120°C (CR112B or CR117B)) <ul style="list-style-type: none"> • After Exposure Bake (120°C): 60sec Development: <ul style="list-style-type: none"> • Time: 30sec in Beaker 1 • Time: 15-30sec in Beaker 2 • Quick Dump Rinse <0.1µS • Spin drying 	Control it during development ?																																										
11	Optical microscopic inspection - Lithography (#char001)	CR112B / Nikon Microscope	Optical microscopy inspection of Lithography																																										
12	Plasma etching of Si B-FAST-1 (# ID etch064)	CR125c/Adixen SE Application: high speed silicon etching <table border="1"> <thead> <tr> <th>Parameters</th> <th>Etch</th> <th>Deposition</th> </tr> </thead> <tbody> <tr> <td>Gas</td> <td>SF6</td> <td>C4F8</td> </tr> <tr> <td>Flow sccm</td> <td>400</td> <td>10</td> </tr> <tr> <td>Time sec</td> <td>13</td> <td>2</td> </tr> <tr> <td>Priority</td> <td>2</td> <td>1</td> </tr> <tr> <td>APC %</td> <td>100</td> <td>100</td> </tr> <tr> <td>ICP Watt</td> <td>2500</td> <td>2500</td> </tr> <tr> <td>CCP Watt</td> <td>10</td> <td>10</td> </tr> <tr> <td>Pulsed (LF) ms.</td> <td>35on/65off</td> <td>35on/65off</td> </tr> <tr> <td>He mBar</td> <td>10</td> <td>10</td> </tr> <tr> <td>SH mm</td> <td>110</td> <td>110</td> </tr> <tr> <td>Electrode temp. °C.</td> <td>10</td> <td>10</td> </tr> <tr> <td>Er Olin907 [nm/min]</td> <td>???</td> <td>(high)</td> </tr> <tr> <td>Er silicon [µm/min]</td> <td>10-20</td> <td></td> </tr> </tbody> </table>	Parameters	Etch	Deposition	Gas	SF6	C4F8	Flow sccm	400	10	Time sec	13	2	Priority	2	1	APC %	100	100	ICP Watt	2500	2500	CCP Watt	10	10	Pulsed (LF) ms.	35on/65off	35on/65off	He mBar	10	10	SH mm	110	110	Electrode temp. °C.	10	10	Er Olin907 [nm/min]	???	(high)	Er silicon [µm/min]	10-20		No need to post bake in case of Bosch process. 425,450, 475 um) Membranes with the thickness of 50, 75,80 um)
Parameters	Etch	Deposition																																											
Gas	SF6	C4F8																																											
Flow sccm	400	10																																											
Time sec	13	2																																											
Priority	2	1																																											
APC %	100	100																																											
ICP Watt	2500	2500																																											
CCP Watt	10	10																																											
Pulsed (LF) ms.	35on/65off	35on/65off																																											
He mBar	10	10																																											
SH mm	110	110																																											
Electrode temp. °C.	10	10																																											
Er Olin907 [nm/min]	???	(high)																																											
Er silicon [µm/min]	10-20																																												
13	Dry Oxidation (DOX) at	CR112B / Furnace B3	30 minutes																																										

Appendix B

	800°C of Silicon (#depo026)	Standby temperature: 800°C <ul style="list-style-type: none"> • Program: DOX-800 • Temp.: 800°C • Gas: O₂ • Flow: 4l/min 	(To remove polymer during bosch process etching)
14	Etching HF (1%) Native Oxide (#etch027)	CR112B / Wet-Bench 3-3 HF (1%) VLSI: MERCK 112629.500 <ul style="list-style-type: none"> • Etch time: >1min • Quick Dump Rinse <0.1μS • Spin drying 	10 minutes
15	Stripping of Photoresist in HNO₃ (#lith014)	CR116B / Wet-Bench 2 HNO ₃ (100%) Selectipur: MERCK 100453 <ul style="list-style-type: none"> • Beaker 1: HNO₃ (100%) 20min • Quick Dump Rinse <0.1μS • Spin drying 	20 to 30 minutes
16	Cleaning Standard (#clean003)	CR112B / Wet-Bench 3-2 HNO ₃ (100%) Selectipur: MERCK 100453 HNO ₃ (69%) VLSI: MERCK 116445 <ul style="list-style-type: none"> • Beaker 1: fuming HNO₃ (100%), 5min • Beaker 2: fuming HNO₃ (100%), 5min • Quick Dump Rinse <0.1μS • Beaker 3: boiling (95°C) HNO₃ (69%), 10min • Quick Dump Rinse <0.1μS • Spin drying 	Characterize membrane

5.2 Process description for 2nd wafer (Channels and Variable resistance)

No	Process	Details	Comments
1	Substrate selection - Silicon <100> DSP (#subs002)	CR112B / Wafer Storage Cupboard Supplier: Orientation: <100> Diameter: 100mm Thickness: 525µm +/- 25µm Polished: Double side Resistivity: 5-10Ωcm Type: p	
2	Wafer thickness measurement (#char012)	CR112B-1 / LEE-Tool01	Measure the thickness at 5 points
3	Cleaning Standard (#clean003)	CR112B / Wet-Bench 3-2 HNO ₃ (100%) Selectipur: MERCK 100453 HNO ₃ (69%) VLSI: MERCK 116445 • Beaker 1: fuming HNO ₃ (100%), 5min • Beaker 2: fuming HNO ₃ (100%), 5min • Quick Dump Rinse <0.1µS • Beaker 3: boiling (95°C) HNO ₃ (69%), 10min • Quick Dump Rinse <0.1µS • Spin drying	6 Wafers + 2 extra wafers
4	Lithography - Priming (liquid) (#lith001)	CR112B / Suss Micro Tech Spinner (Delta 20) Hotplate 120 °C HexaMethylDiSilazane (HMDS) • Dehydration bake (120°C): 5min • Spinning acceleration: 4000rpm/s • Spinning speed: 4000rpm • Spinning time: 20s	To protect the Front side of the wafer
5	Lithography - Coating Olin907-17 (#lith005)	CR112B / Suss Micro Tech Spinner (Delta 20) Hotplate 95 °C Olin 907-17 • Spinning acceleration: 4000rpm/s • Spinning speed: 4000rpm • Spinning time: 20s • Prebake (95°C): 90s	Protect the Front side of the wafer by
6	Lithography - Postbake standard (#lith009)	CR112B / Hotplate 120°C • Time: 30min	Postbake 30 minutes
7	Lithography - Priming (liquid) (#lith001)	CR112B / Suss Micro Tech Spinner (Delta 20) Hotplate 120 °C HexaMethylDiSilazane (HMDS) • Dehydration bake (120°C): 5min • Spinning acceleration: 4000rpm/s • Spinning speed: 4000rpm • Spinning time: 20s	Channel fabrication with mask 2 on the bottom side of 2nd wafer
8	Lithography - Coating Olin908-35 (#lith006)	CR112B / Headway Spinner Olin 908-35 • Spinning speed: 4000rpm	3000 rpm

Appendix B

		<ul style="list-style-type: none"> • Spinning time: 20s • Prebake (95°C): 120s 																																											
9	Lithography - Alignment & Exposure Olin 908-35 (EV)	CR117B / EVG 20 Electronic Vision Group 20 Mask Aligner <ul style="list-style-type: none"> • Exposure Time: 12 sec 	<i>Vaccum contact</i> Exposure time should be 22 seconds as the photor resist layer will be 5 microns																																										
10	Lithography - Development Olin Resist (#lith011)	CR112B / Wet-Bench 11 Developer: OPD4262 Hotplate 120°C (CR112B or CR117B)) <ul style="list-style-type: none"> • After Exposure Bake (120°C): 60sec Development: <ul style="list-style-type: none"> • Time: 30sec in Beaker 1 • Time: 15-30sec in Beaker 2 • Quick Dump Rinse <0.1µS • Spin drying 	Control it during development																																										
11	Plasma etching of Si B-FAST-1 (# ID etch064)	CR125c/Adixen SE Application: high speed silicon etching <table border="0"> <thead> <tr> <th>Parameters</th> <th>Etch</th> <th>Deposition</th> </tr> </thead> <tbody> <tr> <td>Gas</td> <td>SF6</td> <td>C4F8</td> </tr> <tr> <td>Flow sccm</td> <td>400</td> <td>10</td> </tr> <tr> <td>Time sec</td> <td>13</td> <td>2</td> </tr> <tr> <td>Priority</td> <td>2</td> <td>1</td> </tr> <tr> <td>APC %</td> <td>100</td> <td>100</td> </tr> <tr> <td>ICP Watt</td> <td>2500</td> <td>2500</td> </tr> <tr> <td>CCP Watt</td> <td>10</td> <td>10</td> </tr> <tr> <td>Pulsed (LF) ms.</td> <td>35on/65off</td> <td>35on/65off</td> </tr> <tr> <td>He mBar</td> <td>10</td> <td>10</td> </tr> <tr> <td>SH mm</td> <td>110</td> <td>110</td> </tr> <tr> <td>Electrode temp. °C.</td> <td></td> <td>10</td> </tr> <tr> <td>Er Olin907 [nm/min]</td> <td>??? (high)</td> <td></td> </tr> <tr> <td>Er silicon [µm/min]</td> <td>10-20</td> <td></td> </tr> </tbody> </table>	Parameters	Etch	Deposition	Gas	SF6	C4F8	Flow sccm	400	10	Time sec	13	2	Priority	2	1	APC %	100	100	ICP Watt	2500	2500	CCP Watt	10	10	Pulsed (LF) ms.	35on/65off	35on/65off	He mBar	10	10	SH mm	110	110	Electrode temp. °C.		10	Er Olin907 [nm/min]	??? (high)		Er silicon [µm/min]	10-20		No need to post bake in case of Bosch process. (60 um)
Parameters	Etch	Deposition																																											
Gas	SF6	C4F8																																											
Flow sccm	400	10																																											
Time sec	13	2																																											
Priority	2	1																																											
APC %	100	100																																											
ICP Watt	2500	2500																																											
CCP Watt	10	10																																											
Pulsed (LF) ms.	35on/65off	35on/65off																																											
He mBar	10	10																																											
SH mm	110	110																																											
Electrode temp. °C.		10																																											
Er Olin907 [nm/min]	??? (high)																																												
Er silicon [µm/min]	10-20																																												
12	Stripping of Photoresist in HNO₃ (#lith014)	CR116B / Wet-Bench 2 HNO ₃ (100%) Selectipur: MERCK 100453 <ul style="list-style-type: none"> • Beaker 1: HNO₃ (100%) 20min • Quick Dump Rinse <0.1µS • Spin drying 	30 minutes																																										
13	Cleaning Standard (#clean003)	CR112B / Wet-Bench 3-2 HNO ₃ (100%) Selectipur: MERCK 100453 HNO ₃ (69%) VLSI: MERCK 116445 <ul style="list-style-type: none"> • Beaker 1: fuming HNO₃ (100%), 5min • Beaker 2: fuming HNO₃ (100%), 5min • Quick Dump Rinse <0.1µS • Beaker 3: boiling (95°C) HNO₃ (69%), 10min • Quick Dump Rinse <0.1µS • Spin drying 																																											

14	Wet Oxidation (WOX) at 1150°C of Silicon (#depo014)	CR112B / Furnace B2 Standby temperature: 800°C Check water level of bubbler • Program: WOX-1150 • Temp.: 1150°C • Gas: H ₂ O + N ₂ (Bubbler)	Top side wafer processing. Use of mask 3. 1.2 micron of oxide
15	Lithography - Priming (liquid) (#lith001)	CR112B / Suss Micro Tech Spinner (Delta 20) Hotplate 120 °C HexaMethylDiSilazane (HMDS) • Dehydration bake (120°C): 5min • Spinning acceleration: 4000rpm/s • Spinning speed: 4000rpm • Spinning time: 20s	
16	Lithography - Coating Olin907-17 (#lith005)	CR112B / Suss Micro Tech Spinner (Delta 20) Hotplate 95 °C Olin 907-17 • Spinning acceleration: 4000rpm/s • Spinning speed: 4000rpm • Spinning time: 20s • Prebake (95°C): 90s	
17	Lithography - Alignment & Exposure Olin 907-17 (EV) (#lith021)	CR117B / EVG 20 Electronic Vision Group 20 Mask Aligner • Exposure Time: 4sec	<i>Vaccum contact</i>
18	Lithography - Development Olin Resist (#lith011)	CR112B / Wet-Bench 11 Developer: OPD4262 Hotplate 120°C (CR112B or CR117B)) • After Exposure Bake (120°C): 60sec Development: • Time: 30sec in Beaker 1 • Time: 15-30sec in Beaker 2 • Quick Dump Rinse <0.1µS • Spin drying	
19	Lithography - Postbake standard (#lith009)	CR112B / Hotplate 120°C • Time: 30min	*Is post bake is necessary as we are doing BHF etching (yes) It is not recommended in case of BOSCH process etching
20	Lithography - Lamination of BF410 foil (#lith032)	ELTN7143/4 / GBC 3500Pro Laminator Ordyl BF410 dry resist foil • Temp: 130°C ('Carry' preset) • Speed: 2 ('Carry' preset)	Protection of Backside
21	Etching BHF (1:7) SiO₂ (#etch024)	CR112B / Wet-Bench 3-3 NH ₄ F/HF (1:7) VLSI: MERCK 101171.2500 • Quick Dump Rinse <0.1µS • Spin drying Etchrate thermal SiO ₂ = 60-80nm/min Etchrate PECVD SiO ₂ = 125/nm/min Etchrate TEOS SiO ₂ = 180/nm/min	30 minutes (14-15 minutes) ?

Appendix B

	How to remove foil		
22	Cleaning fuming HNO₃ multipurpose (#clean013)	CR116B / Wet-Bench 2 HNO ₃ (100%) Selectipur: MERCK 100453 • Beaker : HNO ₃ (100%) 5min • Quick Dump Rinse <0.1μS • Spin drying	<i>20 minutes</i>
23	Cleaning Standard (#clean003)	CR112B / Wet-Bench 3-2 HNO ₃ (100%) Selectipur: MERCK 100453 HNO ₃ (69%) VLSI: MERCK 116445 • Beaker 1: fuming HNO ₃ (100%), 5min • Beaker 2: fuming HNO ₃ (100%), 5min • Quick Dump Rinse <0.1μS • Beaker 3: boiling (95°C) HNO ₃ (69%), 10min • Quick Dump Rinse <0.1μS • Spin drying	<i>Application of mask three finished</i>
24	Sputtering of Cr (Sputterke) (#depo017)	CR106A / Sputterke Cr Target • Electrode temp.: water cooled electrode • Ar flow: 45% = 90sccm • Base pressure: 1.0e-3mbar • Sputter pressure: 5.0e-3mbar • power: 200W Depositionrate = 10nm/min	<i>50 nm</i>
25	Lithography - Priming (liquid) (#lith001)	CR112B / Suss Micro Tech Spinner (Delta 20) Hotplate 120 °C HexaMethylDiSilazane (HMDS) • Dehydration bake (120°C): 5min • Spinning acceleration: 4000rpm/s • Spinning speed: 4000rpm • Spinning time: 20s	
26	Lithography - Coating Olin907-17 (Headway) (#lith005)	CR112B / Suss Micro Tech Spinner (Delta 20) Hotplate 95 °C Olin 907-17 • Spinning acceleration: 4000rpm/s • Spinning speed: 4000rpm • Spinning time: 20s • Prebake (95°C): 90s	
27	Lithography - Alignment & Exposure Olin 907-17 (EV) (#lith021)	CR117B / EVG 20 Electronic Vision Group 20 Mask Aligner • Exposure Time: 4sec	<i>Application of mask 4 for variable resistance 200 μm</i>
28	Lithography - Development Olin Resist (#lith011)	CR112B / Wet-Bench 11 Developer: OPD4262 Hotplate 120°C (CR112B or CR117B)) • After Exposure Bake (120°C): 60sec Development: • Time: 30sec in Beaker 1 • Time: 15-30sec in Beaker 2 • Quick Dump Rinse <0.1μS • Spin drying	
29	Lithography - Postbake	CR112B / Hotplate 120°C	

	standard (#lith009)	<ul style="list-style-type: none"> • Time: 30min 	
30	Ozone anneal of Olin 907 (to improve wetting) (#lith038)	CR116B-1 / UV PRS-100 To improve wetting during etching of Chromium layers <ul style="list-style-type: none"> • time: 300sec 	
31	Etching of Cr Wet (#etch034)	CR116B / Wet-Bench 2 Chromium etch LSI Selectipur: MERCK 111547.2500 <ul style="list-style-type: none"> • Quick Dump Rinse <0.1μS • Spin drying Etchrates = 100nm/min	<i>Application of mask 4 is finished</i>
32	Cleaning fuming HNO₃ multipurpose (#clean013)	CR116B / Wet-Bench 2 HNO ₃ (100%) Selectipur: MERCK 100453 <ul style="list-style-type: none"> • Beaker : HNO₃ (100%) 5min • Quick Dump Rinse <0.1μS • Spin drying 	<i>Don't use standard cleaning as we have chromium metal.</i>
33	Lithography - Priming (liquid) (#lith001)	CR112B / Suss Micro Tech Spinner (Delta 20) Hotplate 120 °C HexaMethylDiSilazane (HMDS) <ul style="list-style-type: none"> • Dehydration bake (120°C): 5min • Spinning acceleration: 4000rpm/s • Spinning speed: 4000rpm • Spinning time: 20s 	Mask 5 for orifices in the middler wafer
34	Lithography - Coating Olin908-35 (#lith006)	CR112B / Suss Micro Tech Spinner (Delta 20) Hotplate 95 °C Olin 908-35 <ul style="list-style-type: none"> • Spinning acceleration: 4000rpm/s • Spinning speed: 4000rpm • Spinning time: 20s • Prebake (95°C): 120s 	3000 rpm
35	Lithography - Alignment & Exposure Olin 908-35 (EV)	CR117B / EVG 20 Electronic Vision Group 20 Mask Aligner <ul style="list-style-type: none"> • Exposure Time: 12 sec 	Vaccum contact Exposure time should be 22 seconds as the photo resist layer will be 5 microns
36	Lithography - Development Olin Resist (#lith011)	CR112B / Wet-Bench 11 Developer: OPD4262 Hotplate 120°C (CR112B or CR117B)) <ul style="list-style-type: none"> • After Exposure Bake (120°C): 60sec Development: <ul style="list-style-type: none"> • Time: 30sec in Beaker 1 • Time: 15-30sec in Beaker 2 • Quick Dump Rinse <0.1μS • Spin drying 	Control it after development
37	Lithography - Postbake standard (#lith009)	CR112B / Hotplate 120°C <ul style="list-style-type: none"> • Time: 30min 	
38	Ozone anneal of Olin 907 (to	CR116B-1 / UV PRS-100	

Appendix B

	improve wetting) (#lith038)	To improve wetting during etching of Chromium layers • time: 300sec	
39	Etching of Cr Wet (#etch034)	CR116B / Wet-Bench 2 Chromium etch LSI Selectipur: MERCK 111547.2500 • Quick Dump Rinse <0.1μS • Spin drying Etchrates = 100nm/min	
40	Plasma etching of Si B-FAST-1 (# ID etch064)	CR125c/Adixen SE Application: high speed silicon etching Parameters Etch Deposition Gas SF6 C4F8 Flow sccm 400 10 Time sec 13 2 Priority 2 1 APC % 100 100 ICP Watt 2500 2500 CCP Watt 10 10 Pulsed (LF) ms. 35on/65off 35on/65 off He mBar 10 10 SH mm 110 110 Electrode 10 10 temp.°C. Er Olin907 ??? (high) [nm/min] Er silicon 10-20 [μm/min]	Etch through the orifices not to the end. Time: 15min 30sec 315 um
41	Cleaning fuming HNO₃ multipurpose (#clean013)	CR116B / Wet-Bench 2 HNO ₃ (100%) Selectipur: MERCK 100453 • Beaker : HNO ₃ (100%) 5min • Quick Dump Rinse <0.1μS • Spin drying	<i>Don't use standard cleaning as we have chromium metal. Use this user made cleaning step</i>
42	Plasma etching of Si B-FAST-1 (# ID etch064)	CR125c/Adixen SE Application: high speed silicon etching Parameters Etch Deposition Gas SF6 C4F8 Flow sccm 400 10 Time sec 13 2 Priority 2 1 APC % 100 100 ICP Watt 2500 2500 CCP Watt 10 10 Pulsed (LF) ms. 35on/65off 35on/65 off He mBar 10 10 SH mm 110 110 Electrode 10 10 temp.°C. Er Olin907 ??? (high) [nm/min]	Now start etching for variable resistances Time: 16 min 45sec 150 um

		Er silicon 10-20 [μm/min]	
43	Etching of Cr Wet (#etch034)	CR116B / Wet-Bench 2 Chromium etch LSI Selectipur: MERCK 111547.2500 • Quick Dump Rinse <0.1μS • Spin drying Etchrates = 100nm/min	<i>Large etch time needed as it was in BOSCH for a long time</i> 15 minutes
44	Plasma etching of Si B-FAST-1 (# ID etch064)	CR125c/Adixen SE Application: high speed silicon etching Parameters Etch Deposition Gas SF6 C4F8 Flow sccm 400 10 Time sec 13 2 Priority 2 1 APC % 100 100 ICP Watt 2500 2500 CCP Watt 10 10 Pulsed (LF) ms. 35on/65off 35on/65off He mBar 10 10 SH mm 110 110 Electrode 10 10 temp. °C. Er Olin907 ??? (high) [nm/min] Er silicon 10-20 [μm/min]	Time: 5 min 30 sec This etching is done with dummy wafer on the bottom of the wafer with oil. It is done to do over etching. 80 um
	Cleaning Standard (#clean003)	CR112B / Wet-Bench 3-2 HNO ₃ (100%) Selectipur: MERCK 100453 HNO ₃ (69%) VLSI: MERCK 116445 • Beaker 1: fuming HNO ₃ (100%), 5min • Beaker 2: fuming HNO ₃ (100%), 5min • Quick Dump Rinse <0.1μS • Beaker 3: boiling (95°C) HNO ₃ (69%), 10min • Quick Dump Rinse <0.1μS • Spin drying	
	Dry Oxidation (DOX) at 800°C of Silicon (#depo026)	CR112B / Furnace B3 Standby temperature: 800°C • Program: DOX-800 • Temp.: 800°C • Gas: O ₂ • Flow: 4l/min	30 minutes
45	Etching HF (50%) LPCVD SiN or Thermal oxide (#etch029)	CR112B / Wet-Bench 3-3 HF (50%) VLSI: MERCK 100373.2500 • Quick Dump Rinse <0.1μS	<i>Two minutes</i>

		<ul style="list-style-type: none"> • Spin drying Etchrate SiRN = 5nm/min Etchrate SiO ₂ = 1 μm/min	
46	Cleaning Standard (#clean003)	CR112B / Wet-Bench 3-2 HNO ₃ (100%) Selectipur: MERCK 100453 HNO ₃ (69%) VLSI: MERCK 116445 <ul style="list-style-type: none"> • Beaker 1: fuming HNO₃ (100%), 5min • Beaker 2: fuming HNO₃ (100%), 5min • Quick Dump Rinse <0.1μS • Beaker 3: boiling (95°C) HNO₃ (69%), 10min • Quick Dump Rinse <0.1μS • Spin drying 	

5.3 Process description for 3rd wafer (Powder blasting for Inlet/Outlet)

1	Substrate selection - Pyrex7740 (#subs003)	CR112B / Wafer Storage Cupboard Supplier: Corning Diameter: 100mm Thickness: 500μm Bonding side up when secondary flat to left	
2	Cleaning Glass (#clean005)	CR112B / Wet-Bench 3-4 HNO ₃ (100%) Selectipur: MERCK 100453 Only use the dedicated wafer carriers and glass rod! <ul style="list-style-type: none"> • Beaker 1: HNO₃ (100%) 5min • Beaker 2: HNO₃ (100%) 5min • Quick Dump Rinse <0.1μS • Spin drying 	
3	Lithography - Lamination of BF410 foil (#lith032)	ELTN7143/4 / GBC 3500Pro Laminator Ordyl BF410 dry resist foil <ul style="list-style-type: none"> • Temp: 130°C ('Carry' preset) • Speed: 2 ('Carry' preset) 	
4	Lithography - Alignment & Exposure BF410 foil (Floor 7) (#lith034)	ELTN7143/4 / Exposure Tool <ul style="list-style-type: none"> • Time: 30sec 	
5	Lithography - Development BF410 foil (#lith036)	ELTN7143/4 / HCM Spray Developer Na ₂ CO ₃ : MERCK 1.06392.0500 Na ₂ CO ₃ :H ₂ O = 15g : 7.5liters (+ 1 cup Antifoam) <ul style="list-style-type: none"> • Temp: 32°C • Time: 3min • Rinsing • Spin drying Due to non-uniform development turn sample by 180° after half the time - small features might need longer development time	

6	Powderblasting of Glass - high resolution (#etch022)	ELTN10156 / Powderblaster For feature size >30µm <ul style="list-style-type: none"> • Particles: 9µm AlO₂ • Pressure: 4.6bar • Massflow: 3-12 g/min Etchrate appr. 29µm per g/cm ²	
7	Cleaning Ultrasonic - After Powderblasting (#clean010)	CR116B / Wet-Bench 2 Aceton: technical IPA VLSI: MERCK 107038 Removal of Al ₂ O ₃ particles <ul style="list-style-type: none"> • Beaker 1: Aceton, > 10 min (strip foil) • Beaker 2: Isopropanol > 10min • Beaker 3: DI water > 10min • Quick Dump Rinse < 0.1µS • Spin drying Glass-substrates: continue with Standard Glass Cleaning (#clean005) Silicon-substrates: continue with with Standard Wafer Cleaning (#clean003)	
8	Cleaning Glass (#clean005)	CR112B / Wet-Bench 3-4 HNO ₃ (100%) Selectipur: MERCK 100453 Only use the dedicated wafer carriers and glass rod! <ul style="list-style-type: none"> • Beaker 1: HNO₃ (100%) 5min • Beaker 2: HNO₃ (100%) 5min • Quick Dump Rinse <0.1µS • Spin drying 	

5.4 Process description for aligned fusion and anodic bonding of two silicon and one glass wafer

Direct wafer bonding of Silicon Wafers

1	Cleaning Standard (#clean003)	CR112B / Wet-Bench 3-2 HNO ₃ (100%) Selectipur: MERCK 100453 HNO ₃ (69%) VLSI: MERCK 116445 <ul style="list-style-type: none"> • Beaker 1: fuming HNO₃ (100%), 5min • Beaker 2: fuming HNO₃ (100%), 5min • Quick Dump Rinse <0.1μS • Beaker 3: boiling (95°C) HNO₃ (69%), 10min • Quick Dump Rinse <0.1μS • Spin drying 	<i>Direct wafer bonding step</i>
2	Etching HF (1%) Native Oxide (#etch027)	CR112B / Wet-Bench 3-3 HF (1%) VLSI: MERCK 112629.500 <ul style="list-style-type: none"> • Etch time: >1min • Quick Dump Rinse <0.1μS • Spin drying 	<i>Direct wafer bonding step</i>
3	Cleaning "Piranha" (H₂SO₄/H₂O₂) (#clean008)	CR112B / Wet-Bench 3-1 H ₂ SO ₄ (96%) VLSI: MERCK 100709.2500 H ₂ O ₂ (31%) VLSI: MERCK 108552.2500 Only use the dedicated wafer carriers and glass rod! H ₂ SO ₄ :H ₂ O ₂ (3:1) vol% <ul style="list-style-type: none"> • add H₂O₂ to H₂SO₄ • exothermic process! • temperature 130°C • cleaning time 10-15min • Quick Dump Rinse <0.1μS • Spin drying 	<i>Direct wafer bonding step</i>
4	EVG 20 Aligning & Prebonding of silicon wafers (#bond004)	CR112B/EVG 20 (not complete or correct, please send me the correct settings) Electronic Vision Group 20 mask aligner Program: xxxxx <ul style="list-style-type: none"> • Mask holder 4" • Mask 0.6 mm • Substrate 4" • Substrate thickness 0.6 mm • Wedge error eq.8 • separation 60 μm • N2 purge 5 • contact vacuum, bottem bond • contact force 150/10 [10] • set manual correction (0? μm) 	<i>Discuss with Erwin</i>

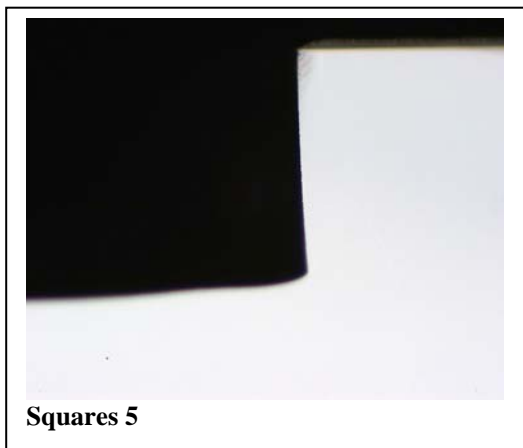
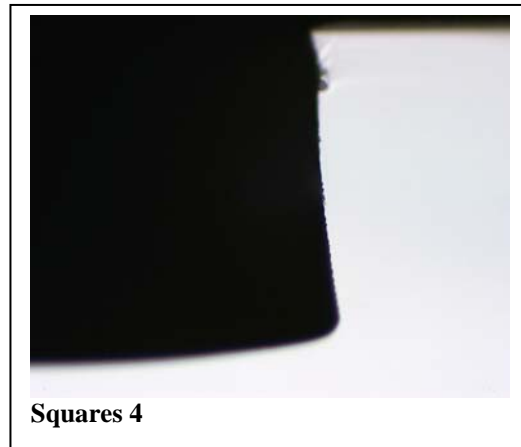
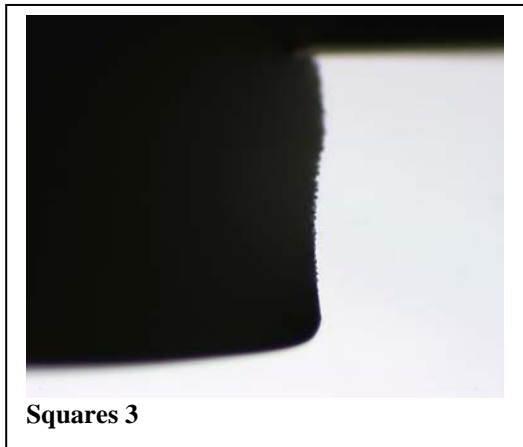
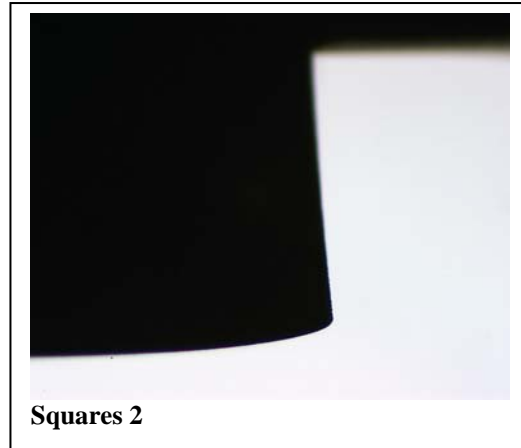
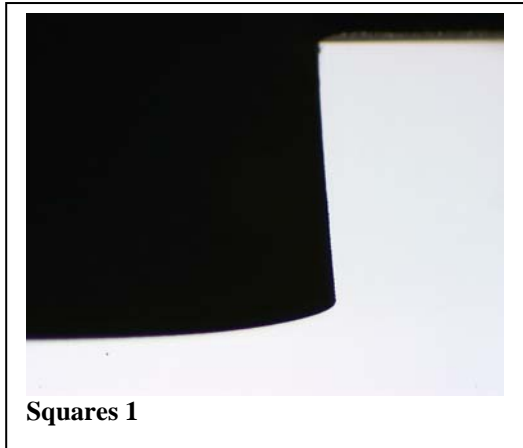
		<ul style="list-style-type: none"> • No exposure • SDB Piston • Bond time 60 sec Instructions: <ul style="list-style-type: none"> • Align alignmarks of of top wafer to crosshairs • adjust N2 pressure for center bending top wafer (1.5 bar) • NO-seal rise and NO purging prebonding • Insert both bond-chucks in the machine • If necessary use tweezers to press out air-bubbles • Check prebonding by using IR-setup 	
5	IR-inspection	-use IR setup to check the pre-bond -use tweezers for additional pressure to promote bonding of not bonded spots	
6	Annealing at 1100°C with N₂ for diffusion of B or P and annealing for Silicon-Silicon bonding (#anne006)	CR112B / Furnace B3 Standby temperature: 700°C <ul style="list-style-type: none"> • Program: ANN-1100-N2 • Temp.: 1100°C • Gas: N₂ • Flow: 1l/min • Ramp: 20°C/min 	<i>30 minutes</i>
7	IR-inspection	-use IR setup to check final bond	<i>There was a problem of conductance. How to get rid of this conductance. ?</i>
8	Etching BHF (1:7) SiO₂ (#etch024)	CR112B / Wet-Bench 3-3 NH ₄ F/HF (1:7) VLSI: MERCK 101171.2500 <ul style="list-style-type: none"> • Quick Dump Rinse <0.1µS • Spin drying Etchrate thermal SiO ₂ = 60-80nm/min Etchrate PECVD SiO ₂ = 125/nm/min Etchrate TEOS SiO ₂ = 180/nm/min	<i>For 2 minutes</i> (Dip in ethanol for 15 minutes in glass beaker before cleaning standard to get rid off conductance)

Anodic Bonding			
			<i>Ultrasonic cleaning is compulsory here.</i>
1	Cleaning Glass (#clean005)	CR112B / Wet-Bench 3-4 HNO ₃ (100%) Selectipur: MERCK 100453 Only use the dedicated wafer carriers and glass rod! <ul style="list-style-type: none"> • Beaker 1: HNO₃ (100%) 5min • Beaker 2: HNO₃ (100%) 5min 	<i>Anodic bonding of fusion bonded silicon wafers with galss</i>

		<ul style="list-style-type: none"> • Quick Dump Rinse <0.1µS • Spin drying 	
2	EVG 20 Aligning & Prebonding of silicon wafers (#bond004)	<p>CR112B/EVG 20</p> <p>(not complete or correct, please send me the correct settings)</p> <p>Electronic Vision Group 20 mask aligner Program: xxxxx</p> <ul style="list-style-type: none"> • Mask holder 4" • Mask 0.6 mm • Substrate 4" • Substrate thickness 0.6 mm • Wedge error eq.8 • separation 60 µm • N2 purge 5 • contact vacuum, bottem bond • contact force 150/10 [10] • set manual correction (0? µm) • No exposure • SDB Piston • Bond time 60 sec <p>Instructions:</p> <ul style="list-style-type: none"> • Align alignmarks of of top wafer to crosshairs • adjust N2 pressure for center bending top wafer (1.5 bar) • NO-seal rise and NO purging prebonding • Insert both bond-chucks in the machine • If necessary use tweezers to press out air-bubbles • Check prebonding by using IR-setup 	<i>Discuss with Erwin</i>
3	Anodic Bonding	<ul style="list-style-type: none"> • Vacuum AB standard 04 <p>At 400 °C</p> <ul style="list-style-type: none"> • 400 V 3 minutes • 600 V 3 minutes • 800 V 3 minutes • 1000 V 10 minutes 	<i>Equipment name, Location and remarks.</i>
Dicing			
Double-sided lamination with dicing foil, to prevent contamination			

1	1-Sided wafer lamination	-laminate the wafer at both sides with dicing foil to prevent the samples from contamination	polluted water will cause stiction and pollution of valve
2	Dicing	-Micro Automation 1006 -blade type S2035 -index1: distance between cuts // to flat -index2: distance between cuts ⊥ to flat -height: distance between blade and chuck during dicing -thickness: maneuver distance between blade and chuck -speed: 2mm/s -wafer diameter: 3" = 80 mm 4" = 110 mm -stopcount 1: number of cuts direction 1 -stopcount 2: number of cuts direction 2	cut width: 50-70μm index1: variable 10mm index2: 5mm height: 0.085mm thickness: 1.1mm wafer diameter: 80 mm stopcount 1: total 10 stopcount 2: 14 "
	Remove foil & put samples in collection box		do not pollute samples
3	Visual inspection	-visual inspection of valves with optical microscope	

Optimization of BOSCH process



	lll	ll	l	r	rr	rrr
Squares1	99	104	104	103	101	91
Squares2	100	104	106	105	101	95
Squares3	112	110	111	112	112	111
Squares4	117	117	118	118	118	116
Squares5	82	86	86	86	85	79

Depth (μm) of the trenches (l = left, r = right)

The best uniformity is obtained with processes 3 and 4. The tradeoff is seen in the sidewall of the trench. The sidewall is less straight. In this case the uniformity is more important than the sidewall of the trench. The best result is then obtained with the fourth process (Squares4). On the next page one can find the process parameters.

Process to etch through the wafer without Leakage

To keep the temperature constant during the etching process, the wafer is cooled from the backside by helium. A procedure has been developed to avoid leakage of cooling gas when etching through the process wafer. Another advantage of this method is that it is easier to cope with the RIE-lag problem. The method has been developed on the Alcatel AMS 100, using the Bosch process.

A wafer carrier was adhered to the backside of the process wafer. In the first attempt photo-resist was used to stick the wafers together. After etching, it took a very long time to remove the photo-resist between the wafers with HNO_3 . It was observed that it is very difficult to release the wafer carrier from the process wafer. Especially, when the process wafer is very fragile, it can break easily.

A better result was obtained by using Fomblin oil instead of photo-resist to stick the wafers together. Fomblin vacuum pump fluids are non-flammable, chemically inert and thermally stable. It is used in high vacuum applications, especially systems exposed to aggressive gases. The Fomblin fluid is applied to the carrier wafer by a spinning process at 4000 rpm for 20 seconds. The process wafer is manually attached to the wafer carrier. After etching, the wafer carrier is released from the process wafer. This was done at three different temperatures: room temperature, 30 seconds on a heater at 90°C and 30 seconds on a heater at 120°C . It was expected that the Fomblin oil becomes more viscous with a higher temperature and it would be easier to release the carrier wafer. It is important to shove the wafer carefully from each other. The best result was obtained by using the heater at 90°C . With the heater at 120°C it became more difficult to release the wafer carrier. At room temperature the results were good, and it is expected that it is possible to remove the wafer carrier at room temperature when the Fomblin layer is thick enough. More experiments have to be done to optimize the release of the wafer carrier by using a thicker Fomblin layer.

Because the proposed procedure is a dry method, it can also be used for comb-drive like structures. The method is also applicable for other etching apparatus in MESA

Process document for Fluidic Interconnects

Interconnection

1. Introduction
 - 1.1 Design Description
 - 1.2 Explanation of Typical Process Steps
 - 1.3 Testing Apparatus
2. Mask Lay out (Overview)
3. Process Outline
4. Specific Design Parameters
5. Process Description
 - 1.1.1

2 Introduction

2.1 Design Description

One of the goals of this project is to design and develop a microvalve, which can be used in microflow controller for analysis and synthesis of chemicals such as in Gas chromatograph. The designed micro valve should withstand the minimum pressure of 15 bars. The valve usually is an adjustable obstruction in a flow as shown in figure 1a. The current design focuses on the interconnection between glass and silicon as shown in figure 1b.

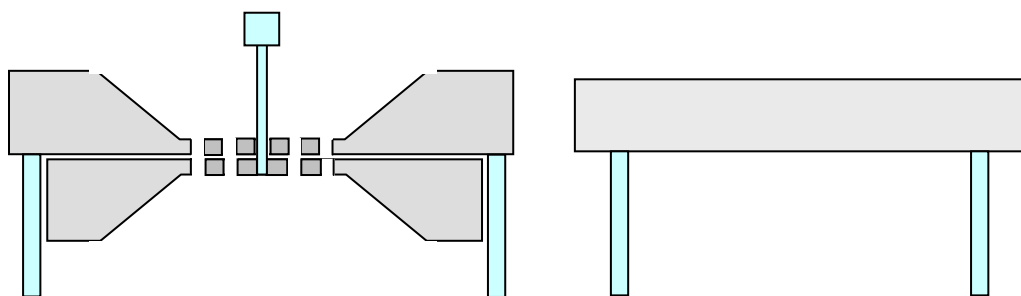


Figure 1.a) controllable microvalve b) Interconnection between glass tube and silicon chip

2.2 Explanation of Typical Process Steps

The fabrication process starts with dicing of glass (Borosilicate glass) tubes. The standard length of glass tubes is 1.5 meter, which is then diced to 15 mm and 20 mm length tubes. The cutting length and the diameter of the tubes are selected with respect to the standard swage lock available. The swage locks are used to connect the micro devices to the outside world. The longer tubes, more than 20 mm are not used, because when these are placed in the furnace at high temperature, these tend to bend due to weight. These tubes are then cleaned

with 1% HF in order to avoid contamination due to the wax used for dicing. Later on they are placed in the furnace with a standard clean silicon wafer at 400 °C. The wafer is cleaned to acquire good bonding. The temperature is then raised to 800 °C with the increasing rate of 10 °C/min. After heating them for 30 minutes the furnace is then cooled down to 400 °C. Later on standard swage locks are used with Nylon/Teflon ferrules to check the bond strength. In order to avoid skidding between glass tubes and ferrules, glass tubes are powdered blasted.

2.3 Testing Apparatus

The block diagram of the apparatus, which is used to check the bond strength of the interconnection, is shown in figure 2.

- 1- Syringe pump
- 2- Pump controller
- 3- Data storage device
- 4- Connectors
- 5- Swage lock
- 6- Interconnection fiber

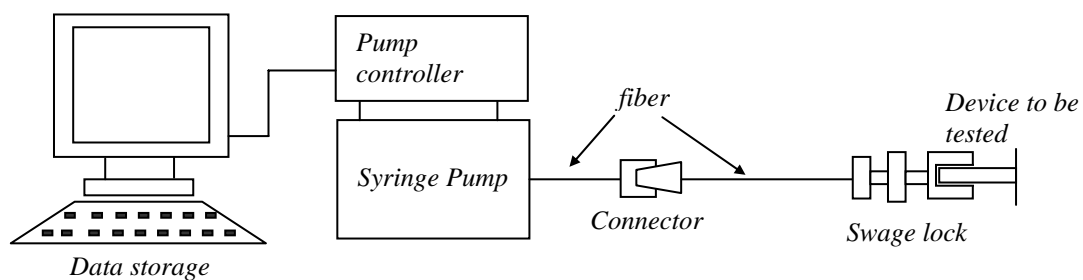


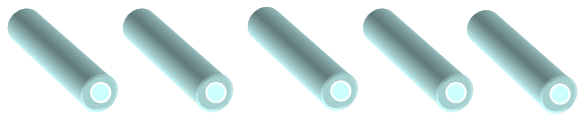

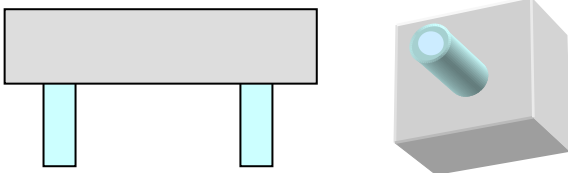
Figure 2: Block diagram of the pressure measuring apparatus

Device is connected to the pump with the help of connector, fiber and swage lock. Device is mounted in a swage lock and then connected to the pump by a fiber and connector. With this apparatus, pressure up to 600 bars can be measured. Water is used as a medium to develop pressure.

3 Mask Lay Out (Overview)

Mask lay out not needed for this device.

4 Process Outline

Step	Process description	After process
1 - 2	Selection + Dicing of Glass Tubes + Cleaning	
3-4	Selection of Si-wafer + Cleaning	
5-7	Pre Aligning + Fusion Bonding + Powder Blasting	

5 Specific Design Parameters

Schott glass tubes : Duron (Comparable with Corning /Pyrex)
 Length of the tube : 15, 20 mm
 Wall thickness : 1.0, 1.5 mm
 Outer diameter : 6.0 mm
 Swage lock diameter : 6.0 mm

6 Process Description

No	Process	Comments
1	Selection of Glass Tubes/Dicing (Borosilicate Glass)	Schott Duran / Glass Factory CT Utwente. Supplier: Schott-Rohrglass Manufacturers Outer Diameter: 6 mm +/- 0.15 Wall Thickness: 1.0 mm +/- 0.04 mm 1.5 mm +/- 0.10 mm Standard Length: 1500 mm
2	Etching HF (1%) user made (#etch028)	CR116B / Wet-Bench 2 HF (1%) VLSI: MERCK 112629.500 DI Water Cleaning of Diced Glass Tubes 12 Minutes in HF solution 20 Minutes in DI Water. To avoid contamination
3	Substrate selection - Silicon <100> OSP (#subs001)	CR112B / Wafer Storage Cupboard Supplier: Orientation: <100> Diameter: 100mm Thickness: 525µm +/- 25µm

Appendix E

		Polished: Single side Resistivity: 5-10Ωcm Type: p	
4	Cleaning Standard (#clean003)	CR112B / Wet-Bench 3-2 HNO ₃ (100%) Selectipur: MERCK 100453 HNO ₃ (69%) VLSI: MERCK 116445 • Beaker 1: fuming HNO ₃ (100%), 5min • Beaker 2: fuming HNO ₃ (100%), 5min • Quick Dump Rinse <0.1μS • Beaker 3: boiling (95°C) HNO ₃ (69%), 10min • Quick Dump Rinse <0.1μS • Spin drying	
5	Aligning & Prebonding of Silicon Wafer and Glass Tubes	• Place wafer manually on the wafer bench and align it • Place glass tubes with tweezers Wafer Bench: This is made by braking wafer in to two halves and placing them underneath a silicon wafer.	
6	Fusion bonding at 800°C with N₂ .	Furnace E2 CR 129C Standby temperature: 400°C • Temp.: 800°C • Gas: N ₂ • Flow: 4SIIm • Ramp: 10°C/min	40 Minutes to reach 800°C. 30 Minutes for Fusion Bonding. 40 Minutes to anneal it down to 400°C.
7	Powder blasting for Glass Tubes	ELTN 7140 Keramo 4 Manual Powder blasting particle size 50 uM	Rough surface is created to avoid skidding of glass tubes during testing.